UNIVERSITAT POLITÈCNICA DE CATALUNYA BARCELONATECH

Development of reduced-scale tests for HTLS substation connectors

Carlos Abomailek Rubio

DEVELOPMENT OF REDUCED-SCALE TESTS FOR HTLS SUBSTATION CONNECTORS

UNIVERSITAT POLITÈCNICA DE CATALUNYA
BARCELONATECH

PhD candidate: Carlos Abomailek Rubio

Thesis directors: Dr. Jordi-Roger Riba Ruiz

Dr. Pau Casals Torrens

Escola Tècnica Superior d'Enginyers Industrials, Aeronàutics i Audiovisuals de Terrassa

Department of Electrical Engineering

Universitat Politècnica de Catalunya

This dissertation is submitted for the degree of Doctor of Philosophy

September 2018

A mis padres por todos los sacrificios que han hecho para proporcionarme la educación que me ha llevado hasta aquí.

A Cecilia, por su infinita confianza en mí y por el amor que me ha dado día tras día.

"Things always become obvious after the fact"

- Dr. Nassim Nicholas Taleb

ABSTRACT

Power distribution networks face the upcoming challenge of managing the increase of power demand predicted worldwide. Power grid capacity is limited by the number of lines deployed and their characteristics, including conductor section, spacing, or number of phases, among others. Building new lines is costly and faces population opposition in many places. Therefore, a new conductor technology designed to upgrade the existing power lines has arisen. This technology, known as High Temperature Low-Sag (HTLS), permits the rise of capacity of existing power lines without modifying the supporting structures. Nowadays, the conductor technology is mature and under commercialization. But, there is the need to design and assess the behaviour of some auxiliary accessories needed to operate power lines equipped with HTLS conductors. Specifically, the substation connector industry is still developing HTLS substation connectors. From all the design process, the validation of the performance of these products is still a milestone. Currently, the tests performed to hardware for power lines are costly in terms of required infrastructures, testing time, power requirements, monetary cost and environmental affectation. Moreover, many of these tests can only be performed in few facilities all around the world. Furthermore, from an industrial scope, there is a growing interest to obtain the data of such tests in onsite industrial laboratories. Thus, this thesis develops a set of reduced-scale tests equivalent to the ones performed on full-scale connectors to validate the performance of the new designs. This thesis also performs a critical review of some of the methodologies that currently are being applied to assess products lifetime, and proposes the use of modern approaches. Concluding, this document aims to develop a series of test procedures that provide data about the validity of the newly required substation connectors designs in a cheaper, faster, and environmentally-friendlier way, whilst allowing to test the connectors in industrial laboratories, which have much less requirements than those of the full-scale test, since the later often require to be carried out in singular and scarce facilities.

SUMARIO

Las redes de distribución y transmisión de potencia se enfrentan al reto de manejar el incremento de demanda eléctrica previsto mundialmente. La capacidad de la red eléctrica está limitada por el número de líneas instaladas y sus características. Esto incluye, la sección del conductor, espaciado o número de fases, entre otros. La construcción de nuevas líneas es cara y en muchos casos imposible debido a la enorme oposición a la que se enfrentan en muchos lugares del mundo. Por ello, en los últimos años una nueva tecnología de conductores ha empezado a tomar importancia. Estos conductores conocidos como HTLS (alta temperatura baja flecha), permiten el aumento de la capacidad de las líneas eléctricas existentes sin por ello tener que modificar las estructuras que las soportan. Hoy en día, esta tecnología está suficientemente madura para ser comercializada. Sin embargo, existe la necesidad de diseñar y validar el comportamiento de una serie de accesorios auxiliares para líneas eléctricas. Concretamente, la industria de los conectores de subestación está desarrollando sus productos para líneas HTLS. El proceso de validación de estos conectores es aún un hito que alcanzar. Por el momento, los ensayos realizados sobre aparamenta para líneas eléctricas son costosos en términos de infraestructuras necesarias, tiempo de ensayo, potencia requerida, coste económico e impacto medioambiental. Además, muchos de estos ensayos sólo pueden llevarse a cabo en unas pocas instalaciones disponibles en todo el mundo. Por lo tanto, desde un punto de vista industrial, existe un creciente interés en obtener estos datos en laboratorios industriales. Por ello, esta tesis desarrolla un conjunto de ensayos a escala reducida equivalentes con los que hoy en día se realizan a escala real, con el fin de validar el rendimiento de los nuevos diseños de conector. Esta tesis también realiza una revisión crítica de algunas de las metodologías que hoy en día se llevan a cabo para estudiar el envejecimiento de los conectores de subestación. A su vez, propone el uso de metodologías más modernas para realizar dichos estudios. En conclusión, este documento desarrolla una serie de procedimientos de ensayo para validar los diseños de los nuevos desarrollos de conectores de subestación de una manera barata, rápida y respetuosa con el medio ambiente a la vez que permite el ensayo de dichos productos en laboratorios industriales.

ACKNOWLEDGEMENTS

I would like first to thank my directors Dr Jordi Riba and Dr Pau Casals. Jordi, you've been during these years further than an extremely dedicated director, a role-model of integrity and excellence in work and life. Pau, your experience and humanity have been of paramount importance for the realization of this thesis. I would be always in debt for your visit during the worst months of the Canadian winter.

I would like to acknowledge as well to my parents and grandparents without whom I'd never reach to the point of presenting this document. The foundations of this thesis are made of uncountable hours of your attention, the example of your lives, the resources you've dedicated to bring me a humanist education and lots of home-made food.

To you Cecilia, for supporting me during the rollercoaster of feelings that is a doctoral thesis. Thank you also for accompanying me to Canada, we spent an unforgettable time there. To my brother Nabil, for being smart-enough to follow me as a role-model just in the academic field and avoiding the rest.

To the former and present integrands of the Amber laboratory with whom I worked on the basis of comradery. Francesca, this thesis drinks from the beverages of the outstanding job that you did during your thesis. I hope to you and Jesús the best for your new paternity. José, we've suffered and we've enjoyed in equal parts, in both cases we've laughed about it. David, thanks, thanks, thanks a lot for the amount of time that you've dedicated to the success of this work. and extensively thanks SBI Connectors staff Joan, Pep, Olga and Albert. Manuel thanks for bringing your sense of humour wherever you go. Carles, it is a pleasure to know that you are going to continue my work in the laboratory. I hope you the best. Hari and Akash, prepare yourselves.

To the MCIA group in general, I have to thank you for the experience in the group. To be part of such an anomaly, as you say Luis, has been an honour for me. Ricardo and Francisco, thank you for the first tips you gave me when I just started. Vicens, thanks for the good times we've spent in the electronics lab.

To Sarajit and Dave for their kindness and for making possible my stay in Kinectrics. To Waheed who hosted us in Canada and became our father from overseas.

To my friends Víctor, Jorge, Pau, Virginia, Samuel, Franky, Adrià and all the rest with whom I shared this and the preceding years.

Finally, to whoever takes the time to read a part or all the document.

CONTENTS

LIST OF TABLES

LIST OF FIGURES

NOMENCLATURE

Acronyms	Description
AAAC	All Aluminium Alloy Conductors
AC	Alternating Current
CAD	Computer Aided Design
CEV	Corona Extinction Voltage [V]
CIV	Corona Inception Voltage [V]
DC	Direct Current
DSLR	Digital Single-Lens Reflex
FDM	Finite difference method
FEM	Finite elements method
FS	Full Scale Connector
HTLS	High Temperature Low Sag
LN	Log-normal distribution
PD	Partial Discharge
RIV	Radio Interference Voltage
RS	Reduced Scale Connector
SSADT	Step-Stress Accelerated Degradation Test
TDMA	Tri-Diagonal Matrix Algorithm
UHF	Ultra High Frequency

Symbols	Description
B	Magnetic field [T]
cp	Specific heat [J/(kg·K)]
D	Diameter [m]
d	Distance [m]
Dcorona_point	Distance between the corona inception point and the axis [cm]
E	Electril field [V/m]
Einc	Inception electric field [V/m]
g	Gravity of Earth [m/s^2]
Gr	Grashof number
h	Convective heat transfer coefficient [W/(m^2·K)]
I	Electric current [A]
k	Coefficient of thermal conductivity [W/(m·K)]
L	Characteristic Length [m]
Lc	Characteristic length [m]
m	Rugosity factor [cm$^{1/2}$]
n	Scale relationship
N	Normal distribution
Nu	Nusselt number
qe	Power losses per unit volume from Joule effect [W/m^3]
Po	Pomerantsev number
Pr	Prandtl number
q	
R	Electrical resistance [Ω]
ℜ	Reliability
Rc	Corrected curvature radius [cm]
Rcorona_point	Curvature radius of the corona inception point [cm]
S	Cross sectional area perpendicular to the electric current [m^2]
T	Temperature [K]
t	Time [s]
Tair,∞	Air temperature far from the studied point [K]
Tcond,∞	Conductor temperature far from the connector [K]
Tfilm	Film temperature [K]
To	Reference temperature, 293.15 K
v	Velocity [m/s]
V	Voltage [V]
Var	Variable
Vol	Volume [m^3]

Greek Symbols	Description
α_e	Temperature coefficient of the resistivity [1/K]
α_{ij}	Drift of resistance
β	Thermal expansion coefficient of air [1/K]
ε	Emissivity
ε_{ijk}	Measurement error in SSADT
ε_p	Electric permittivity [F/m]
θ	Parameter family
Π	Dimensionless number
ρ	Mass density [kg/m^3]
ρ_c	Density of charge [C/m^3]
ρ_e	Electrical resistivity [Ω·m]
σ	Stefan-Boltzmann constant [W/(m^2·K^4)]
σ_ε	Error variability

LIST OF APPENDICES

1 INTRODUCTION

1.1 Topic and justification

The present section describes the technology in which this thesis will be focused, the substation connectors intended for HTLS conductors. It also pinpoints the importance of such technologies and the justification, objectives and impact that aim to have this work.

It is worth noting the moment at which this work takes place. Global energy needs projections show an expansion of a 30% from now until 2040. From the total rise of energy consumption, 40% corresponds to electricity as the world is drifting towards its use as an end-use energy source [1], [2]. The rise of electricity demand implies the deployment of new power lines or the update of the existing ones. In both cases, the installed power lines are expected to carry more power when compared to the existing ones. Among the ways to carry more power using similar distribution systems as the existing ones, the HTLS (High Temperature Low Sag) technology arises as one the most promising. HTLS conductors of the same section and similar weight than the nowadays commonly installed AAAC (All Aluminium Alloy Conductors) conductors are able to transmit considerably more current. Substation connectors, introduced in this chapter, have to be able to work at higher temperatures compared to traditional applications. The high temperatures involved in the use of HTLS conductors, require a redesign of the electrical hardware attached to them. Particularly, the work presented in this thesis is focused on substation connectors, since the thesis work takes place as a collaboration between SBI Connectors SAU, a manufacturer of power connectors, and the MCIA research group of the Universitat Politècnica de Catalunya. The methodologies to validate the performance of the new developments of HTLS substation connectors are explored through this thesis.

1.1.1 Background

The development of reduced scale tests is a part of a bigger national R+D+I project. This project, called Superconnector, belongs to the research program "Retos de Colaboración" funded by the Spanish Ministry of Economy, Industry and Competitiveness, and intends to develop a new series of substation connectors specifically designed for HTLS conductors and the necessary tests to guarantee their performance. The Superconnector project is developed for SBI Connectors, a national company devoted to the manufacture of these products.

Since HTLS connectors must draw an increased electrical current, the cost of the associated standard tests rises as well. Moreover, the required tests for the HTLS connectors are less feasible in common facilities such as factory laboratories or small laboratories. Thus, the idea of performing reduced-scale tests appears highly attractive. Nevertheless, the conclusions of this thesis aim to be relevant for similar studies, related or not related with the HTLS technology.

1.1.2 HTLS conductors

As the electrical power demand grows, several problems related with the sustainability of the power network are ensued. Generally, modern societies tend to avoid building new power lines due to environmental, economic and social concerns.

There have been proposed different solutions during the last years; anyway, the most feasible solution looking from a technological, economic and social point of view is based on increasing the capacity of existing lines by replacing conventional conductors with new ones with lower electrical resistance and/or capable to operate at higher temperature rates.

Within the studied and implemented methods of increasing the capacity of power networks, the two most accepted are:

- Increase the ampacity of an existing line via the replacement of a conductor with one of larger diameter than the original one, thus decreasing in that way the overall resistance of the conductor. This solution entails an increase of the weight, ice and wind loads for which the structure of the line has to be designed. Thus, it requires the reinforcement of suspension structures.
- Increase the ampacity of an existing line by replacing the existing conductor by other of similar diameter as the original conductor, but able to operate at higher temperature. This solution avoids the reinforcement of suspension structures and, therefore, it is a simpler and cheaper solution than the first exposed. These conductors are the High Temperature Low-Sag (HTLS). They can operate at temperatures up to 200-250ºC, therefore the capacity of lines can be almost doubled without compromising their structural performance.

1.1.3 Substation connectors

According to the ANSI/NEMA CC1-2009 [3] standard, an electric connector is “a device that joins two or more conductors for the purpose of providing a continuous electrical path”.

They are commonly divided into different categories. These categories depend on the type of junction between the connector and the conductor; compression, welded and mechanical being the most common.

Substation connectors, the connectors studied within this thesis, are typically aluminium alloy devices of mechanical type. The coupling between the conductor and the connector is done by fixing the coupling parts of the connector with the conductor using nuts and bolts. The range of geometries and sizes for these connectors is really large, some examples of them are found in Figure 1.1.

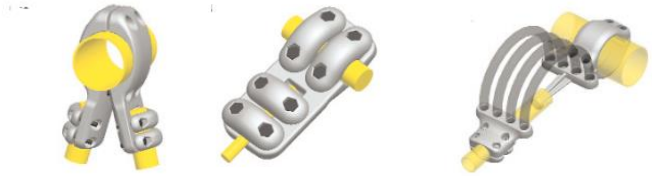

Figure 1.1: Examples of substation connectors of SBI Connectors

The fields of application of substation connectors are multiple, for instance T-connectors which appear repeatedly in this thesis, connect overhead power conductors to the substations as seen in Figure 1.2a. Others, as the connector seen in Figure 1.2b, are used to connect bus-bars with bushings and power terminations. Summarizing, substation connectors are the structural junction between the parts of a substation and between the substation and the grid. They, as well, have the function to ensure the continuity of the current path, thus being among the most critical parts in such structures. Therefore, a proper design and validation of these products prevents dramatic substation failures that can derive in economic losses, environmental accidents or personal harms.

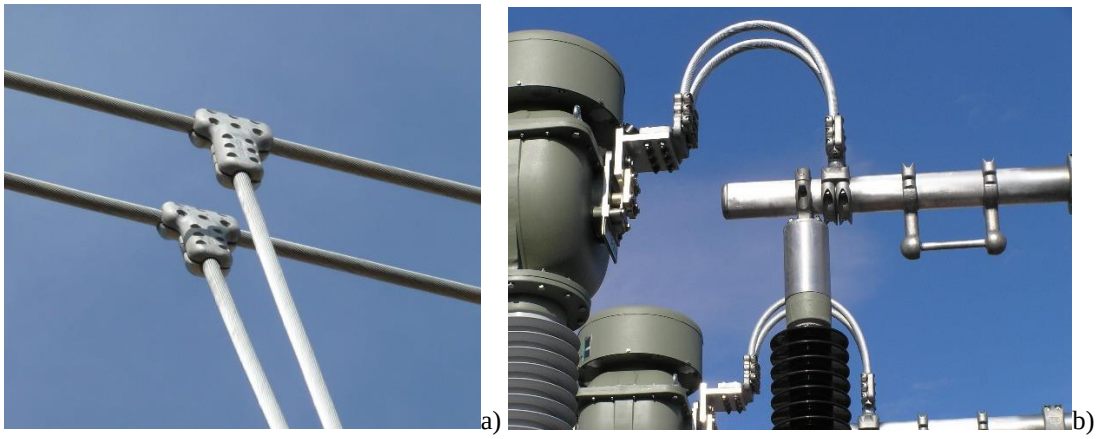

a) b)

Figure 1.2: Substation connectors a) T-connector b) Expansion connection between bus-bar and termination [4]

1.1.4 HTLS substation connectors

In parallel to the work of this thesis and within the Superconnector project, the HTLS substation connectors have been developed. These connectors are designed to work up to the temperature levels at which HTLS conductors can operate. At the same time, HTLS substation connectors must be able to maintain their resistance to mechanical stresses and to be corona-free [5], [6]. Therefore, the design of HTLS substation connectors is divided in three stages in order to attain the three aforementioned specifications. This section presents the specifications of HTLS connectors, describes the design process of substation connectors, and introduce the problems involved with the validation of the connectors.

1.1.4.1 Thermal specifications of HTLS connectors

The thermal behaviour of substation connectors notably influences their useful life. Substation connectors aimed to work with all-aluminium alloy conductors (AAAC), the conductors installed nowadays, are designed to pass several tests proposed by different standards. Nowadays, there is a lack of standards for the validation of hardware intended to work in HTLS lines. Therefore, in order to assess the specifications of HTLS connectors, the standards available nowadays for the testing of substation connectors will be used as a basis to develop new testing methodologies.

Substation connectors must pass the “Temperature rise test”. This test, described by the ANSI/NEMA CC1-2009 [3] standard, specifies that for current values 100%, 125% and 150% of the conductor nominal current, the temperature of the connector never has to surpass the one of the conductor. The nominal current of conductors is a value provided by the manufacturer of the conductor, and depends mostly on the cross-section of the conductor, the material as well as the ambient conditions. The nominal current can be obtained as well using the method of ampacity calculation proposed in IEEE 738-2012 [7]. The temperature at which HTLS conductors work, is superior to the one of AAAC conductors. Specifically, the conductors used in this thesis, the GTACSR-434 and its reduced scale homologue GTACSR-131 (described in Annex 1) have a working temperature of 150ºC. When these are tested at 150% of the nominal current, the temperature reaches a value close to 300ºC. This temperature compromises severally the mechanic behaviour of aluminium. So, there is no interest to reach this current level for the HTLS substation connectors, as if it is reached in a real application, the application would be at all effects compromised. Therefore, in this thesis, the three steps of current considered for the test are 100%, 110% and 120% of the nominal current. Figure 1.3 shows the result of a 3D-FEM simulation of the original three-steps of current applied to the S285TLS T-substation connector installed with a GTACSR-464 conductor. In the figure, it can be seen how the conductor temperature reaches the 300ºC at the third current step.

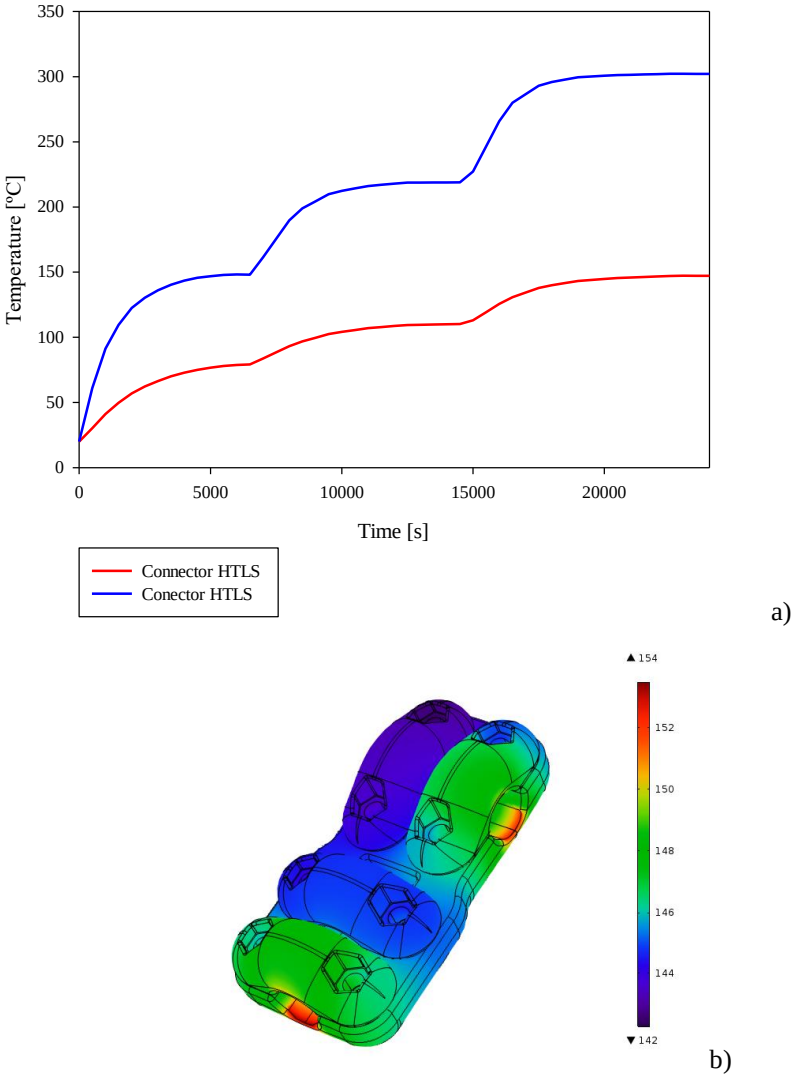

Figure 1.3: Results of the 3D-FEM thermal simulation of the temperature rise-test. a) Evolution of temperature of the conductor and the connector for the three levels of current applied ($I_{100\%}$=1275A, $I_{125\%}$=1721A, $I_{150\%}$=1913A). b) Temperature distribution on the HTLS connector at the third level $I_{150\%}$=1913A of current.

The other specification connectors must support is related with short-circuit phenomena. Short-circuits are sudden fault events which make current to rise abruptly. These events produce superlative thermal and mechanical stresses. Power networks are protected against these events by means of switching devices [8]. Nevertheless, these devices take a time to actuate, usually of around 1s. During this time, it is necessary to ensure that the characteristically high circulating currents of the short-circuit do not compromise the electrical equipment involved. It is accepted that the service life of electrical hardware can be improved by reducing the temperature achieved after a short-circuit incident. Thus, it is of remarkable interest for manufacturers to reduce this temperature and so, to have methods for reproducing these tests and measuring this temperature.

The standard that defines the test methodology for short-circuit events is the IEC 62271-1:2007 [9]. The test current is determined by the characteristics of the network where the connectors are installed. For instance, the connectors studied in this thesis are tested to resist a short-circuit current of 50 kA and a peak current of 125 kA during 1 second. To pass the test, the temperature of the connector must be below the one of the conductor during the test. Also, no significant mechanical deterioration must be seen after the test. Finally, the rise of resistance of the connector after the short-circuit, if exists, cannot excess by 20% the original resistance of the connector.

1.1.4.2 Problems of standard validation of the thermal specifications

1.1.4.2.1 Temperature rise test

Temperature rise tests are performed using high-currents transformers. These transformers have a secondary winding designed to provide currents in the range of thousands of amperes at voltages around 10 V. The transformers usually installed in manufacturer facilities are in many cases on top of their capabilities in terms of current use.

Temperature rise test loops face the problem of being also very inductive, so in many times, and especially when testing large arrangements, the maximum available current is below the specified by the transformer manufacturer. In order to approach the upcoming problem of testing substation connectors aimed to work at higher currentrates, due to the use of HTLS conductors, *Chapter 2* of this thesis proposes a methodology to reproduce temperature rise tests by means of reduced-scale samples. By this way, temperature-rise tests can be performed at all the levels demanded by the standard, but using considerably less current. This strategy will allow manufacturers to test their products using the equipment that already have.

1.1.4.2.2 Short-circuit test

Short-circuit tests face bigger difficulties to be performed in industrial facilities. The values of current necessary to perform such tests require the use of very large transformers and the access to very demanding power sources. To illustrate, the high-voltage laboratories that perform short-circuit tests have a power substation for their own use. Hence, for most manufacturers these facilities are unaffordable or uneconomical to maintain.

Short-circuit tests are costly, and usually, manufacturers face long waiting times to perform them as the laboratories with capability to perform these tests are scarce. Thus, the second part of *Chapter 2,* proposes a methodology to carry out these tests at a reduced scale for product optimization purposes. The approach shown in the following lines lets product designers to perform such tests by means of power transformers with similar characteristics to those used in temperature rise tests, see Figure 1.4. Also, the use of small scale connectors eases the process of assembling the tests. Furthermore, insourcing short-circuit tests lets designers to get more insight about the physical processes occurring during short-circuit as tests are prepared and controlled by themselves.

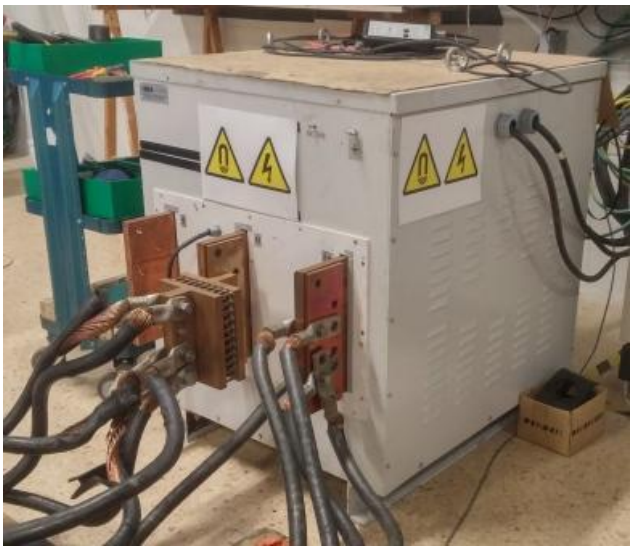

Figure 1.4: High-current transformer used in Temperature rise tests and reduced-scale short-circuits

1.1.4.3 Corona specifications and design of substation connectors

Substation connectors work at very high levels of voltage, in a dielectric media, the atmospheric air. The properties of air vary notably depending on different factors such as the weather, humidity, air-pollution, temperature and height (pressure) above the sea-level. Connectors are dimensioned to work at a determined level of voltage and at a specified distance from the ground-plane. If connectors are not properly designed, the air surrounding the most stressed parts of the connector becomes ionized, thus appearing the Corona effect. The ionization of air occurs because the electric field in some parts of the connectors can sometimes surpass a critical or threshold value, known as corona inception field. The electric field on the surface of the connector depends apart from the properties of air, on applied voltage, ground distance and curvature of the connector surface. Small radiuses of curvature lead to high values of electric field [10] and so, the proper design of the curvature of the connector is of paramount importance when designing substation connectors. The effects of corona are variate and always not desired. Some of the effects are ozone generation, audible noise, electromagnetic interference and power loss [11]–[13]. The specificities of corona and the effects are discussed in more detail in *Chapter 3*.

3D-FEM techniques are used in order to design corona-free substation connectors. Using these tools, it is ensured that the electric field strength on the surfaces of connectors does not surpass a threshold level for the specified voltage level of the connector. This threshold value is related to the electric breakdown of air, and usually industry designs the connectors with a high security margin. Figure 1.5 shows the flow diagram followed to design corona-free connectors.

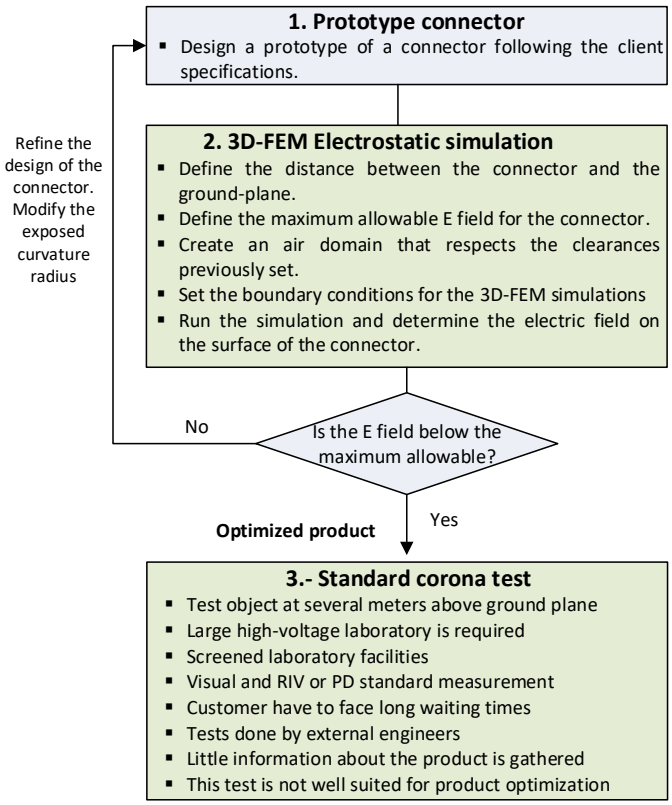

Figure 1.5: Flow diagram of the design process of corona-free connectors [14]

1.1.4.4 Standard validation of corona specifications and problems

Substation connector designs are validated according to the ANSI/NEMA CC1-2009[3]. This standard normalizes the heights above the ground plane at which connectors must be tested for a given voltage, as seen in Table 1.1. Also, for hardware intended to work in three-phase lines, the standard introduces the values of nominal phase spacing.

Table 1.1: Phase Spacing and Height Above Ground as a function of the Nominal Operating Voltage According To ANSI/NEMA CC1-2009 [3]

Nominal voltage (kV_{RMS})	Phase spacing (m)	Height above ground plane (m)
230	3.4	4.6
345	4.9	7.6
500	7.6	9.1
765	13.7	13.7
1100	16.8	16.8

Corona tests are carried out in screened laboratories that can reproduce the clearances between the connector and the ground-plane and the walls. Figure 1.6 shows an example of screened high-voltage laboratory. These laboratories are scarce and the equipment to elevate the voltage and the measuring instrumentation are very expensive. So, few electrical hardware manufacturers are able to have these facilities integrated in their industrial plants.

Figure 1.6: Screened high-voltage laboratory [15]

During the optimization stage it is unaffordable to test the corona behaviour of all the different prototypes generated. Also, before testing connectors on independent facilities for certification purposes, there is no economical way to internally validate the designs. In order to tackle this problematic, *Chapter 3* of this thesis introduces two systems to perform low-cost corona tests. Both systems use commercial digital cameras to detect the visual coronas. Thus, they avoid the use of expensive partial discharge (PD) measuring systems or the necessity of having a totally screened laboratory. Furthermore, both approaches mix 3D-FEM electric field simulation with experimentation at low height from the ground. Hence, they make it possible to recreate the corona tests in small laboratories making use of affordable industrial high-voltage generators.

1.1.4.5 Mechanical specifications of substation connectors

Substation connectors combine two functions. The first one is ensuring the electrical path along the power lines. The latter is to structurally support the substation. So, it is important for manufacturers to guarantee that connectors are able to resist the mechanical solicitations that later will face under real working conditions. The standard ANSI/NEMA CC1-2009 [3], considers two types of stresses, traction and torque-strength, in order to validate the mechanical properties of connectors.

1.1.4.6 Standard validation of mechanical specifications and problems

The ANSI/NEMA CC1-2009 [3] standard specifies that the minimum tractive stress for substation connectors is a function of the cross-section of the conductor. Table 1.2 summarizes the testing values of tractive force depending on the section of their conductors.

Table 1.2: Minimum tractive force for substation connectors. According To ANSI/NEMA CC1-2009 [3]

Cross-section (mm^2)	Tractive force (N)
(16-50)	1334
(70-95)	2224
(120-240)	4448
(240 and above)	8896

On the other hand, substation connectors' resistance to torque-strength applied by bolted unions is tested by gradually applying a torque-strength 50% higher than the nominal one. No deformation of the connector must be seen during or after this test. The nominal torque-strength applied to bolted unions depends on the material and metrics of the bolts, which is shown in Table 1.3.

Table 1.3: Torque-strength applied to bolted-unions according to ISO 3506-2009 [16]

Materials	M8	M10	M12	M14	M16
Aluminium alloys	10	20	40	60	90
Stainless steel	15	35	60	90	140
Zinc-coated steel	20	45	78	120	180

Due to its simplicity, and because the machinery necessary to perform mechanical tests is affordable, manufacturers carry out mechanical tests in their facilities. Therefore, there is no industrial interest in finding new ways of performing these tests. Also, HTLS substation connectors face similar mechanical solicitations as the connectors installed nowadays. So, the methodologies used to test their mechanical performance are well-suited for HTLS substation connectors. For this reason, it is out of the scope of this thesis to develop new mechanical tests for HTLS substation connectors.

1.1.4.7 Lifetime specifications of substation connectors

Substation connectors are intended to work during all the working life expected for the substations where they are installed. In general, substation connectors are expected to work at least 40 years since installation.

The principal source of ageing of connectors is the deterioration of the contact interfaces. Contact interfaces are the parts where the aluminium-aluminium junctions between conductors and connectors take place. Contacts are imperfect and so, current is forced to pass through few points of these contacts, which are known as a-spots. The constriction of current lines is commonly known as the contact resistance. The contact resistance depends on the smoothness of the surface, on the presence of aluminium oxides (alumina) and the contact pressure. Through operation time, contact interfaces face loose of pressure of the contacts and infiltration of contaminants. These effects tend to rise the contact resistance of the connector, which increases the working temperature.

Temperature is known as the principal accelerator of the ageing of contacts, as the chemical reactions taking place between the contacts become accelerated. Therefore, in order to design connectors able to survive during all their expected working life, it is a task of designers to have insight about how the resistance will evolve along time.

1.1.4.8 Standard validation of lifetime specifications and problems

Substation connectors behaviour through time is nowadays validated following the methodology proposed by ANSI/NEMA C119.4 [17]. The standard proposes to perform a set of temperature cycles on a sample of substation connectors. The number of these cycles depends on the type of connector.

The experience obtained in Amber laboratory and the opinion of other authors [18], suggests that the results obtained from the standard tests, are not useful to obtain relevant conclusions about connectors life. Specifically, for a T-connector like the one seen in Figure 1.3b, the standard proposes to carry out 125 temperature cycles, where the temperature of the conductor attached to the connector rises 100ºCabove the ambient temperature. Considering that the working temperature of HTLS connectors is around 150ºC, this test is insufficient at all effects. Also, considering that the tested product is intended to be in service up to 40 years, and that no full deterioration of the connector is seen through the test, it results somewhat arbitrary to consider that the design is good, based only in the fact that its resistance does not rise more than 5% after 125 cycles.

For all of the above explained, this thesis introduces in *Chapter 4* a methodology, the step-stress accelerated degradation tests (SSADT), to test substation connectors based on to apply high thermal stresses, in order to accelerate the deterioration processes.

1.1.5 Improvements introduced in HTLS substation connectors

In parallel to the work of this thesis, and within the Superconnector project, HTLS substation connectors have been developed. The focus of the redesign of the connectors has been put in the modification of the connectors materials in order to make them able to work up to the temperature levels at which HTLS conductors operate. Also a special effort in the understanding and treatment of the contact interface has been done as its behaviour has an enormous influence on the final temperature of the connectors. Moreover, as any other connector, HTLS connectors have been designed to resist the mechanical solicitations and to be corona free [5], [6].

1.1.5.1 Alloy selection and treatments

Substation connectors, designed to be installed with AAAC conductors, are manufactured using A356.0 aluminium alloy. This alloy is suitable for producing connectors by sandcasting. The elements and proportions of the alloy are shown in Table 1.4.

Table 1.4: A356.0 alloy composition

Element	Percentage	Element	Percentage
Aluminium, Al	91.1 - 93.3 %	Others, each of them	<= 0.05 %
Copper, Cu	<= 0.20 %	Others, total	<= 0.15 %
Iron, Fe	<= 0.20 %	Silicon, Si	6.5 - 7.5 %
Magnesium, Mg	0.25 - 0.45 %	Titanium, Ti	<= 0.20 %
Manganese, Mn	<= 0.10 %	Zinc, Zi	<= 0.10 %

Basically, the two preponderant elements of the alloy are aluminium and silicon. In order to vary the properties of the alloy, the modification of the silicon is a common practice to refine the eutectic structure of the A356.0 alloy. As a way to work at the regimes of temperature of HTLS conductors, an improvement in the electrical and mechanical properties of the aluminium alloy was desired. References [19]–[21], suggested that the addition of strontium, Sr would result in a modification of the microstructure of the silicon inside the aluminium for the application in HTLS substation connectors. The modification of the alloy based in addition of Sr enhances the conductivity of the alloy.

In order to improve the mechanical behaviour of the alloy, a study of the different heat treatments applicable to the alloy was performed. From all of them, the T6 heat treatment was the most suitable in terms of improving the mechanical and electrical properties of the alloy. The treatment, depicted in Figure 1.7, consists of a solution phase where the temperature of the alloy is elevated, a quenching, and a precipitation stage after the quenching at a temperature lower than that used during the solution temperature phase [22].

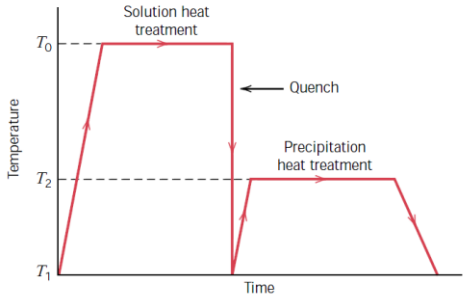

Figure 1.7: Heat treatment T6: solution, quenching and precipitation [22]

Experimental results [23] show a decrease of about 15% of the resistivity of the A356.0 due to the modification of the alloy and a rise of around 40% of the break load values. The decrease of resistance is of notable importance as HTLS connectors would behave better under higher current stresses. At the same time, the rise of average break load involves a higher security margin for an alloy that is intended to work at a much higher temperature.

1.1.5.2 Contact resistance in substation connectors and improvements

Although the results of the modification of the alloy are important, the main resistance source of a connector is the contact resistance. This is the resistance due to the constriction of current lines that happens when electrons cross between two contact surfaces through the small spots, known as a-spots, where contact is effectively set. This resistance is especially significant in aluminium contacts. On the surface of aluminium, a layer of alumina, a non-conductive oxide of aluminium, is formed whenever the aluminium gets in contact with atmospheric air. Therefore, it is a priority to eliminate as much as possible this layer in order to facilitate the conduction through the contacts. Usually, this problem has been attained by brushing the contact surfaces meanwhile a conductive grease protective layer that blocks the development of the alumina layer is applied. Albeit the results of this technic are quite good, it only eliminates a part of the alumina of the contact. Therefore, in a parallel work, a new chemical cleaning technic was proposed to completely eliminate the alumina layer [24].

Table 1.5 shows comparative results of the contact resistance of connectors with different surface treatments, that is, with no treatment, brushing and application of conductive grease, and chemical cleaning and application of conductive grease.

Table 1.5: Summary of the improvements of the chemical modification of the alloy and the application of heat treatments

Treatment	Connector surface treatment	Conductor surface treatment	Average contact resistance [μΩ]	Connector resistance [μΩ]
1	No treatment	No treatment	29.31	7.15
2	Brushing + conductive grease	Brushing + conductive grease	5.93	
3	Chemical cleaning + conductive grease	Brushing + conductive grease	2.67	
4	Chemical cleaning + conductive grease	Chemical cleaning + conductive grease	4.65	

As seen in Table 1.5, when the contact surface is not treated, the contact resistance can be about 4 times the resistance of the connector. From the rest of the solutions shown, the best is the third, as the contact resistance values obtained is reduced to almost a third of the resistance of the connector. Compared with treatment 2, which is the one used nowadays, the contact resistance can be decreased by half. Contact resistance minimization is of paramount importance when designing aluminium hardware. Figure 1.8 depicts the result of a negligently installed substation connector. No conductive grease was placed within the contact interface and the temperature of the connector reached levels above the melting point of aluminium.

Figure 1.8: Failed substation connector.

1.1.5.3 Conclusions about HTLS substation connectors development

The common approach for the design of a new connector under harder thermal specifications, would be the increase of its mass and/or surface. Nevertheless, the development of HTLS substation connectors performed by Capelli [23], for the Superconnector project, has been centred on the modification of the materials and thermal and surficial treatments applied. By this way, a connector of the same size and ease of manufacture and install was designed. The modifications and treatments performed on the connector are not costly nor require complex technologies to be applied. Thus the unit cost of the connector is not remarkably affected. Furthermore, the application of such modifications do not require important investments in machinery acquisition, sandcasting moulds or production plant modifications. Hence, the proposed HTLS connector is a satisfactory solution in terms of both technical and economic feasibility.

1.1.6 Restrictions on scale-reduction

The reduced scale is defined as the ratio between the physical dimensions of the original connector and the reduced scale one. This ratio is mainly restricted by the availability of materials. First, the connectors have to fit in commercially-available HTLS conductors. Specifically, for the pair of connectors considered in this thesis (see Figure 1.9), the reduced-scale connector (RS), has been designed to fit in a GTACSR131-19 conductor which was the smallest HTLS conductor available on the market. On the other hand, the original-scale one (OS) uses a GTACSR 464 CONDOR conductor which was the largest one available.

The second market constriction is related to screws metrics. The metrics for the OS connector is M10 whereas the smallest that fitted the RS connector uses M6. As a result, the connectors have a scale relationship of 1:1.745. Annex 1 and 2 show relevant data of the dimensions of conductors and connectors at different scales.

Figure 1.9: Two scales of the S285TLS connector

1.1.7 Justification and scope of the thesis

The development of the HTLS conductors is a revolutionary solution in terms of assuring the supply of power in a world where the power demand does not cease to increment. The deployment of HTLS conductors in the following years supposes a challenge in terms of redesigning the hardware attached to them. Specifically, substation connectors are designed for thermal loads of between 70ºC to 90ºC. These products are validated nowadays following a set of international standard tests. The new designs of HTLS substation connectors lack of the set of testing methodologies necessary to check their performance under the superior current loads associated with the use of HTLS conductors. Also, the fact that these are intended to work under harsher conditions, makes them more difficult to be tested in industrial facilities. Manufacturers are interested in avoiding to outsource tests related with the design of these products. These tests intended to be performed to products under development not always return satisfactory results and having them insourced represents an invaluable source of knowledge for the product-development departments of hardware manufacturers. Also, outsourcing tests of prototypes is in many cases unaffordable due to the elevated costs and the time involved on them.

For all of the previous, this thesis develops a set of tests based either on the use of reduced-scale samples or the study of methodologies that reduce the overall requirements or the time to obtain reliable data. These tests pretend to bring a new scope to substation connector testing, and in general, to high power hardware design. The methodologies explained in these lines are already applied by SBI Connectors SAU, the partner with whom this work has been developed. The tests in which reducing the scale has been considered of utility, are thermal (temperature rise and short-circuit), thermal-ageing and corona tests. The development of a methodology for the performance of mechanical test based on reduced-scale connectors does not provide any relevant improvement in terms of cost-drop, ease of test performance or increase of the quality and quantity of the data obtained after the tests. Thus, these tests are out of the scope of this thesis.

As a conclusion, the fact that the tests proposed in this thesis are already used by a connectors manufacturer, justifies the effort in developing such methodologies. Also, the significant number of publications in relevant congresses and journals, listed in *'1.3 Thesis publications*, about the topics explored in this thesis suggests that the work has been found to be relevant by many independent researchers related with the power industry.

1.2 Objectives

This thesis develops a set of methodologies to test connectors for HTLS conductors. The scope chosen to successfully test these products is to develop reduced-scale tests, which are based on the already existing standard tests for regular substation connectors for current power lines. Several criteria for considering the test design as successful are taken into account. First and foremost, the data obtained in such tests should be extrapolable to the one obtained at full-scale. Also, time, monetary cost and facility simplification are among the desired criteria to design such tests.

The newly developed tests have to be based on the existing international standards for substation connectors [3], [17]. Particularly, the developed tests aim to obtain the same information obtained nowadays for current substation connector. They include the temperature rise test, thermal-ageing test, short-time withstand current test (short-circuit test) and corona test.

Concluding, the thesis is focused to develop new reduced-scale tests for HTLS substation connectors taking into account all the factors that will emerge when reducing the size, related both to heat transfer and electro-magnetic points of view. The thesis aims also to critically review existing testing procedures and propose, if necessary, new ones.

Summarizing, the objectives of the thesis are the following:

- Present the state of the development of HTLS technology and specifically of the HTLS substation connectors.
- Formulate the scale-relationships necessary to reproduce temperature rise tests (TRT) at a reduced-scale and in an affordable way. Validate the results by means of simulation and experimentation.
- Formulate the scale-relationships necessary to reproduce the short-time withstand currents tests (STWCT) at a reduced-scale and in an affordable way. Validate the results by means of simulation and experimentation.
- Develop the methodology to perform corona tests at a short distance from the ground-plane. Validate the results by means of simulation and experimentation.
- Develop the equivalence methodologies between corona tests performed using different scale samples. Validate the results by means of simulation and experimentation.
- Review the ageing tests methodologies and propose new approaches to determine the reliability of substation connectors. Experimentally validate a new approach for ageing testing.

1.3 Thesis publications

Several works have been published during the consecution of this thesis. These are shown in the following sub-sections.

1.3.1 Conferences

Table 1.6: Works presented in notable conferences

Name of conference	Name and Year	Authors
IEEE International Conference on Power System Technology	'Transient thermal modelling of short-circuit test for conductors by means of dimensional reduction', September 2016	C. Abomailek, F. Capelli, J.-R. Riba, M. Moreno-Eguilaz.
IEEE International Conference on Power System Technology	'Analysis of electrical contact resistance models for substation connectors', September 2016	F. Capelli, C. Abomailek, J.-R. Riba, J. Sanllehí.
Cigré, Session 46	'Reduced scale feasibility of temperature rise tests in substation connectors', August 2016	C. Abomailek, J.-R. Riba, P. Casals-Torrens.

1.3.2 Journals

Table 1.7: Journal articles written during the development of this thesis

Name of publication	Name and Year	Authors
IET Generation Transmission & Distribution	'Simplification and Cost Reduction of Visual Corona Tests', February 2018	J.-R. Riba, C. Abomailek, F.Capelli, P. Casals-Torrens
Measurement	'A 3D-FEM-based model to predict the electrical constriction resistance of compressed contacts', September 2017	J.-R. Riba, A. Mancini, C. Abomailek, F. Capelli
IET Generation Transmission & Distribution	'Fast Electro-Thermal Simulation of Short-Circuit Tests', July 2017	C.Abomailek; J-R. Riba; F. Capelli; M. Moreno-Eguilaz
Applied Thermal Engineering	'Transient thermal modelling of substation connectors by means of dimensionality reduction', January 2017	C. Abomailek, F.Capelli, J.-R. Riba, P. Casals-Torrens
Experimental Heat Transfer	'Application of reduced scale tests to improve the thermal performance of high-voltage substation connectors' (Under review)	C. Abomailek, J.-R. Riba, P. Casals-Torrens
IET Generation Transmission & Distribution	'Feasibility Analysis of Reduced-Scale Visual Corona Tests in High Voltage Laboratories' (Under review)	C. Abomailek, J.-R. Riba, P. Casals-Torrens

1.3.3 Patents

Table 1.8: Technologies patented from the work presented in this thesis

Type of patent	Name and Year	Authors
National patent	'Test procedure for the performance of corona visual with reduced voltage', June 2018	J-R. Riba; C.Abomailek; J. Sanllehí; F. Capelli; J. Pérez.

2 THERMAL TESTS

2.1 State of the art

2.1.1 Power losses due to Joule heating

2.1.1.1 Description of the phenomenon

The Joule heating designates the process by which the energy of an electric current is transformed into heat as it flows through a body. On a microscope scale, it occurs whenever a current flows through a finite-conductivity body. The circulating electrons impact with the atoms of the conductor. The released energy is dissipated, thus increasing the temperature of the conducting body.

2.1.1.2 Quantification of the magnitude order of Joule effect losses in power lines

Many heating applications are based on Joule heating. Nevertheless, in power transmission systems, this process represents one of the major sources of loss, thus impacting their efficiency.

$$P = I^2 R \tag{2.1}$$

Joule heating depends on *I*, the applied current, and *R*, the resistance to the pass of current through the conducting body (2.1). The current has a quadratic weight. This is this reason why power transmission is carried out at high-voltage levels. By this way, it is possible to decrease the current circulating through the network and, therefore, the necessary section of conductors.

Nowadays, the working temperature of power conductors is between 70-90ºC under rated operating conditions, depending on their section and ampacity. Thus, the temperature-rise of power system components from ambient temperature to working temperature is a significant loss of the power involved in power systems.

One could propose that voltage could be raised at a much higher level in order to reduce the electric current almost to 0 A. Unfortunately, this is unfeasible due to the uprising of losses in form of corona effect, thus requiring huge supporting towers, insulator chains and other elements, which makes the power system more complex and expensive. This sort of losses appear whenever voltage levels are close to the breakdown value of the surrounding dielectric medium, atmospheric air for the case that attains substation connectors.

2.1.2 Power losses due to eddy currents

Eddy currents are loops of electric current induced within conductors produced by a changing magnetic field in the conductor. They are described by the Faraday's law of induction. Eddy currents flow in closed loops within conductors, in planes perpendicular to the magnetic field.

As described by the Faraday-Lenz Law (2.2), the existence of a variable magnetic field close to a surface induces an opposing current inside the conductor that generates a magnetic field, which opposes to the first one. These parasite currents, known as eddy currents, contribute to the heating of conductors via the Joule effect. Therefore, this charge movement worsens the thermal performance of conductors.

$$\oint_C \vec{E}\cdot\vec{dl} = -\frac{d}{dt}\int_A \vec{B}\cdot\vec{dS} \qquad 2.2$$

The magnitude of the current in a given loop is proportional to the strength of the magnetic field, the area of the loop, and the rate of change of flux, and inversely proportional to the resistivity of the material [25].

Eddy currents often involve both skin and proximity effects.

2.1.2.1 Skin effect losses

An alternating current in a conductor produces an alternating magnetic field in the surroundings and inside the conductor. As Faraday-Lenz Law describes (2.2), the variation of a magnetic field due to a change of an electrical current, produces an opposing electric field to counteract the change of current. This opposing field is stronger at the centre of conductors. This forces the conducting electrons to move at the outer or skin section of the conductor. Thus, the conductor's effective section can be largely decreased, since the current is not distributed homogeneously across the section of the conductor. This effect increases the effective resistance of conductors (2.3) [25].

$$R = \rho_e \cdot \frac{Length}{S_{effective cross-section}} \qquad 2.3$$

The skin effect increases the alternating current (AC) resistance of power conductors because it reduces the effective section, thus increasing power losses via Joule effect, as seen in Figure 2.1. Due to its dependence on the change of magnetic field, it is strongly affected by the frequency of the alternating current. Nevertheless, this thesis is focused in electrical distribution accessories. Therefore, the frequency considered during all calculations will be 50Hz, the standard distribution frequency of Europe.

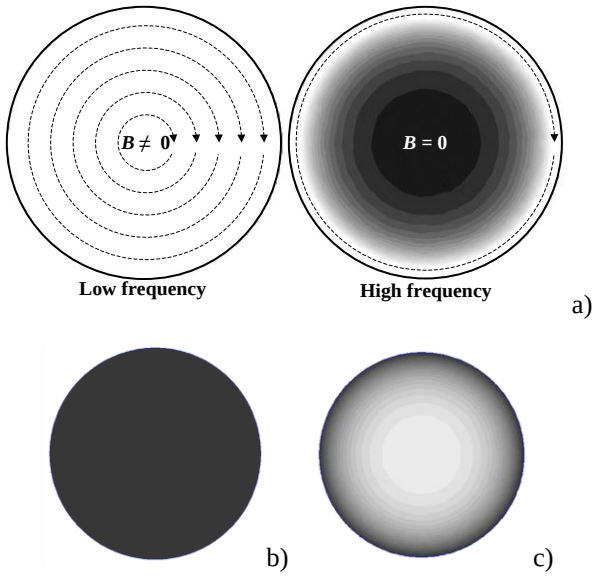

Figure 2.1: a) Cross-section of a cylindrical conductor carrying a current *I* flowing in the perpendicular plane of the drawing. b) 50 Hz current density distribution on an isolated aluminium conductor. c) 10 kHz current density distribution on an isolated aluminium conductor.

2.1.2.2 Proximity effect losses

Finally, the last effect in conductors due to the interaction of electric and magnetic alternating fields is the proximity effect. Whenever two conductors are close to each other, the magnetic field generated by one conductor modifies the distribution of charge in the other (see Figure 2.2). This provokes a concentration of current density in one side of the conductor, thus reducing once again the effective section of the conductor and increasing the AC resistance of the conductor and hence the losses due to Joule effect [25].

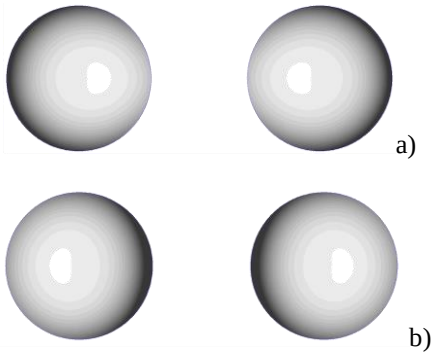

Figure 2.2: a) Proximity effect in two conductors carrying alternating currents of the same polarity $f = 10$ kHz. b) Proximity effect in two conductors carrying alternating currents of the opposite polarity $f = 10$ kHz

2.1.3 Temperature rise tests

2.1.3.1 Standard test-description

The ANSI/NEMA CC1-2009 standard describes the most extended approach towards the performance of the temperature rise test [3]. The aim of the test is to determine the substation connector thermal behaviour under transient and steady-state conditions. Therefore, it is carried out to check the suitability of the design of a connector for a determined thermo-electric load. The temperature rise test on electric power connectors may be conducted either indoors or outdoors, at the choice of the manufacturer. The applied current shall be 100, 125, and 150% of the rated current, reaching the equilibrium at each of the current levels. Equilibrium is described in the standard as the constant temperature (+/-2ºC) acquired during three successive measurements taken five minutes apart.

Measurements are made at the end of the first 30 minutes and at one-hour intervals thereafter until completion of the test. The rated current shall be in accordance with the ampacity of the conductor attached to the connector. Heat sinks or hot spots are avoided on the test loop, procuring that conductors of the correct size and type have a length from each opening of the connector to the point where the connection is made to the circuit of, at least, 8 times the conductor diameter (but never less than 1.2m) (see Figure 2.3).

Furthermore, the standard defines specific test conditions for different connector typologies:

a) Terminal connectors: Test current shall be either the current rating of the equipment to which the connector is connected, or the current rating of the conductor for which the opening is designed, whichever is lower.

b) Angle and straight connectors: Test current shall be selected as a function of the conductor that has the lower current-carrying value where the openings of the connector are of two sizes.

c) "T" connectors: Test current shall be based on the conductor having the lowest current rating in the assembly.

ANSI/NEMA CC1 [3] imposes that the temperature rise of the tested electric power connector does not exceed the temperature rise of the conductor with which it is intended to be used. For the case of connectors that join two conductors of different size, the rise of temperature shall not exceed the temperature rise of the conductor having the highest temperature rise.

Figure 2.3 shows the setup used in AMBER laboratory of the Universitat Politècnica de Catalunya to conduct temperature rise tests.

Figure 2.3: Temperature rise test assembly for substation connectors

2.1.4 Short-circuit tests

2.1.4.1 Standard test-description

Power systems have to be designed and tested in such a way that it is guaranteed that devices involved can withstand a short-circuit current. These currents appear under violent failures of network, due to natural disasters or negligence, and can compromise the integrity of the whole network. Connectors, being the weakest part of the power network, and the ones that have the function of being the nexuses with power conductors or bus bars, have to withstand such current surges.

Short-circuits produce both electromechanical and thermal effects, so when analysing short-circuit consequences, both effects must be considered. Power devices have to be tested and certified in accordance to the IEC 60694-2002 standard [26] (see Figure 2.4), which refers to the short-circuit tests as short-time withstand current and peak withstand current tests. The standard value of rated short-time withstand current is specified in the IEC 60059 [27], and shall be equal to the short-circuit rating assigned to switchgear and control gear, while the rated peak withstand current, for a frequency of 50 Hz, is equal to 2.5 times the rated short-time withstand current. The standard duration of short circuit is 1s. If it is necessary, a value lower or higher than 1s may be chosen (most used values are 0.5 s, 2 s and 3 s). To verify that the connector has not suffered significant damage due to the test, it has to accomplish two main requirements:

1. No-load operation of the mechanical switching device shall be performed after the test, and the contacts shall open at the first attempt.
2. Resistance of the main circuit shall be measured. When the resistance increase is more than 20 %, and if it is not possible to confirm the condition of the contacts by visual inspection, an additional temperature-rise test should be performed.

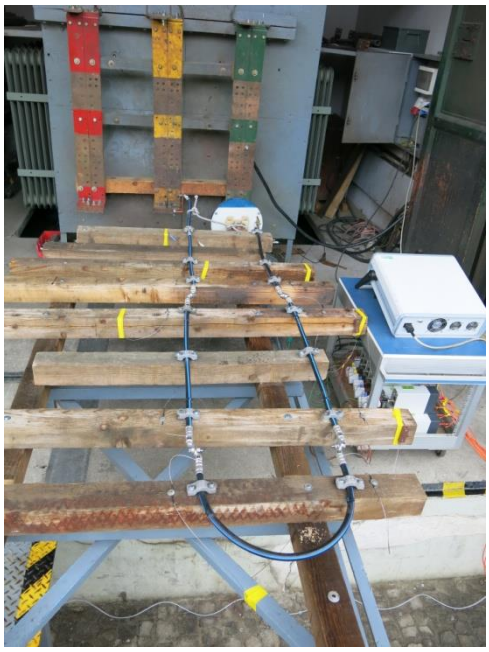

Figure 2.4: Short-circuit test assembly for low voltage connectors

2.1.5 3D-FEM electro-thermal modelling of substation connectors

3D-FEM (three-dimensional finite element method) is a recognized and flexible simulation tool to accurately simulate the thermal behaviour of 3D devices such as connectors [28], bus bars, or power transformers [29] among others. This research makes use of this methodology to perform a Multiphysics electric-thermal analysis using the commercial Comsol® software [30]. The system of equations briefly described in the following lines is solved each time-step. Also, the values of physical properties are refreshed at each of the time-steps to reflect its dependency with respect to the temperature. Figure 2.5 displays the mesh of the full scale substation connector analysed in this work.

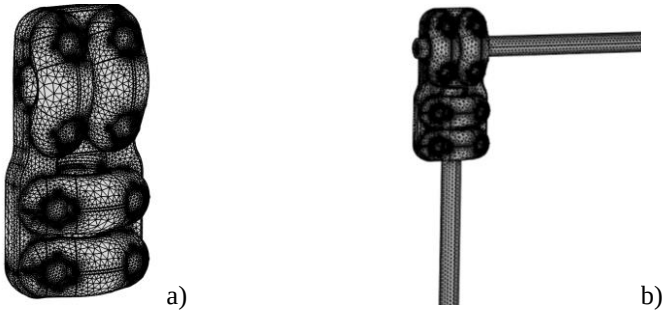

a) b)

Figure 2.5: a) Mesh of the S285TLS substation connector analysed in this work, consisting of 914486 domain elements, 176608 boundary elements and 26339 edge elements. b) Mesh of the S285TLS substation connector and the related GTACSR 464 HTLS conductors.

First, the electric field and the current density is calculated solving the Maxwell equations as in (2.4) and (2.5),

$$\vec{j} = \frac{\vec{E}}{\rho_e(T)} \quad 2.4$$

$E = -\nabla V$	2.5

Power losses per unit volume ($W \cdot m^{-3}$) are calculated as,

$$\dot{q}_e = \vec{j} \cdot \vec{E} = \rho_e \vec{j} \cdot \vec{j} \quad 2.6$$

It is noted that $\dot{q}_e$ is the heat source in the heat conduction equation [31],

$$\rho c_p \frac{\partial T}{\partial t} = -\vec{\nabla} \cdot \vec{q} + \dot{q}_e \quad 2.7$$

By considering the electrical resistivity $\rho_e(T)$ to be temperature-dependent, (2.7) results in,

$$\rho c_p \frac{\partial T}{\partial t} = k\nabla^2 T + \rho_{e,293K}[1 + \alpha_e(T - 293)]\vec{j} \cdot \vec{j} \quad 2.8$$

Simulations consider isotropic materials and ρ, k and Cp as temperature-dependent, although they don't notably change for the working temperatures range of substation connectors.

To set the initial condition of the thermal analysis, it is supposed that the test object has been acclimated to the conditions of the indoor area of test. The boundary condition at the solid/air interface including natural convection and radiation with the external ambient can be expressed as [32],

$$-\vec{n} \cdot (-k\nabla T) = h(T_{air,\infty} - T) + \varepsilon\sigma(T_{air,\infty}^4 - T^4) \quad 2.9$$

$\vec{n}$ being the unit vector normal to the solid/air boundary.

Due to the complex physical phenomena involved [33], convection cooling is often analysed from experimental data supported by dimensional analysis. The convective heat transfer coefficient h is assumed to be temperature dependent, thus being recalculated at each iteration of the FEM simulations. More details about the calculation of h and the 3D-FEM mode in general is found in [28].

2.1.6 Fast simulation methodologies for thermal behaviour study

2.1.6.1 Aim and introduction

During the last years, the finite element method (FEM) has been widely applied to design electrical devices. Two- and three-dimensional (2D and 3D) multiphysics FEM simulations are recognized as a realistic means to predict the electromagnetic and thermal behaviour of diverse type of electrical devices. Different authors have struggled to develop coupled electromagnetic-thermal 2D- and 3D-FEM formulations to predict the thermal behaviour of diverse electrical components such as conductors, bus bars, cables, connectors or semiconductors among others [34]–[42]. Despite significant improvements in computer performance, 3D-FEM simulations are still time-consuming and memory-intensive due to the heavy computational resources involved to provide the required resolution for complex 3D multiphysic problems [43]. It can cause serious difficulties, particularly when applying recursive simulations during the design optimization stage [44]. The use of 3D-FEM simulation tools often requires the use of costly licenses and the implication of specialized engineers to carry out tedious and time-consuming tasks associated to the preparation of 3D geometries, generation of the 3D mesh, or settling of boundary conditions among others. Therefore the development of accurate fast models [45] which can be based on model reduction techniques [46], are highly appealing to overcome the abovementioned drawbacks.

This section proposes a one-dimensional fast method based on nodal equations and finite differences formulation to accurately predict the temperature evolution in substation connectors during the standard temperature rise test. This is a multiphysics electromagnetic-thermal problem. The main heat source is the Joule loss due to the electric current, whose time-profile is known, although there is a minor contribution due to the induced eddy currents. The proposed method discretizes the analysed domain in finite one-dimensional regions in which the energy rate balance due to the flow of heat is calculated. To accurately predict the temperature profile along the connector and the surrounding conductors, the proposed transient model takes into account the three-dimensional geometry of the analysed system to determine for each discretized element and at each time step different parameters, such as the incremental electrical resistance or the convective coefficient. It is worth noting that the proposed approach can also be applied to simulate the temperature rise of other power devices.

To evaluate the accuracy of the proposed system, two substation connectors are evaluated and the standardized temperature rise test according to the ANSI/NEMA CC1-2009 standard [3] is simulated and checked against experimental tests. According to this standard, the connector passes the test if its temperature is below the temperature of the conductors at with which the connector is associated. This test is very useful since it allows evaluating the thermal behaviour of the substation connectors under both transient and stationary conditions. Temperature rise tests are expensive since they last for long time, and consume large amounts of electrical power. As a result, to obtain designs with optimal thermal performance [47], manufacturers of substation connectors require fast, easy-to-use and accurate simulation tools to anticipate the results of the mandatory standard temperature rise tests.

The finite difference method (FDM) is a recognized tool to approximate the solutions of systems governed by differential equations by means of finite differences calculated at the grid points of a discretized geometry. The FDM method has been widely applied in the technical bibliography, for example to model the heat transfer in solar cells by applying the energy conservation principle [48], calculate the natural convection heat transfer in a cavity filled with a nanofluid [49], [50], determine the temperature rise of a surgical drilling machine [51], model the transient thermal performance of machining processes [52], predict the temperature distribution of ball-screw mechanical systems [53] or to perform vibrational analysis in elastic media [54].

Most of the works are based on two- or three-dimensional FDM approaches. It is shown that by using a one-dimensional FDM reduction by considering the whole three-dimensional geometry in calculating key parameters for the energy conservation laws it is possible to obtain very accurate results, similar to those attained with 3D-FEM, which is the current way to solve this kind of problems [28], but with much less computational burden. As a consequence, the method here proposed can be very useful to optimize in an economical and fast manner the design of different power devices including substation connectors, power conductors, bus-bars or fittings used in power lines among others to ensure an improved thermal behaviour.

2.1.6.2 Problem discretization

The temperature of the connector is directly related to the temperature of the reference conductors at which it is connected. Due to the longitudinal geometry and heat conduction of the considered problem, the thermal analysis can be reduced to a one-dimensional problem by formulating suitable assumptions. To this end the whole domain is divided into several discrete elements called nodes, along the axial and main dimension of the geometry, as shown in Figure 2.6. The axial dimension is selected to solve the heat transfer problem because it is the dimension where almost all heat conduction occurs. It is assumed that the temperature of the central point of the any node is the average temperature of this node. This assumption is accurate since connectors are made of good conductor materials such as copper and aluminium and because a sufficiently small spatial step Δx is selected.

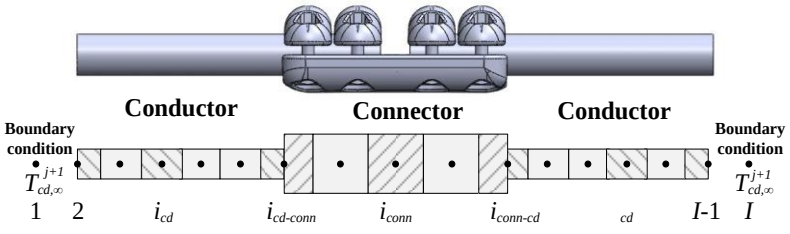

Figure 2.6: Conductor-connector discretization.

In the analysed problem, Joule heating is by far the most important heat source. To accurately reproduce the coupled electro-thermal physics of the problem, conductive, convective and radiative effects will be considered during both the heating and cooling phases. Electrical and thermal equations are solved similarly to how it is done by 3D-FEM software packages.

To increase accuracy and reduce drastically the computational burden, the one-dimensional model retains key information of the three-dimensional geometry from the CAD of the test object to determine the temperature distribution along the conductor and the connector. By this way different parameters related to the three-dimensional origin of each discrete node of the one-dimensional geometry are calculated. They include the outer perimeter and area, or the convective coefficient of each element.

The FDM approach calculates the temperature in each node based on the temperatures of the two adjacent right-side and left-side nodes. Since three nodal temperatures are involved at each calculation step, it results a three-term nodal temperature equation. The tri-diagonal matrix, defining the system of equations arising from the simultaneous solution of all nodes in the analysed domain, can be solved by applying the tri-diagonal matrix algorithm (TDMA) [55]. The FDM formulation approximates the partial derivatives by means of the Taylor expansions in the discretized points of the analysed system. The nodal temperatures are calculated from the temperature of the neighbouring right-side and left-side nodes. The tri-diagonal equations system arising from this approach can be written as [56],

$$a_i^j \cdot T_{i-1}^{j+1} + b_i^j \cdot T_i^{j+1} + c_i^j \cdot T_{i+1}^{j+1} - d_i^j = 0 \qquad 2.10$$

where *i* and *j* are the indices of the spatial and temporal steps, respectively, with *i* = 1, 2, …, *I* and *j* = 1, 2, …, *J*. Therefore, $T_i^j = T(i \cdot \Delta x, j \cdot \Delta t)$ is the mean temperature of the *i*-th node calculated at the *j*-th time-step, being a_i^j, b_i^j, c_i^j and d_i^j constant coefficients. It is noted that Δx and Δt are, respectively, the discretized spatial and time steps considered in the simulations.

By assuming that coefficients a_i^j, b_i^j, c_i^j and d_i^j in (2.10) are known, the vector $[T_1^{j+1}, T_2^{j+1}, ..., T_I^{j+1}]$ of unknown nodal temperatures is obtained from the TDMA algorithm.

The coefficients a_i^j, b_i^j, c_i^j and d_i^j are calculated by applying the rate of energy balance equation in all nodes of the analysed domain (2.11) [57]. For clarity, Figure 2.7 depicts the heat balance.

$$q_{change} = (q_{conduction\_left} + q_{generation}) - (q_{convection} + q_{radiation} + q_{conduction\_right}) \qquad 2.11$$

being q_{change} [W] the rate of energy change in the studied node or element, $q_{conduction\_left}$ the rate of energy flowing into the left side wall of the node, $q_{generation}$ the rate of energy generated in the node and $q_{conduction\_right}$ the rate of energy flowing away from the right wall of the node under analysis.

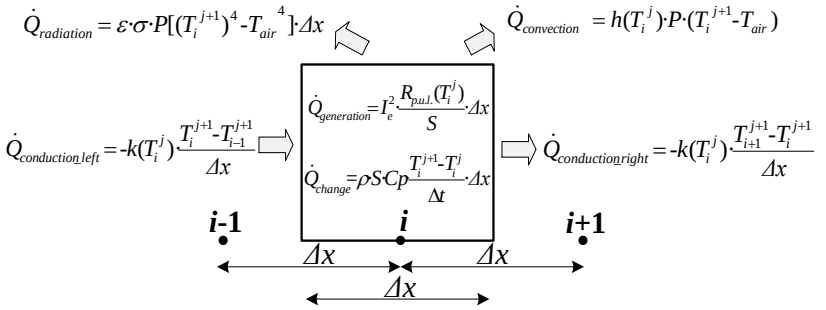

S: cross-section perpendicular to the conduction heat flux
P: outer perimeter of the element
P·Δx: convection and radiation area of the considered element

Figure 2.7: Rate of energy balance in a general element of the studied domain.

It is noted that parameters *S*, *h* and *P* are calculated in each element along the domain since they depend on the three-dimensional geometry of the problem.

The generation term requires knowledge of the electrical resistance of each nodal element. The resistance of the conductor is obtained from the manufacturer datasheet, which is usually provided at 20 ºC in Ω/km. Due to its complex geometry, the resistance of the connector is calculated from its CAD model. The connector geometry is divided in several parts or slices of the same thickness, as seen in Figure 2.8, their parallel faces being perpendicular to the electrical current flow. The envelope of each part and the inner cross section within this envelope is determined by means of a convex-hull algorithm, from which the resistance of the connector is calculated as the addition of the incremental resistances of all slices.

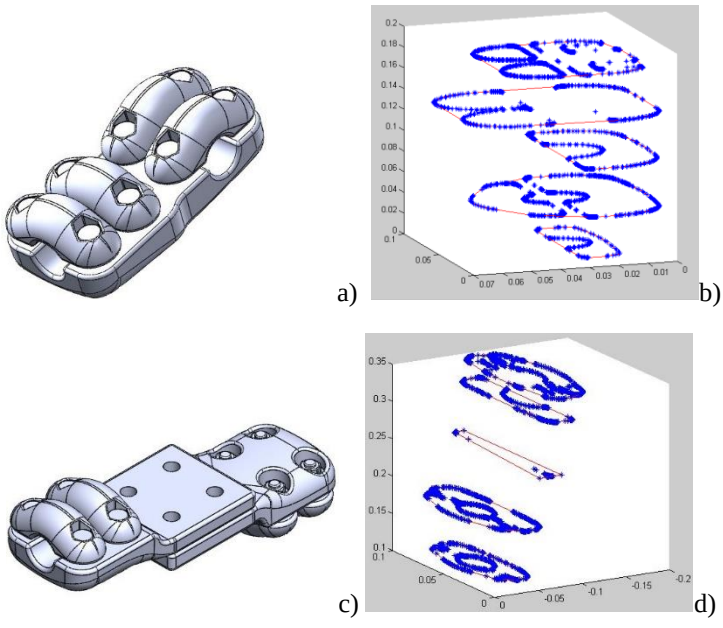

Figure 2.8: Conductor a) CAD of the analysed the T-type S285ZTLS connector. b) Convex-hull envelopes of the T-type S285ZTLS connector after dividing the domain in different slices. c) CAD of two S285ZA4P23LS terminal connectors as usually joined. d) Convex-hull envelopes of the S285ZA4P23LS terminal connectors after dividing the domain in different slices.

To set the initial conditions, it is assumed that the tested objects are at the temperature of the surrounding air $T_{air,\infty}$,

$$T_i^{j=1} = T_{air,\infty} \qquad i = 1,...,I \tag{2.12}$$

Regarding the boundary conditions, the convective and radiative cooling effects have been considered in all nodes of the analysed domain, respectively, as,

$$\dot{Q}_{convection} = h(T_i^j) \cdot P \cdot (T_i^{j+1} - T_{air}) \cdot \Delta x \tag{2.13}$$

$$\dot{Q}_{radiation} = \varepsilon \cdot \sigma \cdot P[(T_i^{j+1})^4 - (T_{air}^{j+1})^4] \cdot \Delta x \tag{2.14}$$

The h coefficient of both the conductors and the connector is computed from the dimensionless Nusselt number Nu, the thermal conductivity k [W/(m·K)] of atmospheric air and the characteristic length L_c [m],

$$h(T_i^j) = k \cdot Nu / L_c \tag{2.15}$$

The characteristic length of the conductor is its diameter and the characteristic length of the connector is the cubic root its volume [58].

The convective coefficient $h_{conductor}$ of the conductor was calculated from the Nusselt number from Churchill & Chu for horizontal cylinders with natural convection [59]. The convective coefficient of the connector $h_{connector}$ was calculated from the Nusselt number of Qureshi and Ahmad [60], [61] for natural convection in horizontal cylinders. To this end, the 3D geometry of the connector is considered since the weighted average value $h_{connector}$ was calculated by considering the angular orientation of each of the individual triangular faces of the surface mesh of the connector, which is directly generated by the CAD software. Since the Nusselt number depends on the temperature, it was re-evaluated at each time-step.

2.1.6.3 Experimental validation of the methodology

Experimental temperature rise tests according to the ANSI/NEMA CC1-2009 standard [3] were conducted in the AMBER laboratory of the Universitat Politècnica de Catalunya to validate the simulation method proposed in this work. The test loop was composed of HTLS GTACSR-464 conductors with outer diameter D_{cd} = 27.5 mm and two S28ZTLS T-type connectors and four S285ZA4P23LS terminal connectors from SBI-Connectors catalogue, as shown in Figure 2.9.

ANSI/NEMA CC1-2009 [3] is the main international standard used by the substation connectors industry. This standard specifies the type of normalized tests to be applied in substation connectors, which include the temperature rise test, which evaluates the performance of the connector at 100%, 125% and 150% of the nominal current of the conductor at which the connector is joined. To pass the test, the temperature of the connector must always be below that of the conductor at any current level. The simulation model proposed in this section is intended to shorten the development time of new lines of connectors and also to avoid the testing of non-compliant prototypes.

Experimental tests were performed at atmospheric conditions (14.5 ºC, 982.7 hPa and 52.3% relative humidity) under a constant current I = 1206 A_{RMS}. The experimental setup includes a 120 kVA bi-phase variable autotransformer [0V-400V] connected to a 120 kVA 400/10 V transformer whose rated output values are 0-10 V, 0-10 kA. The output of this transformer was connected to the test loop. The loop current was measured with a calibrated Fluke i6000s-Flex Rogowski coil that has an uncertainty of 2%. Temperature measurements were performed with 16 K-type thermocouples with a stainless steel sheath (AISI 316, 1 mm diameter) placed on the surface of the conductors' and connectors' bodies. The tolerance of these thermocouples is typically 2.2ºC within the 0-275ºC temperature interval once the temperature reading is stabilized. A small hole was drilled in the connector body to place the thermocouple, which was attached with thermal grease. Thermocouples signals were acquired every 10 seconds by means of a Tecnocat acquisition card.

Annex 1 summarizes the values of the physical properties considered in the simulations.

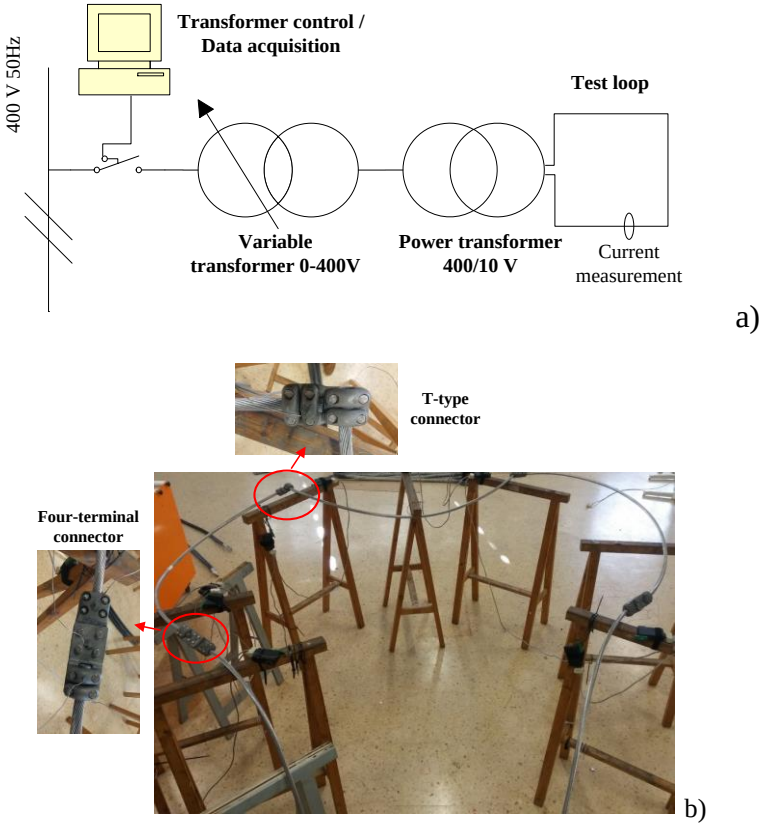

Figure 2.9: Experimental setup. a) Schematics of the experimental setup. b) Test loop composed of an ACSS conductor, S285ZTLS T-connectors and S285ZA4P23LS terminal connectors.

Table 2.1 shows the time- and spatial-steps considered in the simulations performed as well as the duration of the simulations. A time step of 50 s and a spatial step of 0.1 mm were selected after carrying out a study of their values to fulfil both speed and accuracy criteria.

Table 2.1: Calculation parameters of the simulation

Variable	Value
Time step (Δt)	50 s
Simulation time	9000 s
Spatial step ($\Delta x_{cd} = \Delta x_{conn}$)	0.1 mm

Figures 2.10 compare the temperature evolution between the S285TLS T-type connector and the conductor. Figure 2.10a clearly shows that the temperature of the connector is always below than that of the reference conductor, as required by the ANSI/NEMA CC1-2009 standard. Figure 2.10b displays the temperature profile along the whole geometry. It shows that the connector tends to cool the conductor portion closest to the connector, this effect is negligible at about 2 m far from the connector. Figure 2.10c depicts the evolution between experimental and simulated data. The average relative temperature difference is 2.33% for the connector and 1.09% for the conductor.

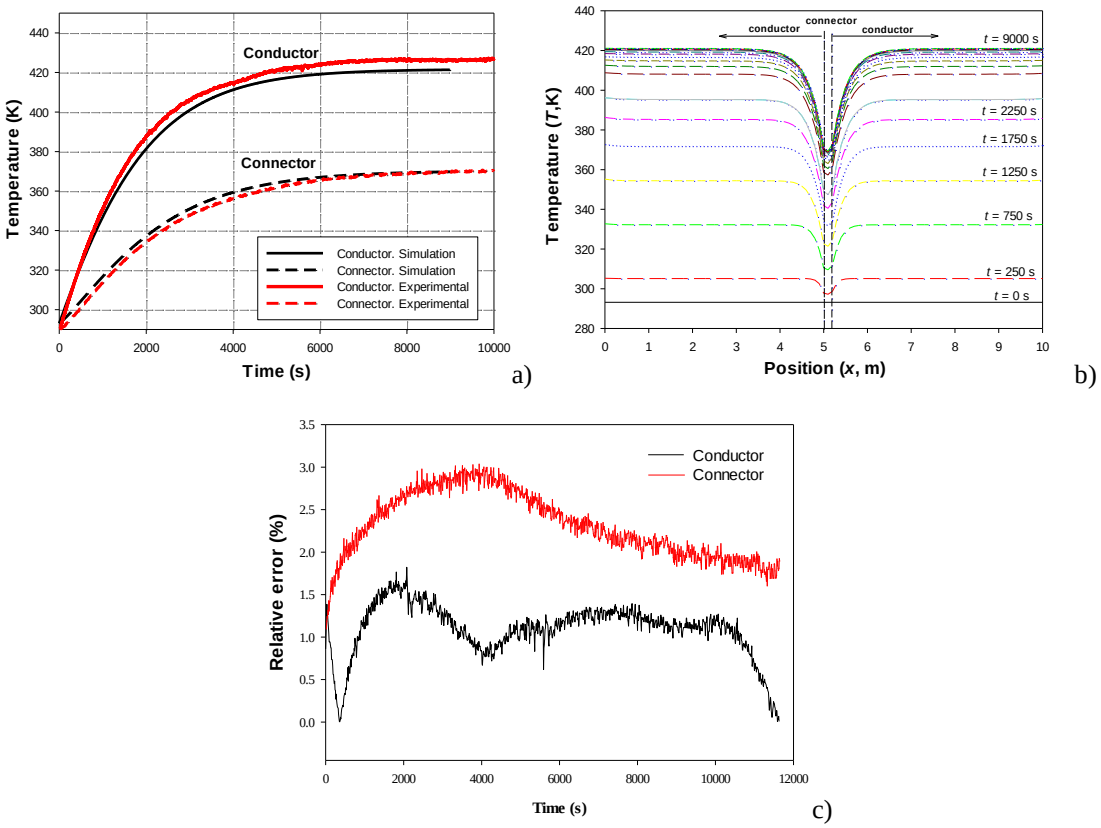

Figure 2.10: a) Experimental data and FDM-based simulation results of the temperature rise for both the conductor ($T_{cd,\infty}$) and the T-type S285TLS connector (centre point). b) Simulated temperature profile evolution with time. c) Temperature difference evolution between experimental and simulated data for the S285TLS connector and its reference conductor.

Figures 2.11 compare the temperature evolution in the terminal connector and the conductor. Again, Figure 2.11a shows that the connector is always cooler than the reference conductor. Figure 2.11b displays the temporal evolution of the temperature profile along the whole geometry. Finally, 2.11c shows an average relative temperature difference of 0.42% for the connector and 1.15% for the conductor.

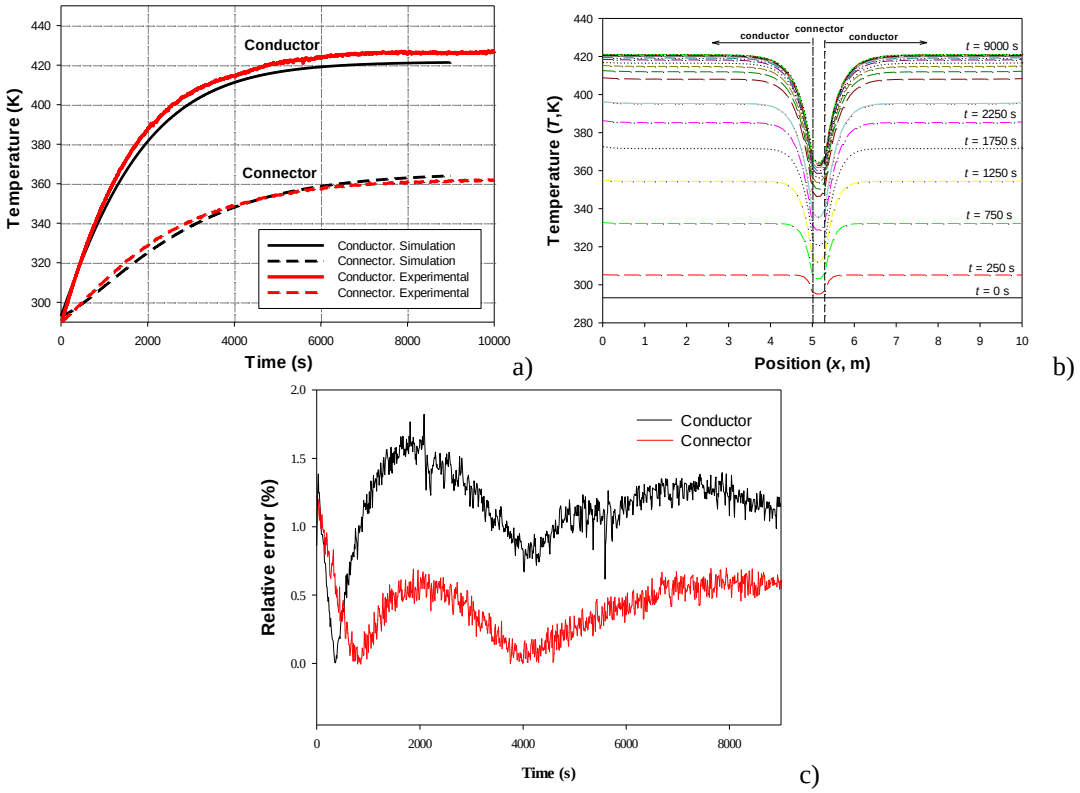

Figure 2.11: a) Experimental data and FDM-based simulation results of the temperature rise for both the conductor ($T_{cd,\infty}$) and the S285ZA4P23LS terminal connector (centre point). b) Simulated temperature profile evolution with time. c) Temperature difference evolution between experimental and simulated data for the S285A4P23LS connector and its reference conductor.

Figures 2.10a and 2.11a show the close agreement between experimental data and simulation temperature profiles for the conductor and the two types of analysed connectors. It is worth noting that the elapsed time required to run a complete simulation is about 40 s using an Intel-Core® i7-3770 CPU 3.4 GHz with 6 GB RAM using a code programmed in the Matlab® R2014a environment. It is much shorter than the average time required by an experienced designer to prepare the 3D-geometry, the 3D-mesh, to define the equations and boundary conditions and to run an equivalent transient 3D-FEM electromagnetic-thermal simulation.

2.1.7 Non-dimensional equations

2.1.7.1 Non-dimensional numbers

The problem of generating reduced-scale tests can be analysed under the scope of the dimensional analysis. When dealing with complex thermal and fluid-dynamic phenomena it is beneficial to use a dimensionless approach. There are two main reasons that apply this scope. The first one is that since tests are performed for specific conditions, so to generalize results, it is advantageous avoiding to present data in terms of dimensional variables such as temperature, velocity, current, etc. The second reason to use dimensional analysis is to use similarity criteria in order to determine the real conditions of the problem under study [62].

2.1.7.2 Basics of dimensional analysis

In many physical processes, heat transfer occurs by the interactions and couplings of the physics involved. The strength of these interactions and couplings is determined by the magnitudes of physical quantities involved that characterize the physical properties of the medium, its state, motion and interactions with the surrounding boundaries [62].

All physical properties are measured by means of a unity scale. Therefore, the unities that measure physical properties are internationally agreed since they are useful to deal with such data. Some of the most used systems of measure are the CGS (centimetre, gram, second), the MKS (metre, kilogram, second) or the FPS (foot, pound, second). When analysing deeply to the information provided by these systems of measure, it is observed that they basically express the same.

Hence, the measure systems are derived unities of the primary unities: mass [M], time [T], length [L], electric charge [Q], temperature [Θ]. For instance, "Force" is measured in the SI in N – in MKS [$kg \cdot m \cdot s^{-2}$] – its primary units are [$M \cdot L \cdot T^{-2}$].

Whenever a problem is analysed experimentally, and the results are used as a pattern to guess the behaviour of a similar configuration of the studied problem, it is strictly necessary to non-dimension the set of equations that govern the similar processes in order to obtain a law that relates the data obtained experimentally with the results required for the desired configuration.

2.1.7.3 Similarity

Similarity is a property shared by two or more physical systems that relates the behaviour of one with the behaviour of the others. Regarding to the subject of study, further than a scale dimensioning of the system, two systems are similar if they share the same non-dimensional numbers that govern the equations describing the phenomena that occurs in both systems.

There are several ways to tackle this problem; despite of that the most systematic one is the Buckingham Pi theorem [63].

2.1.7.4 Buckingham Pi theorem

The Buckingham Pi theorem is a methodology to obtain the non-dimensional groups that characterize a physical problem. Mathematically, suppose that there is a physical equation that relates a set of *X* variables ($Var_1, Var_2, ..., Var_x$) involved in a certain physical problem. Each of the variables can be expressed by *K* physical units like time, length, mass, current, within many others. There must exist a functional relationship like (2.16).

$$f(Var_1, Var_2, Var_3, ..., Var_X) = 0 \text{ or equivalently } Var_1 = f(Var_2, Var_3, ..., Var_X) \quad 2.16$$

The theorem states that the same equation can be rewritten by means of a set of $N = M - K$ dimensionless parameters as seen in (2.17).

$$F(\Pi_1, \Pi_2, \Pi_3, ..., \Pi_X) = 0 \text{ or equivalently } \Pi_1 = F(\Pi_2, \Pi_3, ..., \Pi_X) \quad 2.17$$

where $\Pi_{1,2,...,N}$ are dimensionless terms called Pi groups, with the general form,

$$\Pi_i = Q_1^a Q_2^b ... Q_X^m \quad 2.18$$

where $a+b+...+m=0$ to make Π_i dimensionless. In order to obtain the expression of all the Π_i groups, a system of *K* equations with $K + 1$ unknowns must be written in terms of one of the exponents [64].

The methodology for obtaining the Π_i groups can be easily understood by means of the following example. Suppose that the behaviour of a car running at v_{FS} = 10 m/s along a road of d_{FS} = 1000 m is intended to be studied at a reduced scale. The scale *n* at which the problem is reduced is *n* = 100, thus, the longitude of the reduced-scale road is d_{RS} = 10 m. Such a trivial problem could be stated in the following way. Consider that the problem considers three dimensions: distance *d*[m], time *t*[s], and velocity *v*[m/s]. A law of the form of (2.19) is pursued.

$$v = velocity(d, t) \quad 2.19$$

Two dimensions are involved in the problem, the distance dimension *D* and the time dimension *T*. So, the number of dimensionless quantities is *N* = 3-2 =1. A matrix *M* is then built. The columns of *M* are the original dimensions of the problem, whereas the rows are the units involved in the problem. Thus, for instance, in the third column of *M* seen in (2.20), the exponents of the units of *v* [m/s=m^1s^{-1}] are inputted.

$$M = \begin{matrix} d & t & v \\ \end{matrix} \begin{bmatrix} 1 & 0 & 1 \\ 0 & 1 & -1 \end{bmatrix} \begin{matrix} D[m] \\ T[s] \end{matrix} \quad 2.20$$

The only existing dimensionless quantity Π_1 will have a form similar to (2.18) $\Pi_1 = d^a t^b v^c$. To obtain the exponents, equation (2.21) has to be solved. In it, the dimensions matrix *M* is multiplied by the exponents vector $\vec{w} = [a,b,c]$.

$$M \cdot \vec{w} = \begin{bmatrix} 0 \\ 0 \\ 0 \end{bmatrix}, \vec{w} = \begin{bmatrix} -1 \\ 1 \\ 1 \end{bmatrix} \qquad 2.21$$

The vectors that multiplied by a matrix return a matrix of zeros are commonly known as the null-space of the dimensional matrix. Then, Π_1 value takes the form of (2.22).

$$\Pi_1 = d^{-1} t^1 v^1 = \frac{t \cdot v}{d} \qquad 2.22$$

Recalling the concepts of similarity introduced in the previous section and the problem stated at the beginning of this section to reproduce the behaviour of the real scale car, a reduced-scale car, travelling through a reduced distance, by the same scaling relationship n = 100 and during the same time *t* for both scales would reproduce the behaviour of the real-scale one that has a velocity of v = 10 m/s if their non-dimensional groups have the same value, as shown in (2.23).

$$\Pi_{RS} = \frac{t_{RS} \cdot v_{RS}}{d_{RS}}, \Pi_{FS} = \frac{t_{FS} \cdot v_{FS}}{d_{FS}} = \frac{t_{FS} \cdot v_{FS}}{100 \cdot d_{RS}}, \Pi_{RS} = \Pi_{FS}$$

$$\frac{t_{RS} \cdot v_{RS}}{d_{RS}} = \frac{t_{FS} \cdot v_{FS}}{100 \cdot d_{RS}},$$

$$v_{RS} = \frac{v_{FS} \cdot t_{FS}}{100 \cdot t_{RS}} \qquad 2.23$$

Considering $t_{FS} = t_{RS}$,

$$v_{RS} = \frac{v_{FS}}{100}$$

The result obtained in (2.23) is meaningful in terms of showing how without knowing the exact form of the equations that drive the example, it is possible to compute a set of dimensionless parameter that characterize the problem. These are useful in terms of finding the scale relationships necessary to reproduce test at a reduced scale.

In many cases, some of the Π_i terms obtained through this heuristic can lack of physical meaningfulness. Therefore, it is a task of the test designer to decide their relevance or try to obtain others more meaningful altering the order of terms of *M*. So, even when it is said that no specific equations are required to be known when non-dimensioning equations, a thorough knowledge of the physics under study is necessary to define the relevance of the non-dimensional parameters obtained.

2.1.7.5 Hypothesis applied for scaling thermal tests

The following hypothesis are formulated to analyse the scaling factors,

- The final temperature of both, the full and reduced scale test samples, reached during the electro-thermal tests must be the same, since the temperature is the most influencing parameter in such tests.
- The materials of the conductor and connector remain unchanged for the samples studied in both scales.
- The torque applied to the bolting elements of the connectors is scaled to maintain the mechanical pressure applied to the apparent area of contact.

Reduced-scale tests are often based on a dynamic similarity criterion. Dynamic similarity is achieved when the dimensionless groups provide the same numerical results for the different scales. In the problem under analysis, this means same temperatures at same evaluation times. To achieve this goal, it is often required to change the materials of the downscale samples or the surrounding fluid, thus denaturalizing the purpose of the test. However, thermal similarity is less restrictive, since it does not impose the characteristic dimensionless groups to have the same values [65], [66]. The tests performed at both scales are thermally similar when the homologous surfaces reach equal or homologous temperatures at homologous times [67]. To achieve this condition, the heat-flow distribution in the two scales must be similar.

2.2 Reduced scale temperature rise tests

2.2.1 Introduction

The aim of this test is to ensure that the connector under test operates properly at the three current levels which are defined by the rated current of the reference conductor [5]. The connector passes this test when its temperature is below the temperature of the reference conductor at any current level. Downscale temperature rise tests pursue to apply the exact amount of current to reach the same steady-state temperature than that in the full scale test, for both the connector and the reference conductor, although the rise time interval can be different for both scales.

2.2.2 Mathematical approach

The dimensionless groups arising from the heat conduction equation and the boundary conditions to be evaluated to ensure thermal similitude between the solid and the surrounding fluid are summarized in Table 2.2 [32]. Table 2.2 also includes the physical meaning of each of these dimensionless groups.

Table 2.2: Dimensionless relevant groups for a radiation-convection-conduction problem

Dimensionless group	Expression	Meaning
Π_1	$\left(\frac{k_{Al}}{\sigma T_o^{\,3} L}\right)$	Heat conduction through the solid versus radiation cooling.
Π_2	$\left(\frac{k_{Air}}{\sigma T_o^{\,3} L}\right)$	Heat transfer to the air versus radiation cooling.
Po	$\left(\frac{L^2 q_e}{k_{Al} \cdot T_o}\right) = \left(\frac{I^2 R}{k_{Al} \cdot T_o \cdot L}\right)$	Volume heat source versus conduction.
Gr	$\left(\frac{\rho_{air}^{\,2} g\beta \cdot L^3 \cdot T_0}{\mu^2}\right)$.	Natural convection dimensionless number.

Note that the four dimensionless groups shown in Table 2.2 depend on the characteristic length *L* of the problem, which is considered as the cubic root of the integration volume [58], and thus on the scaling factor. Dimensionless groups Π_1 and Π_2 are related to the heat conduction through the solid material and through the air due to radiative cooling. As deducted from their mathematical expressions, any scale reduction, while conserving the surface temperature, leads to a linear growth of the conduction term, since the distance between the solid core of the analysed object and its surface is reduced by the scaling factor, as proved in (2.24).

$$\frac{\Pi_{1,RS}}{\Pi_{1,FS}} = \frac{\Pi_{2RS}}{\Pi_{2,FS}} = \frac{k/(\sigma {T_o}^3 L_{RS})}{k/(\sigma {T_o}^3 L_{FS})} = \frac{L_{FS}}{L_{RS}} = n \qquad 2.24$$

n being the scaling factor defined as the ratio between the dimensions of the full scale (FS) and reduced scale (RS) test objects.

The dimensionless Grashof number, *Gr*, is related to the natural convection phenomenon, since it represents the ratio between buoyancy and viscous forces in the fluid surrounding the solid object. When reducing the scale of the problem the *Gr* number is also reduced as in (2.25).

$$\frac{Gr_{,RS}}{Gr_{FS}} = \frac{{\rho_{air}}^2 g\beta \cdot L_{RS}^3 \cdot T_0 / \mu^2}{{\rho_{air}}^2 g\beta \cdot L_{FS}^3 \cdot T_0 / \mu^2} = \frac{L_{RS}^3}{L_{FS}^3} = \frac{1}{n^3} \qquad 2.25$$

Finally, the Pomerantsev number, *Po*, is defined as the ratio between the volumetric heat sources and thermal conduction through the solid. Since the amount of volumetric heat generated decreases with the scale of the problem, the *Po* dimensionless number also decreases as,

$$\frac{Po_{RS}}{Po_{FS}} = \frac{\dfrac{{I_{RS}}^2 R_{RS}}{k_{Al} \cdot T_C \cdot L_{C,RS}}}{\dfrac{{I_{FS}}^2 R_{FS}}{k_{Al} \cdot T_C \cdot L_{C,FS}}} = \frac{\dfrac{{I_{RS}}^2 R_{FS} \cdot n}{L_{C,FS}/n}}{\dfrac{{I_{FS}}^2 R_{FS}}{L_{C,FS}}} = \frac{1}{n} \qquad 2.26$$

Rearranging (2.26), the ratio between I_{RS} and I_{FS} can be expressed as,

$$\frac{I_{RS}}{I_{FS}} = \frac{1}{n^{3/2}} \qquad 2.27$$

Equation (2.27) expresses the relationship between I_{RS} and I_{FS} in order to achieve the same steady-state temperature, although the duration of the temperature rise test for both scales is different. Note that (2.27) takes into account convective and radiative effects, without any change in the materials of the scaled test objects.

2.2.3 Experimental validation

2.2.3.1 Experimental setup

The experimental setup to perform temperature rise tests consists of a bi-phase 120 kVA, 0-400 V, variable autotransformer connected to a 120 kVA step-down 400/10 V power transformer unit with output current range 0-10 kA. This equipment is placed at the AMBER laboratory of the Universitat Politècnica de Catalunya (Spain). The test loop including the analysed substation connectors was connected to the output of this transformer, as shown in Figure 2.12. The test current was acquired by means of a calibrated Fluke i6000s-Flex Rogowski coil. Temperature was measured by means of fast T-type thermocouples with Teflon PFA cover placed on the external surfaces of the conductors and the body of the connectors. Thermocouples were inserted in the body of the connectors by means of a small drilled hole with the help of thermal grease. Temperatures were registered every 10 seconds using an acquisition card. Temperature rise tests were conducted indoors at atmospheric conditions (12 ºC, 985.6 hPa and 56 % relative humidity).

Figure 2.12: Temperature rise tests. Test loop composed of HTLS conductors and S285ZTLS T-type mechanical substation connectors.

2.2.3.2 Results

This section compares the temperature evolution during the temperature rise test for both scales obtained through FEM simulations and by means of experimental results.

Due to the use of HTLS conductors, which operate at temperatures much higher than those of the traditional conductors, temperature rise tests were conducted at 100%, 110% and 120% of the rated current of the FS reference HTLS conductor, which are summarized in Table 2.3. Once the values of the three current steps have been settled for the FS tests, the current steps of the RS test are calculated from (2.27).

Table 2.3: Temperature rise tests. Scaling factor n =1.745

Variable	Applied current	Step 1 100% I_n	Step 2 110% I_n	Step 3 120% I_n
Applied current (FS)	I_{FS}	1200 A	1320 A	1440 A
Applied current (RS)	$I_{RS} = I_{FS}/n^{3/2}$ (4)	520 A	573 A	625 A

It is noted that the conductors dealt with to fit with the FS and RS connectors have been tested at 1200 A_{RMS} (GTACSR 464 CONDOR), the rated current, and at the 110% (1320 A_{RMS}) and 120% (1440 A_{RMS}) of this current. The three current steps applied to the RS tests have been scaled by applying (4), the ratio between the RS and FS current derived in this work.

Figure 2.13 shows the temperature evolution of the temperature rise test for the FS and RS analysed loops.

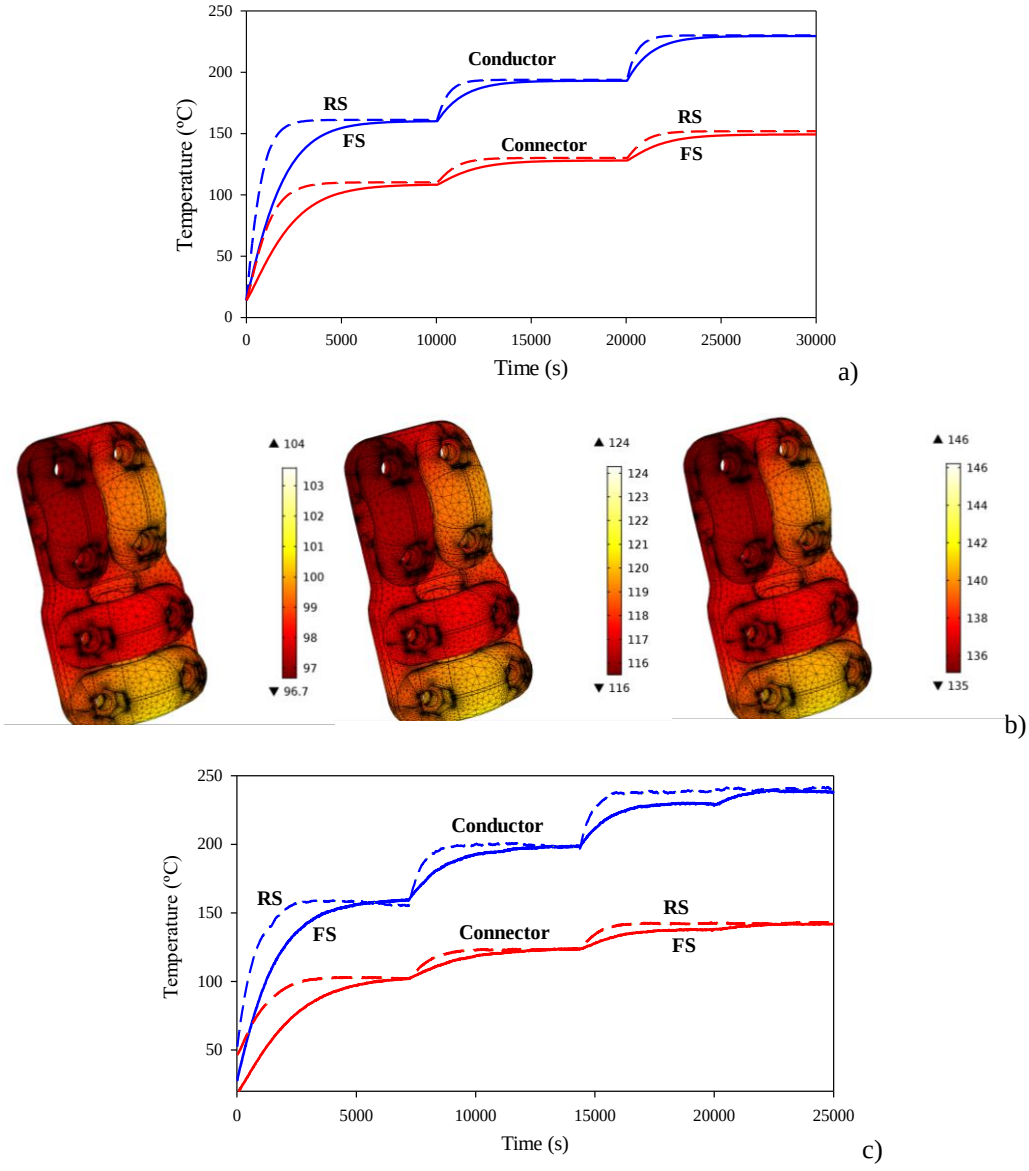

Figure 2.13: Full scale and reduced scale temperature rise tests. a) FEM results. b) Thermal maps of the FS connector surface (ºC). c) Experimental results.

Results in Figure 2.13 show that the solutions provided by FEM simulations are in close agreement with experimental results. It is also noted that by applying (2.27), the temperature rise of the RS samples is the same as in the FS samples for the three current steps thus validating the applicability and accuracy of (2.27).

2.3 Reduced scale short-circuit tests

2.3.1 Introduction

The aim of this test is to ensure that the connector under test operates properly after a short-circuit stress[5]. The connector passes this test when its temperature is below the temperature of the reference conductor at any current level. Downscale short-circuit tests pursue to apply the exact amount of current to reach the same peak temperature than that in the full scale test, for both the connector and the reference conductor in the same time. As the heating process is adiabatic, the heating time for both scales is the same.

2.3.2 Mathematical approach

Since the short-circuit test is a very fast phenomenon, it is assumed adiabatic heating [68], [69]. This means that the effects of conduction, radiation and convection are neglected from (2.28), the heat balance equation.

$$m \cdot c_p \cdot \Delta T = I^2 R \cdot t \qquad 2.28$$

By assuming the same temperature rise, duration and materials for both scales, (2.28) results in,

$$\frac{m_{FS} \cdot c_p \cdot \Delta T}{m_{RS} \cdot c_p \cdot \Delta T} = \frac{\rho \cdot c_p \cdot Vol_{FS} \cdot \Delta T}{\rho \cdot c_p \cdot Vol_{RS} \cdot \Delta T} = \frac{R_{FS} \cdot I_{FS}^2 \cdot t}{R_{RS} \cdot I_{RS}^2 \cdot t} \qquad 2.29$$

From (2.29) it results,

$$\frac{Vol_{FS}}{Vol_{RS}} = \frac{R_{FS} \cdot I_{FS}^2}{R_{RS} \cdot I_{RS}^2} \qquad 2.30$$

Since $Vol_{FS} = n^3 \cdot Vol_{RS}$, n being the scaling factor, the relationship between the resistances for both scales becomes,

$$R_{RS} = \rho_e \cdot \frac{L_{RS}}{A_{RS}} = \rho_e \cdot \frac{L_{FS} / n}{A_{FS} / n^2} = R_{FS} \cdot n \qquad 2.31$$

and thus, (2.31) can be rewritten as,

$$\frac{n^3 \cdot Vol_{RS}}{Vol_{RS}} = \frac{R_{FS} \cdot I_{FS}^2}{n \cdot R_{FS} \cdot I_{RS}^2} \qquad 2.32$$

Finally, the relationship between the reduced scale and full scale currents factor for the short-circuit currents to achieve the same temperature raise with the same short-circuit duration under the adiabatic assumption can be expressed as,

$$\frac{I_{RS}}{I_{FS}} = \frac{1}{n^2} \qquad 2.33$$

It is noted that (2.27) and (2.33) are different because they have different purpose. Whereas (2.27) calculates the current ratio for the temperature rise test (considering conductive, convective and radiative phenomena) to achieve the same steady-state temperature with different duration for both scales, (2.33) applies the adiabatic approximation during the short-circuit transient, which pursues obtaining the same temperature by assuming the same short-circuit duration for both scales.

2.3.3 Experimental validation

2.3.3.1 Experimental setup

Experimental short-circuit tests were conducted at the facilities of Veiki VNL laboratory (Budapest, Hungary). The experimental setup to conduct such tests is able to provide up to 170 kA_{peak} and up to 1000 MVA. It consists of a protective circuit breaker, a synchronized making switch, a reactor set, two three-phase regulating transformer units and two short-circuit transformers. The output voltage and current were acquired by means of a 1kV/100V calibrated voltage divider and a calibrated Rogowski coil. Temperature was measured by means of calibrated K-type thermocouples inserted in small holes drilled in the bodies of the connectors and in the conductors. The thermocouples signals, which were registered every 100 μs, were acquired by means of a digital acquisition card through an analogue converter. Short-circuit tests were conducted outdoors at atmospheric conditions. Figure 2.14 shows the loop analysed for the short-circuit tests.

Figure 2.14: Short-circuit tests. Test loop composed of HTLS conductors and S285TLS T-type connectors.

2.3.3.2 Results

Short-time withstand current and peak withstand tests are conducted to ensure the resilience of electrical equipment to the unpredictable and hazardous effects of short-circuit faults. Short-circuits are usually fast transient phenomena, since the electrical protections have typical actuation time less than one second. Substation connectors are tested to withstand a short-time current of several tens of kilo-amps, typically during 1 s [28]. These results provide valuable data to be used during the optimal design process of such devices. The standard short-circuit test often contains two parts, the rated peak withstand current test and the rated short-time withstand current test [70]. The connector passes the test when its temperature is less than that of the reference conductor.

Table 2.4 summarizes the currents applied during the peak withstand current and short-time withstand current tests.

Table 2.4: Test currents used during the short-time withstand current tests

Scale	Applied current	Peak withstand current (kA_{peak})	Short-time withstand current (kA_{RMS})
Full scale (FS)	I_{FS}	128.20	52.62
Reduced scale (RS)	$I_{RS} = I_{FS}/n^2$ (10)	42.03	17.10

It is noted that from the experimental values of the FS peak withstand and short-time withstand currents, the ones related to the RS test are obtained by applying (2.34), which has been applied supposing adiabatic conditions.

Figures 2.15 show the 0.3 s transient stage of the experimental and simulated peak withstand current test as well as the short-time withstand current test with a duration of 1 s. Figure 2.15a and 2.15b show, respectively, the results of FEM simulations and the experimental ones of the temperature rise and the cooling stages during the peak withstand current tests for both scales.

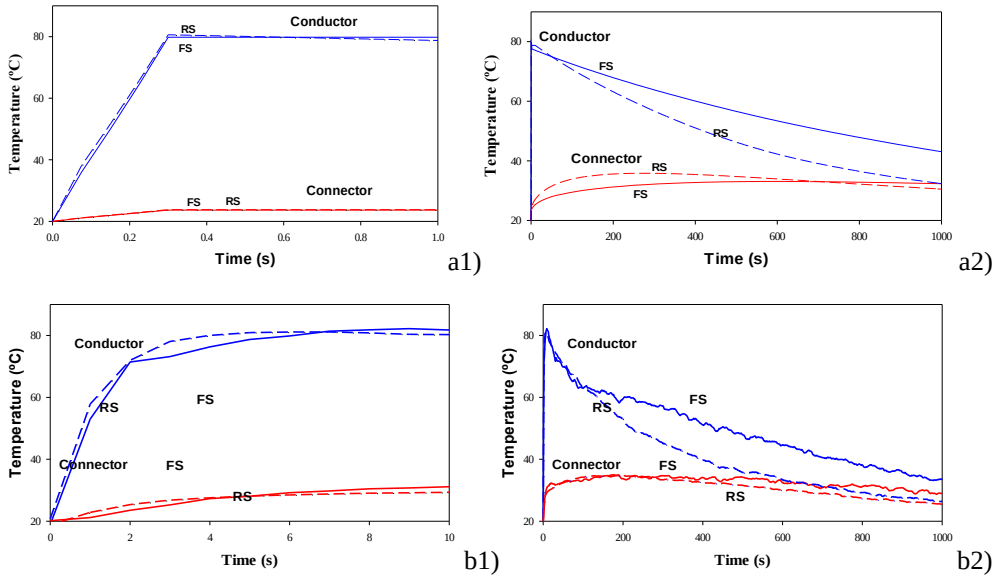

Figure 2.15: Full scale and reduced scale peak withstand current test. a) FEM results. b) Experimental results.

Results presented in Figure 2.15 clearly show that the connectors and conductors of both scales reach the same temperature just after the peak withstand current test, although, as expected, the RS tested components cool down faster during the cooling stage.

Figure 2.16a and 2.16b show, respectively, FEM and experimental results of the temperature rise and the subsequent cooling phase during the short-time withstand current tests for both, the FS and RS samples analysed.

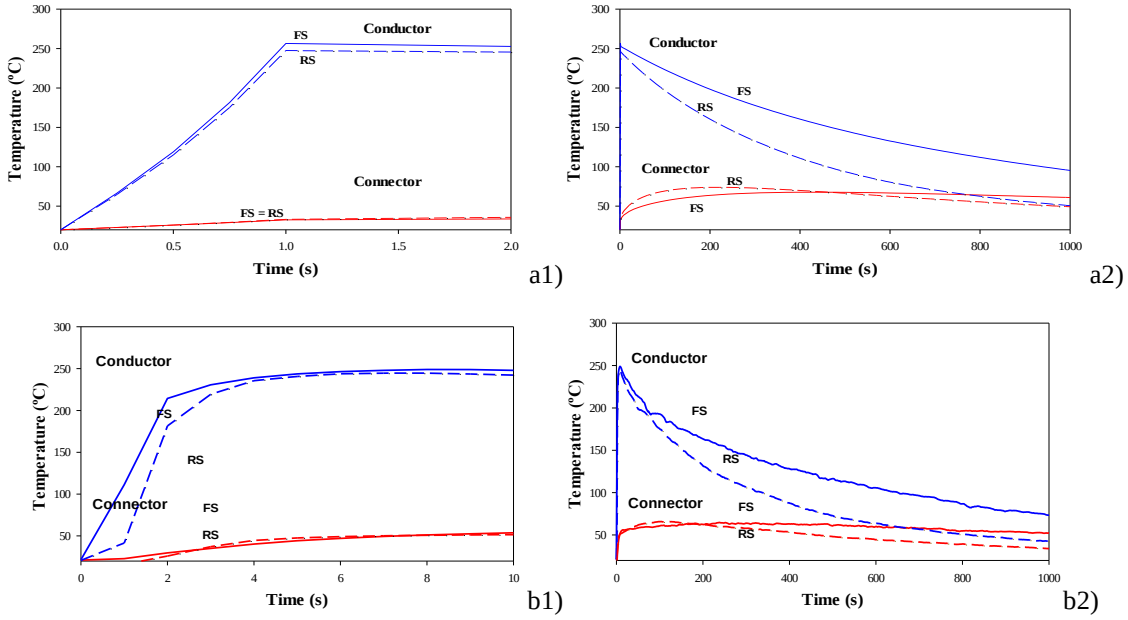

Figure 2.16: Short-time withstand current test. Comparison between FS and RS tests. a) FEM results. b) Experimental results.

Results presented in Figure 2.16 show, once again, that just after the end of the short-circuit transient, the temperature reached for the FS components is the same that of the RS components. These results validate the approach described previously. Once the short-circuit current has been cleared, the cooling process for both scales has different time-constant due to the different mass of the two scales, as well as inherent differences in the convective phenomena due to the different sizes of the metallic faces in contact with the surrounding air.

Results summarized in Figures 2.15 and 2.16 validate the applicability and accuracy of (2.33).

2.4 Conclusions

The present chapter has reviewed the issue of joule heating in substation connectors, and in extension to any energized accessory installed in power transmission lines. Commonly, in order to test the suitability of newly developed products designed to work under a specified thermal stress, standard tests are performed. These, nowadays are not designed for substation connectors aimed to work attached to HTLS conductors. These conductors work at a range of temperatures that ranges between 150ºC to 250ºC, well above the range of 70ºC to 90ºC of nowadays installed conductors. Therefore, in these applications, the reduced-scale temperature rise test and the reduced-scale short-circuit test methodologies have been presented, based on the use of reduced-scale connector samples in order to obtain insight about the standard test results. The aim is to allow manufacturers to obtain data of the performance of new designs of substation connectors during the optimization stage of such products without having to outsource such tests to more powerful external laboratories.

For each of the tests herein analysed, an expression that relates the current that has to be applied with respect to the scale relationship between tests has been obtained. Although the temperature rise test and the short-circuit share the same physical heating phenomenon, the scale relationships obtained for each of the tests are different. This happens because the assumptions by which the scale relationships where obtained differ. For the temperature rise it is considered joule heating, with conduction, convection and radiation. During short-circuits, due to the fast temperature rise of the tested assembly, the heating process is considered adiabatic.

Finally, 3D-FEM simulations and experimental tests demonstrate that the developed scale relationships are useful to reproduce full-scale tests in reduced-scale samples. Thus it has been proved that these expressions are able to guide the extrapolation of results obtained in reduced-scale tests to assess the development of full-scale products.

3 CORONA TESTS

3.1 Introduction

This chapter develops two methodologies aimed at simplifying corona tests for product optimization purposes, whilst reducing the cost and requirements of facilities and instrumentation needed. First, a thorough revision of the theoretical background of the corona phenomenon is presented. A description of the experimental methodologies employed through this chapter is detailed as well. Next, a FEM-based visual corona experimental methodology is presented to reduce the voltage requirements of such tests. Finally, a FEM-based approach to perform corona tests for reduced-scale models and to extrapolate the data obtained in such tests to real-scale models is presented.

3.2 State of the art

3.2.1 Corona discharge

Corona is a sort of partial discharge, luminous and localized, seen in high-voltage electrodes surrounded by a gas dielectric that produces a localized ionization once the electric field on these electrodes surpasses a critical onset value [13], [71]. Although coronas generate a conductive area surrounding an electrode, they do not induce electrical breakdown if voltage levels are no further increased [11]. Corona depends mostly but not solely on weather conditions, geometry and applied voltage. Another way to understand the process is to consider corona discharges as a release of capacitive energy stored in the electric field [72].

Corona exists both in positive and negative polarity. Both polarities share many similar characteristics but the physical processes involved differ [73]. A corona discharge is commonly divided in two regions. The first, a thin ionizing layer surrounding the outmost points of the electrode surface. The second, a drift region where the circulation of ions towards the collecting electrode takes place. The first ionizing layer is usually stated as the unique source of unipolar ions. These generate a space charge density and follow the field lines [74]. Microscopically, the physical processes that lead to the ionization of the insulating gas surrounding the electrode are collision, drift of ionic particles, photoionization, attachment and recombination [75]. The ionization of such quantity of gas can finally turn it into plasma. This is when coronas are seen as a violet glow halo around energized electrodes.

Under AC electrode excitation, as voltage is risen, negative polarity corona takes place first. Negative corona is characteristic for the emission of soft blue light at the electrode surface. It is rarely heard (sometimes only a slight hiss is detected), and generates very little RIV (radio interference voltage). It is, as well, not straightforward to be seen even using light amplification instrumentation [10].

On the opposite, positive corona inception is abrupt, sonorous and easily seen under darkness conditions. It generates significant RIV emissions, and usually masks negative corona due to its much vigorous effect.

Differences between corona phenomena relay in the significant mass difference between electrons and positively charged ions. It is studied that at very short spacing (below 5 mm), the breakdown characteristics for both polarities almost match, and no corona region is seen. At larger space-gaps (20 mm and above) positive corona occurs at lower voltages than negative coronas [76].

Being the corona inception in air-insulated systems condition highly dependent on the air properties, electric field strength, and electrodes geometry, the equations governing the inception of corona are used to calculate the electric field distribution around the analysed electrodes.

The Poisson equation (3.1) that describes the distribution of the electric scalar potential V,

$$\varepsilon_p \nabla^2 V = \rho_c \qquad 3.1$$

Assuming that the gas surrounding the charged electrode is at uniform ambient conditions and therefore, ignoring diffusion, expression (3.2) can be derived from the previous [77].

$$\nabla \rho_c \cdot \nabla V = \frac{\rho_c^{\,2}}{\varepsilon_p} \qquad 3.2$$

Equation (3.2) is solved by means of FEM (3D-FEM) simulations performed with the Eletrostatics module of Comsol Multiphysics® software [78]. Since there are not any effective sensors for measuring the electric field, such simulations are applied to determine the surface electric field in the areas of the connectors generating corona. Further in this chapter it is explained in deep the use of the values of electric field obtained by means of FEM simulations.

3.2.1.1 Positive corona

Positive coronas occur in the vicinities of an excited electrode under positive DC polarization or during the positive half-cycle of the voltage sinusoid for AC excitation. They are commonly seen as a violet-white glow surrounding the electrode (as seen in Figure 3.1). As their emissions are mostly in the ultraviolet, only a part of the radiation spectrum falls within the visible [79].

A positive corona appears by an exogenous ionization event in a region of high-voltage gradient. Free electrons liberated because of the ionization process are attracted towards the electrode. The accumulation of negative charge due to free electrons, repulse positive ions from the electrode. By a set of inelastic collisions close to the electrode, molecules are ionized in an accelerated reaction forming an electron avalanche.

Figure 3.1: Inception of positive corona and streamer.

In a positive corona, secondary electrons, the ones that trigger the subsequent avalanches after the first, are originated predominantly in the fluid outside the plasma region. This area is usually named as avalanche region. Secondary electrons are liberated by the ionization process instigated by the photons emitted from the corona plasma during the set of various de-excitation processes occurring within the plasma after electron collisions. The electrons appearing from the ionization of neutral gas molecules are then electrically attracted back toward the electrode. This lets to a self-sustained reaction that creates further avalanches of electrons inside the plasma zone [80].

3.2.1.2 Negative corona

Negative corona process of self-sustained discharge is rather more complicated than the positive one. As with positive ones, the first corona event starts with an exogenous ionization event, a primary electron that triggers an electron avalanche (see Figure 3.2).

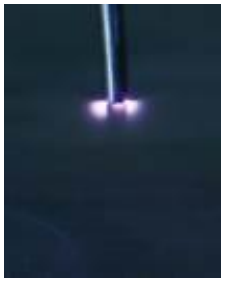

Figure 3.2: Inception of negative corona and streamer.

As opposite to positive coronas, the electrons ionized from the neutral gas, commonly air, are useless in terms of sustaining the negative corona process. Instead, the preponderant process generating secondary electrons is the photoelectric effect from the electrode surface. The electron-liberation is enhanced by the collisions of highly energized photons from atoms within the plasma body that relax after excitation from previous collisions. The importance of ionized neutral gas as an ionization source is low and diminishes with time as positive ions tend to cluster around the curved electrode. Simultaneously, secondary electrons travel outwards the electrode, thus colliding with neutral molecules. In air, oxygen and water vapour are also electronegative molecules, and therefore they combine and become negative ions [79].

3.2.2 Effects of corona discharges

Effects of corona discharges are numerous, being generally harmful in high-voltage electric switchgear. Amongst the most important are ozone generation, audible noise, electromagnetic interference and power loss [11]–[13]. Current pulses due to corona are very fast, in the order of some nanoseconds, thus being an important source of wide spectral-range electromagnetic interference, covering a frequency range from the ultraviolet and visible to radio and TV spectral regions (UHF) [81]. Corona is a well-known source of voltage transients. Such discharges degrade insulation systems since their effects are permanent and cumulative [82]. Thus, they are a cause of reliability drop of electrical devices.

3.2.3 Peek's law

Peek's law defines the electric field strength required to trigger the corona discharge phenomenon for an isolated conductor, two parallel conductors or a coaxial cylinder [83]–[89]. The origin of the expression is purely empiric and its formula is shown in Equation (3.3).

$$E_c = E_o \cdot m \cdot \delta \left(1 + a / \sqrt{\delta \cdot r}\right) \text{ [kV/cm]} \qquad 3.3$$

E_o (kV_{peak}/cm) being the disruptive visual voltage gradient measured at standard atmospheric conditions, δ the relative air density, r the curvature radius of the conductor, m a rugosity factor and a around 0.301-0.308 $cm^{1/2}$ depending on the specific conductor configuration.

Peek's law will be generalized along this chapter to predict corona inception values for random three-dimensional surfaces. To do so, Peek's law will be reduced to its parametric form (3.2). Later, these parameters will be properly analysed by means of a hybrid experimental-simulation approach.

$$E_c = b \cdot \left(1 + c / \sqrt{r}\right) \text{ [kV/cm]} \qquad 3.4$$

Note that b (kV_{peak}/cm) and c ($cm^{1/2}$) are parameters, whose values depend on the specific geometry of the problem.

3.3 Corona discharge measurement

Corona discharges can be visually detected or electronically measured. Visual detection is almost imperceptible in daylight because most of its spectrum is in the ultraviolet range. Consequently, its detection requires the use of digital cameras with a light-spectrum wider than the human one. These tests are useful to identify the weakest areas, the most electrically stressed, of high-voltage accessories. A proper location of over-stressed points is of notable usefulness during the optimal design stage of new high-voltage components [90].

Although visual corona detection methods are useful, they are still not extended and for many applications they are simply unfeasible. Thus, in order to properly asses the corona onset conditions of high-voltage devices international standards propose also the use of PD (partial discharge) or RIV (radio interference voltage) detection systems [12], [13], [72].

Some examples of the standards are the NEMA 107-2016 (RIV) [91], the IEC 60270:2000 (PD) [92], the IEEE Std. 1829-2017 (visual corona and RIV) [93] or the ANSI/NEMA CC1-2009 (visual corona and RIV) [3], the latter one being specific of substation connectors. From the non-visual corona discharge measurement methods, the RIV in μV correlates the ear acoustical noise impression with the appearance of corona effect. On the other hand, PD measurement, as measured by the IEC 60270:2000 [92], is based on an indirectly assessment of the charge and frequency of coronas, which are a form of PD, by measuring the apparent charge displacement in pC detected in calibrated elements of a circuit, such as coupling capacitors. Apparent charge can be understood as the charge that if suddenly injected between the terminals of the test object would alter transitorily the voltage between the terminals by the same amount as the partial discharge [71].

3.3.1 Visual corona measurement methodology

The two methodologies described in the following sections base their experimentation methodology in the recording of visual corona inception. These tests have been carried out in the AMBER high-voltage laboratory of the Universitat Politècnica de Catalunya using a calibrated 130 kV BK-130 high-voltage generator from Phenix technologies. Figure 3.3 shows the layout used to carry out this test.

Visual corona was recorded by means of a Canon EOS-70D digital camera. It includes a 20.2 Mpixels CMOS APS-C sensor (22.5 mm x 15 mm). Corona onset points were located with the high-voltage laboratory completely darkened and performing long exposure photographs.

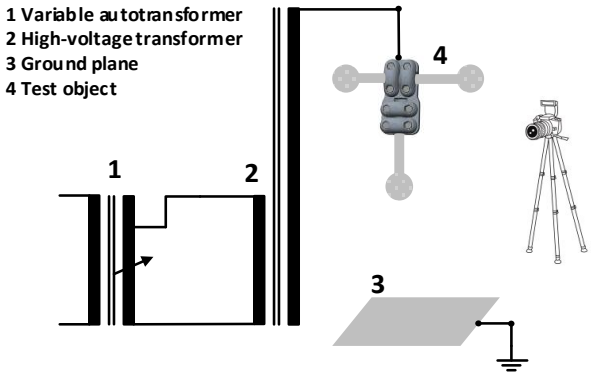

Figure 3.3: High-voltage generator used for the experimental tests.

Corrections of the values of experimental visual corona must be performed, as these are dependent on the local atmospheric conditions [72]. To do so, the measured voltages are transformed to the standard atmosphere conditions (101.3 kPa, 20 ºC, and absolute humidity 11 g/m^3) by applying the method proposed in in the IEEE Std 4-2013 standard [94].

All visual corona voltage values in this chapter correspond to corona extinction voltage (CEV). CEV is the highest voltage at which corona no longer occurs when voltage is gradually decreased from the corona inception value [71]. Corona inception voltage (CIV) is defined as the lowest voltage at which continuous corona happens when voltage is risen gradually.

Under alternating current excitation (50 Hz) negative corona appears first than positive corona for air-gaps larger than 20 mm. Nevertheless, corona recordings were taken during positive corona according to IEEE Std 1829-2017 [95] standard. CEV was determined following the procedure recommended in the IEEE Std 1829-2017:

1. Increase the voltage gradually and slowly until positive corona is observed on the surface of the connector under test. This is the corona inception voltage (CIV).
2. Following, increase the voltage by 10% and uphold it for 60 seconds.
3. Finally, lower slowly the voltage until observing the extinction of positive corona. This is the positive corona extinction voltage (CEV).

Steps 1 to 3 are repeated 3 times for each connector and the average value of CEV is calculated. Photographic reports of these tests are provided along this chapter.

3.3.2 Calibration of the digital camera system against PD measurement

As introduced in previous sections, a digital camera substitutes PD or RIV corona detection methods in the proposed test methodologies. Herein the battery of tests performed to check the sensitivity of a commercial digital camera, with respect to a commercial PD measurement system, is described. PD system is used as a reference, since apart from the US, it is more widespread that the RIV system. It is also known that PD measurements provide higher sensitivity [96], [97] because the measurement system takes into account a wider bandwidth and a lower measuring frequency. Thus, the obtained PD signal is stronger. The principal differences between PD and RIV measurement methodologies are found in the calibration procedure, the measurement instruments and the measuring bandwidths and frequencies [97].

The geometries considered as a reference to determine the inception voltage in air are the rod-plane and the needle-plane electrode configurations [98]. Figure 3.4a shows the needle-plane configuration used to generate corona discharges. These discharges have been measured by means of a PD detector and a digital camera, in order to compare the sensitivity of both methods under the testing conditions described previously.

The tests here described were carried out in a small-size laboratory of the Universitat Politècnica de Catalunya (4 m x 6.75 m, and height 3 m). A 130 kV BK-130 high-voltage generator manufactured by Phenix technologies was used to generate the test voltage. Figure 3.4b shows the layout used to carry out this test.

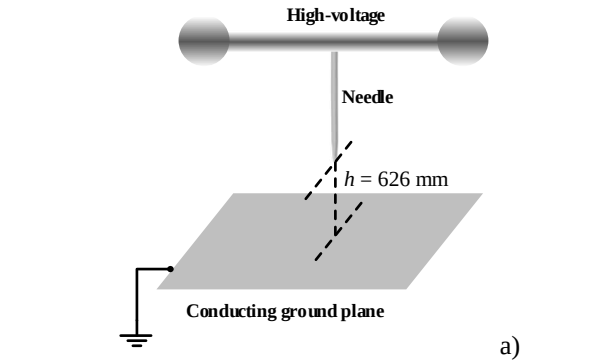

a)

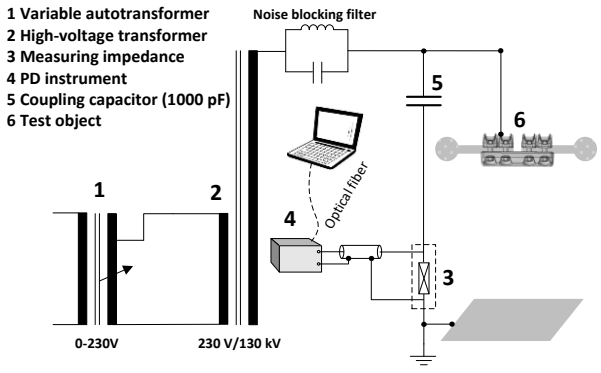

b)

Figure 3.4: a) Needle-plane experimental setup to calibrate the digital camera against PD measurements. The rod of the needle has a diameter of 3 mm, whereas the diameter of the tip is 1.5 mm. The distance between the tip of the needle and the ground plane is 626 mm. b) PD measuring circuit in accordance with the IEC60270 standard.

A Canon EOS-70D digital camera was used to detect the visual corona, which is equipped with a CMOS APS-C sensor (22.5 x 15 mm) with 20.2 Mpixels resolution and variable sensitivity in the range 100-12800 ISO. To magnify the test object an 18-135 mm objective was used. The camera was operated in the bulb mode, which allows setting both the aperture and shutter speed.

PD pulses were acquired by means of a commercial Techimp PD-BaseII instrument, using the standard IEC60270 bandwidth (115-440 kHz) and a sampling frequency of 200 Msamples/s. The PD detector allows expressing the measured voltage as equivalent charge in pC. A PDCAL PD calibrator was used to calibrate the test object to reduce the effect of the background noise.

PD tests were carried out at local atmospheric conditions (17.1 ºC, 49.2 %RH and 987.1 hPa). Under the conditions above, the detection limit of the digital camera was 9.8 kV_{RMS} as shown in Figure 3.5a. The detection limit of the PD detector was 10 kV_{RMS} with the IEC60270 bandwidth as Figure 3.5b depicts. Although, some corona activity was detected buy masked by the background noise at 9.7 kV_{RMS}.

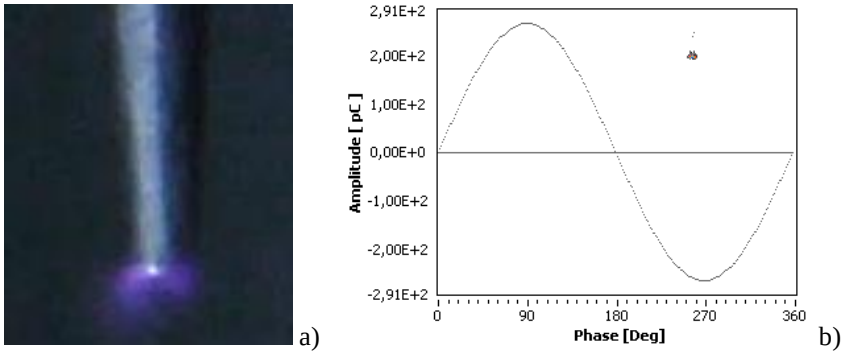

Figure 3.5: Detection limit of the needle-plane setup. a) Alternating current negative corona photograph taken with the digital camera. b) Partial discharge pattern corresponding to negative corona acquired during 39.55 s (310 pulses) with the PD detector

PD results from Fig. 3.5b clearly show a corona pattern, since they are concentrated in the negative semi-period of the voltage waveform, with an average phase angle of 258º.

These results prove that the sensitivity of the digital camera is comparable to that of the PD detector under unscreened laboratory conditions. Hence, the detection of corona activity can be performed with a digital camera. This method allows to properly identify the exact location of the discharge points for routine visual corona tests intended for product optimization in industrial laboratory facilities. The cost of the installation of a simple laboratory as the used in this experience is drastically lower than that of a screened laboratory and a PD detector. Finally, it is worth noting that high-voltage accessory manufacturers usually let a wide electric field safety margin. Therefore, a slight sensitivity difference between the digital camera and the PD detector is not relevant at product optimization level.

3.4 Reduced voltage corona tests

3.4.1 Introduction

Visual corona tests are one of the most convenient methods to locate the critical corona points of high-voltage components such as substation connectors. The proper location of these points allows applying corrections of the design of such devices.

Other common methods to detect corona activity in electrical stressed devices are PD (partial discharges) and RIV (radio interference voltage). These techniques do not provide information about the exact location of the corona discharge, although their technical requirements are high. To be performed with sufficient accuracy, such tests require expensive screened laboratories and sophisticated instrumentation.

For all of this, corona tests are commonly performed in external laboratories. This leads for manufacturers to expensive test costs, long waiting times and no intervention in the collection of data. Finally, customers have to pay for a service, where despite of a certificate of corona validity, manufacturers are unable to obtain relevant data for the optimization of the product.

This section presents a feasible solution to execute routine corona tests for product optimization in high-voltage manufacturer facilities. To do so, laboratory size and screening requirements, applied voltage, assembly and testing times are greatly reduced, thus dropping the overall costs of the tests related to new product developments. The methodology herein presented uses a commercial digital camera in order to detect the corona onset. Thus, it uses of an affordable detection device without lack of sensitivity, which is also useful to exactly detect the corona points. As the other methods presented in this thesis, the presented methodology is applicable to many other high-voltage components such as, but not restricted to, corona protections, vibration dumpers, spacers for bundle conductors and conductors themselves.

3.4.2 Theoretical approach

Corona discharges appear in energized accessories and specifically, in connectors, whenever the electric field in any surface point surpasses a threshold value. This value, $E_{inc,}$ the inception electric field, depends on the voltage applied to the connector, the surrounding dielectric medium, the curvature of the surface and the distance to surrounding grounded elements.

The approach proposed to perform simplified corona tests is based on the modification of the clearances between the connector and the surrounding grounded walls. By this manner it is allowed a drastic reduction of technical requirements necessary to perform the tests. Specifically, it allows to minimize the dimensions of the laboratory, maximum voltage applied, nominal power, and instrumentation requirements. In addition, it is worth noting that the following approach does not require the use of a high-voltage generator free of partial discharges.

The following lines summarize the three-step strategy in which the simplified visual corona test is based.

First, (Step 1.1 in Figure 3.6) a FEM simulation of the standard corona test [12], [74] is performed. The simulated geometry is the same as in the standard test, and the distance to the ground-plane must be the final installation height of the connector. The applied voltage must be equal as in the standard corona test, that is, 10% above the nominal operating voltage of the connector [3]. FEM simulation allows locating the points of the surface of the connector with highest electric field strength. It also provides the numerical value of the electric field strength in these points. Following, (Step 1.2 in Figure 3.6), it is carried out a FEM simulation, where the geometry of the connector is maintained, so that the height of the test object above the ground plane is reduced notably. Usually the height used for this test is below 1 m. The critical corona points in the surface of the connector will coincide with the ones obtained in the previous simulations. The value of test voltage necessary to apply during the simplified visual corona test in Step 2 (experimental corona test at reduced height above ground plane) must accomplish that the electric field strength in the corona points located in Step 1.2 is the same than in Step 1.1.

Following, (Step 2 in Figure 3.6) refers to the experimental simplified visual corona test carried out in an indoor small unscreened laboratory. The connector under test is placed at the reduced height determined in the previous step. Critical corona points on the connector surface are detected using a digital camera. The advantages of the test are numerous, and they go beyond the evident drop of the test cost. The most notable are that engineers in charge of product optimization are able to test their design in the manufacturers' facility. Thus, no long waiting times are faced. Also, many other useful product information can be gathered by means of these tests. Therefore, it eases the process of connector optimization. Whenever a design doesn't fulfil the required specifications, Steps 1 and 2 can be repeated iteratively until ensuring that the connector is ready to pass the standard corona test.

Finally, in the third step (Step 3 in Figure 3.3) the mandatory standard corona test is carried out to the final optimized connector in an accredited high-voltage facility.

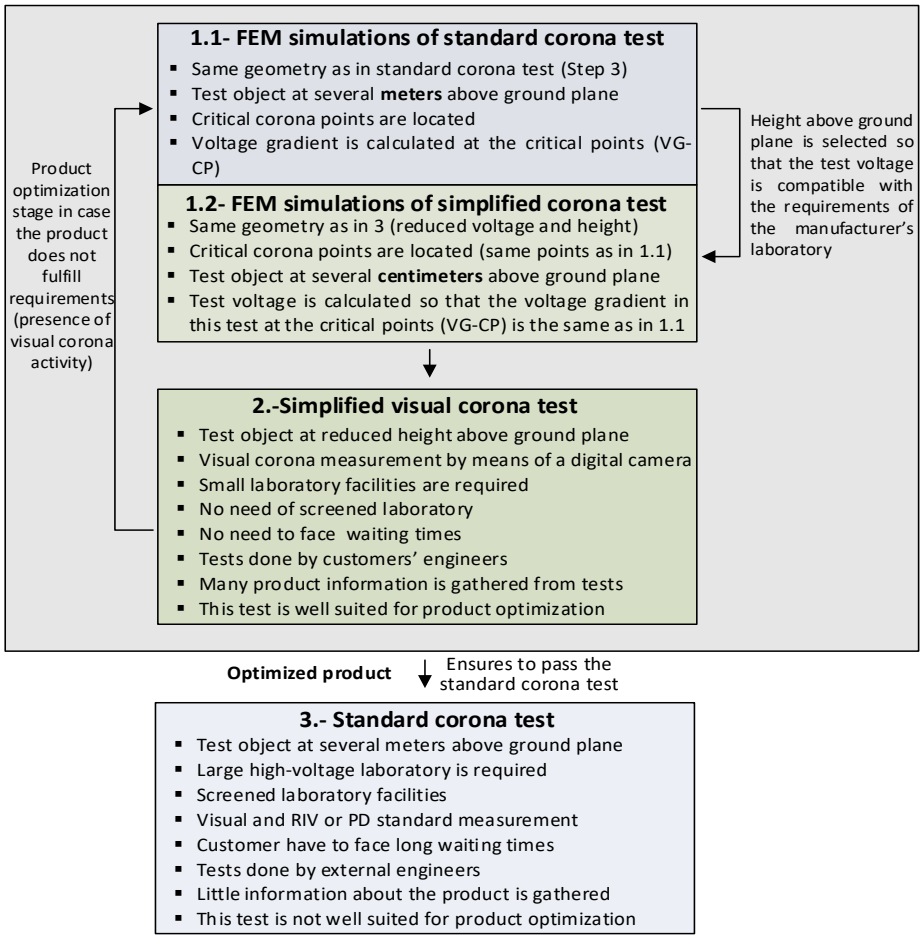

Figure 3.6: Summary of the three-step approach proposed to perform reduced voltage corona tests

3.4.3 Experimental validation

Visual corona tests, which are performed in completely blackened laboratories, use image caption methods to identify the onset of corona effect. The main goal of these tests is to detect the levels of voltage at which the inception (CIV) and extinction (CEV) of corona effect are detected for a determined test object at a particular height above the ground-plane.

The data presented in this section follows the test procedure for visible corona recommended in the IEEE 1829-2017 guide [93] and detailed in *'3.3.1 Visual corona measurement methodology'*. The procedure is repeated a minimum of three times to ensure results repeatability. It is considered that an object passes the test whenever both the visual extinction and inception voltages are greater than the thresholds of CIV and CEV specified. Hence, no visual corona must be detected at the acceptance test voltage [93]. Note that the data hereafter presented is referred always to CEV, since under AC excitation it is lower than the CIV, being a most restrictive condition. Recall also, that as previously explained, all CEV experimental values are corrected to the standard atmospheric conditions (20 ºC, 101.3 kPa, and absolute humidity 11 g/m^3) [94].

Phase spacing and ground-plane distance are standardized according to the ANSI/NEMA CC1-2009 [3]. Table 3.1 summarizes the standard distances required for different nominal voltages. Also, visual corona and audible noise extinction voltage are required to be at least above a 10 % of the rated operating voltage, and the RIV level must be below 200μV. Note that a RIV level of 0V is unpractical since it is physically unfeasible to find any hardware without measurable RIV near its operating voltage [93].

Table 3.1: Phase Spacing and Height Above Ground as a function of the Nominal Operating Voltage According To ANSI/NEMA CC1-2009 [3]

Nominal voltage (kV_{RMS})	Phase spacing (m)	Height above ground plane (m)
230	3.4	4.6
345	4.9	7.6
500	7.6	9.1
765	13.7	13.7
1100	16.8	16.8

3.4.3.1 Connector J40S33PK

This section describes the tests performed to the J40S33PK mechanical substation connector from SBI Connectors catalogue, made of A356 aluminium alloy. The study of the suitability presented in the previous lines, first requires to carry out the standard corona test. To do so, the J40S33PK mechanical substation connector was tested in the facilities of Veiki Laboratory (Budapest, Hungary). Corona inception was detected by means of RIV measurements. The J40S33PK substation connector was installed at 7 m above the ground-plane level. The measured CEV was around 170 kV_{RMS}, with a RIV level of 71 μV, far below the 200 μV limit value suggested by the ANSI/NEMA CC1-2009 . Hence the tests were performed under more restrictive conditions than those imposed by the ANSI/NEMA CC1-2009 standard. RIV measurements were carried out at 0.65 MHz across a 300 Ω impedance, in accordance with the IEC 60437 standard [99]. The test was carried out at local atmospheric conditions, 25.2 ºC, 998 hPa and 53.6% relative humidity. The wiring diagram is analogous to that in Figure 3.4b, but the measuring impedance was replaced by another one, in accordance with the specifications of the ANSI/NEMA CC1-2009, and a RIV meter (Siemens B83600-B40) was used.

Following this first standard experiment, the test was replicated by means of FEM simulations. The same geometry was reproduced, following the procedure detailed in *'3.4.2 Theoretical approach'*. The critical corona points were located on the surface of the connector and the electric field in such points during the corona extinction condition was obtained, as shown in Fig. 3.7.

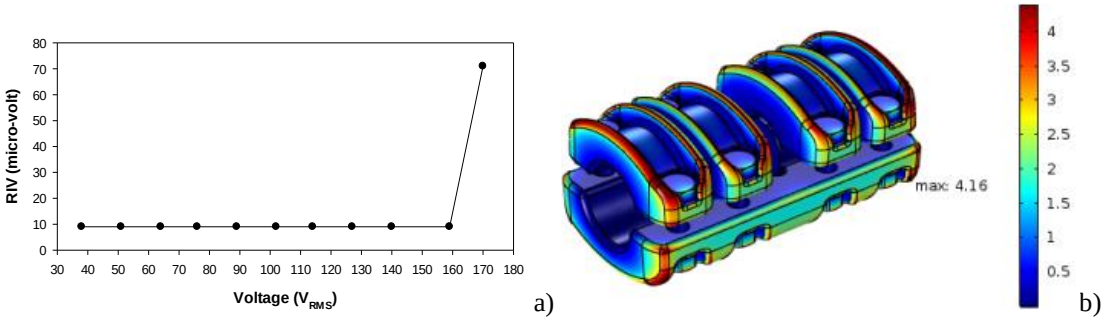

Figure 3.7: Connector J40S33PK. Large-size screened laboratory. The height above ground plane is 7 m. a) RIV measurement to determine the corona inception voltage conducted in Veiki Laboratory. b) FEM simulation. The electric field strength is in kV/mm.

Next, a second FEM simulation was carried out preserving the geometry of the problem but decreasing the height of the J40S33PK connector above the ground plane to 0.315 m. The height was chosen to guarantee corona onset conditions below 130 kV_{RMS}, which is the maximum output voltage of the small-scale high-voltage facility were these tests were carried out. The critical corona points on the connector surface matched the critical points obtained in the standard corona test.

To conclude, the connector was tested in the small-scale high-voltage laboratory of the Universitat Politècnica de Catalunya, with the connector placed at a height of 0.315 m above the ground-plane level. Figure 3.8 depicts the experimental setup, the FEM simulations results and the corona streamers that appeared on the critical points of the connector.

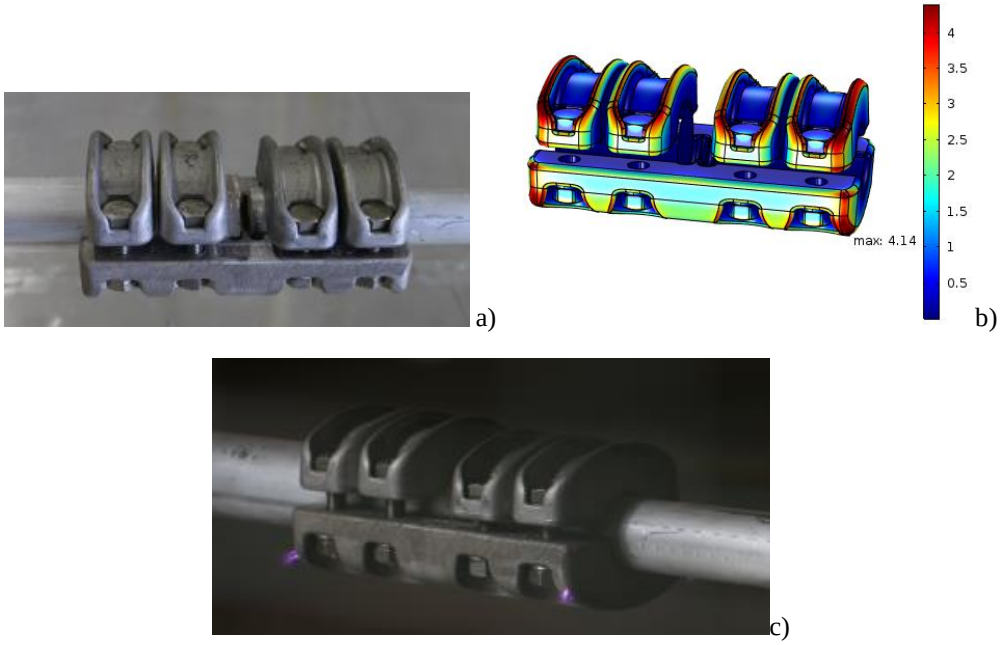

Figure 3.8: Connector J40S33PK. Small-size unscreened laboratory. The height above ground plane is 0.315 m. a) Experimental setup of the simplified visual corona test including the tested substation connector, the conductors and the spherical corona protections. b) FEM simulation of the J40S33PK mechanical substation connector. The electric field strength is in kV/mm. c) Visual corona photographed with the digital camera.

Table 3.2 shows the numerical results acquired in this section. The values of extinction electric field are almost equal for both experiences. The suitability of the test method presented in this section is proved with these results. Assembly and testing times, and facility requirements have been reduced notably by applying this approach.

Table 3.2: Comparative results between large-size and small-size laboratories

Laboratory type	Corona extinction voltage* (kV_{RMS})	Extinction electric field* (kV_{peak} /mm)	Height above ground plane (m)
Large-size	170	4.16	7.0
Small-size	98	4.14	0.315

*Corrected to standard atmospheric conditions according to [94].

3.4.3.2 Connector J40S33D4PK

This section repeats the methodology presented in the previous points to further validate the reduced voltage corona test approach. The J40S33D4PK from SBI connectors, made of A356 aluminium alloy, was tested, as well, in the facilities of Veiki Laboratory (Budapest, Hungary). It was installed at 7 m height over the ground-plane level. No changes in laboratory, measuring devices and experimental conditions were made with respect to the previous section. The measured CEV was approximately 170 kV_{RMS}, and the RIV value was 141 μV. This value is again below the 200 μV limit recommended by the ANSI/NEMA CC1-2009 standard [3].

As previously detailed, the experimental test was replicated by means of a FEM simulation. Critical corona points on the surface of the connector and the electric field in such points during the corona extinction conditions were obtained as shown in Figure 3.9.

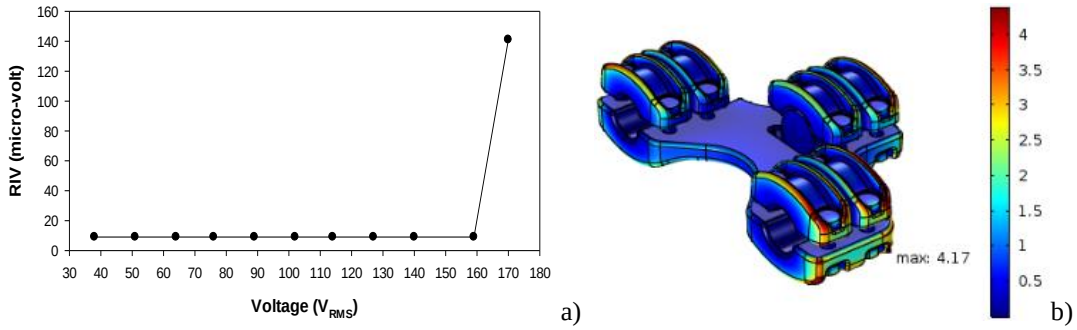

Figure 3.9: Connector J40S33D4PK. Large-size screened laboratory. The height above ground plane is 7 m. a) RIV measurement to determine the corona inception voltage conducted in Veiki Laboratory. b) FEM simulation. The electric field strength is in kV/mm.

Next, a FEM simulation preserving the geometry of the connector, but decreasing considerably the height above the ground plane to 0.455 m was performed. The height was chosen to ensure corona onset conditions below 130 kV_{RMS}, the maximum voltage of the small-size laboratory used for this study. The critical corona points on the connector surface matched the critical points obtained in the standard corona test.

To conclude, the connector was tested in the small-scale high-voltage laboratory of the Universitat Politècnica de Catalunya, with the connector placed at a height of 0.455 m above the ground plane level. Figure 3.10 depicts the experimental setup, the FEM simulations results and the corona streamers that appeared on the critical points of the connector.

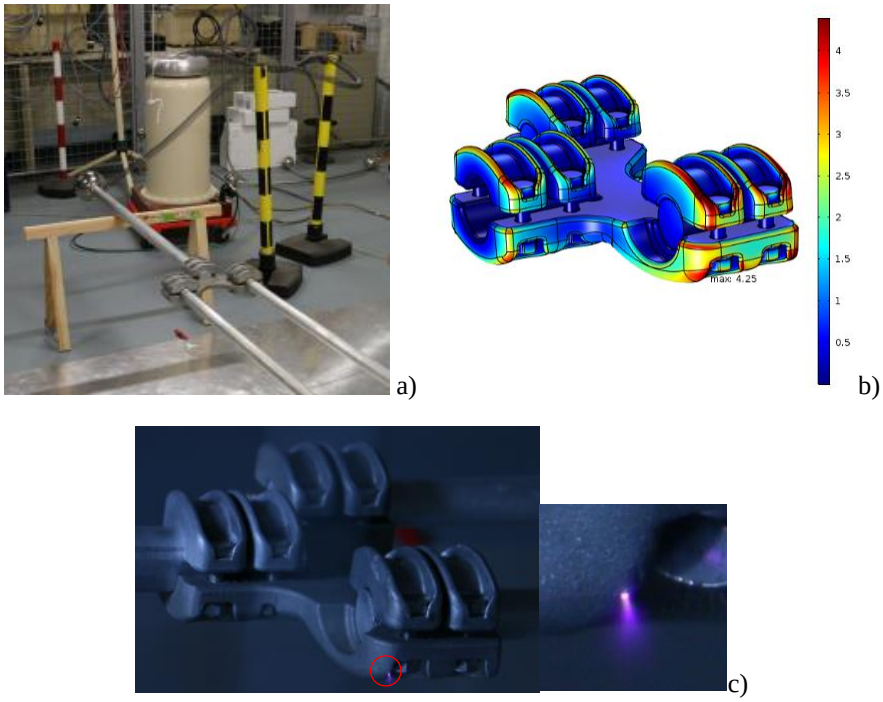

Figure 3.10: Connector J40S33D4PK. Small-size unscreened laboratory. a) Experimental setup of the simplified visual corona test including the tested substation connector, the conductors and the spherical corona protections. The height above ground plane is 0.455 m. b) FEM simulation of the J40S33D4PK mechanical substation connector. The electric field strength is in kV/mm. c) Visual corona photographed with the digital camera.

Table 3.3 summarizes the numerical results obtained in this section. The values of electric field extinction are almost equal for both experiences. The suitability of the test method presented in this section is proved with these results. Assembly, testing times, and facility requirements have been reduced notably.

Table 3.3: Comparative results between large-size and small-size laboratories

Laboratory type	Corona extinction voltage* (kV_{RMS})	Extinction voltage gradient* (kV_{peak} /mm)	Height above ground plane (m)
Large-size	170	4.17	7.0
Small-size	101	4.25	0.455

*Corrected to standard atmospheric conditions according to the [94].

3.4.4 Electric field lines distribution around the connector surface

The suitability of the proposed approach can be observed in Figure 3.11. The results of the FEM simulations are compared when the connector is placed at a height of 0.315 m and 7 m above the ground plane. It illustrates that the electric field far from the surface of the connector is clearly influenced by the height of the test. However, the distribution of the surface electric field is almost equal for both configurations and therefore, the location of the critical corona points on the surface of the connector remains virtually unchanged.

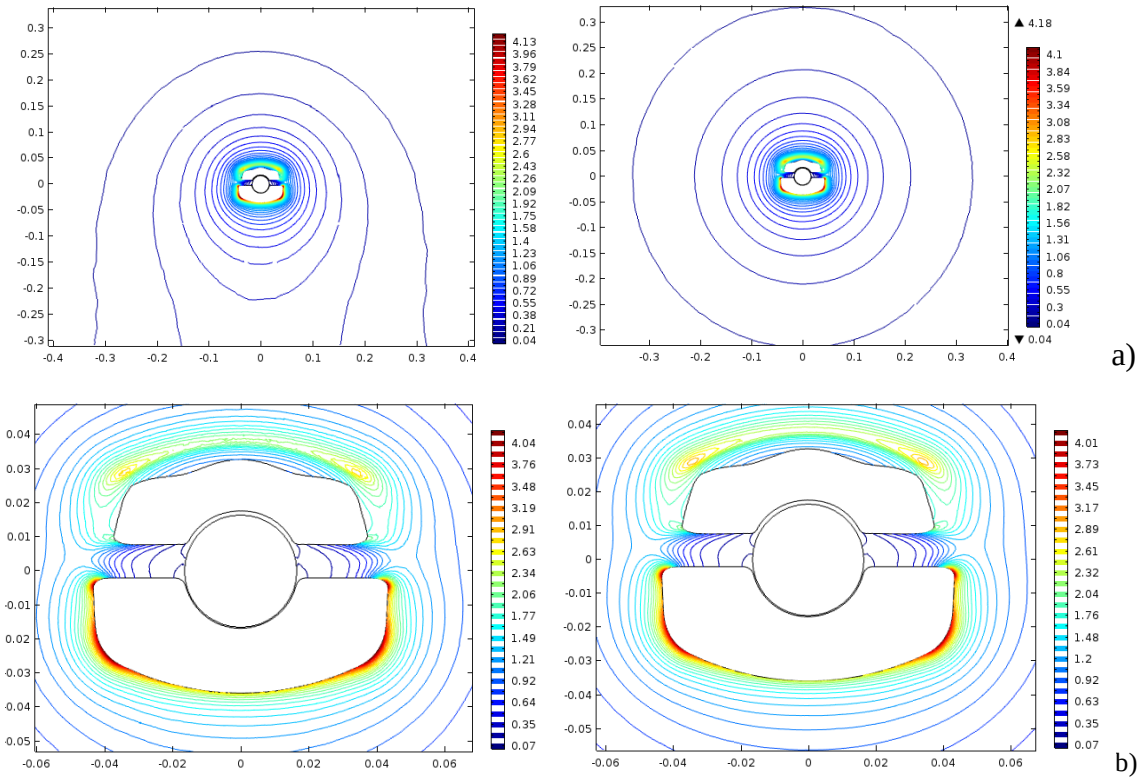

Figure 3.11 a) Electric field (kV_{peak}/mm) distribution around the most stressed parts of the connector for the connector placed at a height of 0.315 m and 7 m above the ground plane, respectively. b) Detail of the electric field distribution on the vicinities of the surface of the connector for both configurations, 0.315 m and 7 m above the ground plane, respectively.

3.5 Reduced-scale corona tests

3.5.1 Introduction

Before going through compulsory standard tests, new connector designs are extensively validated in manufacturers' laboratories, in order to ensure proper performance and reliability. Wide-ranging experimental tests of full-scale (FS) prototypes are the most extended validation method nowadays. Nevertheless, these present a sort of drawbacks such as added complexity [100], extended assembling and test time [65], and consequently high cost [101] [102]. Hence, this section proposes a methodology based on the use of reduced-scale (RS) prototypes to overcome the aforementioned drawbacks. These models are currently considered as viable, valuable and essential design tools [103]. Nevertheless, the relationship between RS and FS prototypes is not always linear. Thus this section tackles the problem of finding the proper relationships between scales [104].

As already introduced in previous sections, standard full-scale corona tests require large screened laboratories with high-voltage capability [105]. These are scarce and so, tests become costly for manufacturers as they have to be outsourced [85]. Outsourcing them is translated to long waiting times. Also, engineers in charge of the design of the connector lack of intervention during the test, thus losing the opportunity of acquiring relevant information and experience regarding the performance of the connector under test.

The use of reduced-scale models lets to speed up and diminish the cost of corona tests, because the required facilities and testing devices are more affordable. The size of the test hall and clearances are dramatically reduced thus easing the work of carrying out routinely corona tests in industrial laboratories.

The electric field in the vicinities of the reduced-scale test object follows the same pattern than that resulting in the full-scale test [106], [107]. Several reports are found in the literature comparing reduced and full-scale tests of electromagnetic behaviour of DC and AC power lines [108]–[110]. In [111] it is proved that great similarity exists when evaluating full- and reduced-scale models, the ion current density, electric field distribution, and corona activity of monopolar dc and single-phase ac lines are equivalent.

Conducting reduced-scale visual corona tests for product optimization in unscreened industrial laboratories with a limited voltage output is appealing since it allows a drastic reduction of the requirements of the high-voltage generator. A resulting size reduction of the testing area is permitted since the test voltage can be reduced and the generator does not require being free of partial discharges. A DSLR (digital single-lens reflex) camera can be used to record corona activity [112], [113], reducing the requirements of the corona measuring instruments.

3D-FEM simulations are used to determine the electric field of the reduced- and full-scale connectors, as done in [107], [114]. The approach also identifies the critical corona points of the surface of the connector, whereas it is affordable in terms of computational time [100], [107]. Hu et al. [114], already used a similar approach to deduce equivalences between reduced- and full-scale bundle conductors models. Nevertheless, there is still a lack of works focused on properly analysing the corona onset on complex three-dimensional shapes such as high-voltage hardware. Hence, the use of downscaled models is appealing, specifically when combined with FEM simulations, because it allows to derive relationships of electrical behaviour, which are later applicable to full-scale models.

Based on the Peek's law, a method to infer the equivalence between visual corona onset for models with different scales is proposed. As done previously, the methodology presented in the following lines is validated by means of a set of different visual corona tests performed to different substation connectors with a scale factor 1:1.745. It is worth noting that the method presented in the following lines can be tailored to be applied to different high-voltage hardware, such as corona protections, conductors or fittings for substations or power lines among many others.

3.5.2 Analysed substation connectors

The study herein carried out has been developed with the following 5 models of A356 aluminium substation connectors, from the catalogue of SBI Connectors, two of which have been manufactured at two scales, that is, FS (full scale, 1:1) and RS (reduced scale, 1:1.745), which are shown in Figure 3.12.


a)


b)


c)


d)


e)

Figure 3.12: The five models of substation connectors analysed in this section. a) T-type connector J285TLS, FS and RS with a scale factor 1:1.745. b) T-type connector S285TLS, FS and RS with a scale factor 1:1.745. c) Coupler connector J40S33PK. d) Double coupler connector J40S33DPK. e) Duplex T-type connector Z12T390D9DLSP.

Table 3.4 shows the main features of the conductors or bus bars at which each analysed substation connector are linked.

Table 3.4: Conductors associated to each connector

Connector designation	Scale	Conductor 1	Conductor 2
J285TLS	FS	GTACSR-464 (ϕ = 27.6 mm)	GTACSR-464 (ϕ = 27.6 mm)
J285TLS	RS	GTACSR-131/19 (ϕ = 15.79 mm)	GTACSR-131/19 (ϕ = 15.79 mm)
S285TLS	FS	GTACSR-464 (ϕ = 27.6 mm)	GTACSR-464 (ϕ = 27.6 mm)
S285TLS	RS	GTACSR-131/19 (ϕ = 15.79 mm)	GTACSR-131/19 (ϕ = 15.79 mm)
J40S33PK	FS	Al bus bar (ϕ = 33 mm)	Al bus bar (ϕ = 40 mm)
J40S33DPK	FS	Al bus bar (ϕ = 33 mm)	Al bus bar (ϕ = 40 mm)
Z12T390D9 DLSP	FS	Al bus bar (ϕ = 120 mm)	Quad bundle Al rod (ϕ = 39 mm)

3.5.3 Connector reduced-scale optimization approach

Figure 3.13 summarizes the approach proposed for performing reduced-scale corona tests with the aim of optimizing high-voltage hardware, specifically substation connectors. Tests can be performed in small and unscreened high-voltage laboratories, usually located in manufacturer facilities. This methodology aims to reduce considerably the power, facility dimensions and requirements, test time, preparation time and instrumentation requirements to obtain insight of the corona behaviour of products. By this manner the process of product optimization can be simplified and speeded up considerably.

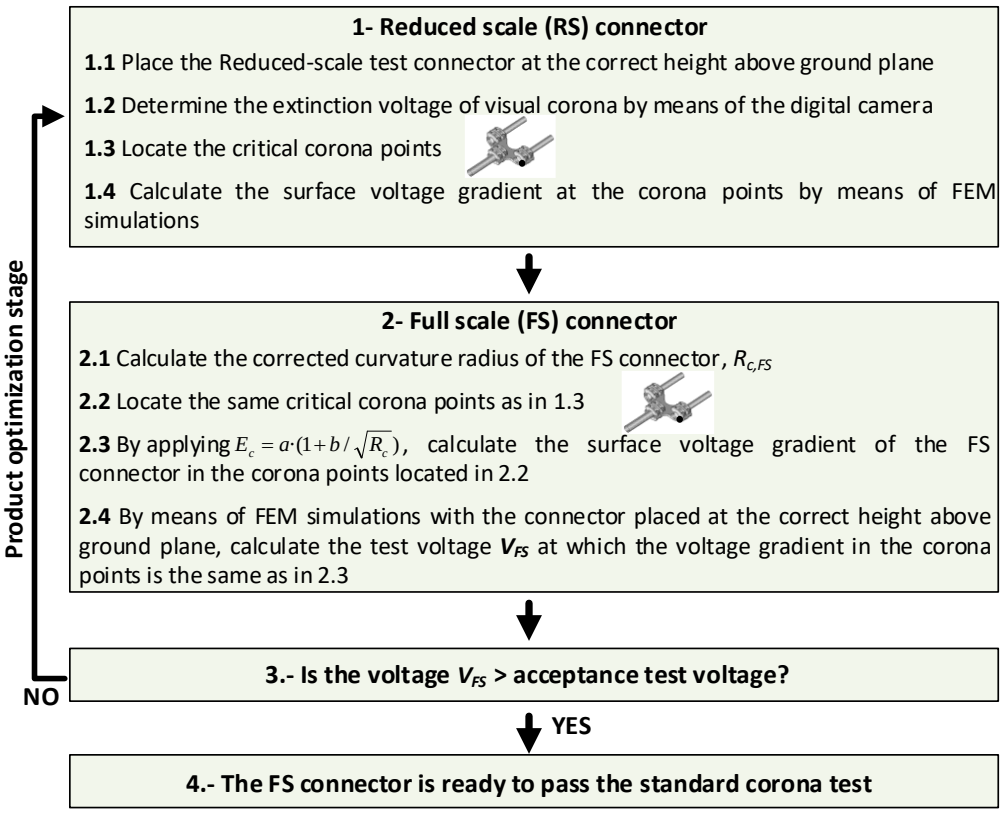

Figure 3.13: Summary of the approach proposed in this work.

The reduced-scale optimization procedure consists of four steps. The first is the experimental analysis and FEM simulation of the RS (reduced scale) connector. Step 1 includes the following stages:

- Step 1.1. The RS connector is assembled in the high-voltage laboratory to conduct the visual corona test.
- Step 1.2. The visual corona test is performed and long exposure photographs are taken to detect corona activity. The visual corona extinction voltage is determined.
- Step 1.3. The corona onset points on the surface of the connector are located.
- Step 1.4. The surface voltage gradient in the corona points located in step 1.3 is calculated by means of FEM simulations when applying the visual corona extinction voltage obtained in step 1.2.

The second step is related to the FEM simulation of the full-scale connector. This consists of the following stages:

- Step 2.1. The corrected curvature radius of the FS connector is calculated by applying (3.6).
- Step 2.2. Locate the corona onset points on the surface of the connector. These points are the equivalent points of the RS connector located in step 1.3.
- Step 2.3. Calculate the surface voltage gradient at the corona points of the FS connector located in step 2.2, by applying (3.7).

- Step 2.4. By simulating through FEM the geometry of the FS connector when placed at the standard height above ground plane, calculate the test voltage V_{FS} to be applied at which the surface voltage gradient on the corona points located in step 2.2 is the same than that calculated in step 2.3.

No visual corona at the acceptance test voltage must be seen [95], so the visual corona test is passed when the visual CEV is greater than the specified one. Lastly, the FS connector passes the standard corona test if the voltage V_{FS} calculated in step 2.4 is higher than the acceptance test voltage. Otherwise, the connector geometry must be modified in order to improve its design. If this happens, the procedure has to be repeated from step 1.1.

The strategy presented in Figure 3.13 is intended to be applied during the optimal design stage of high-voltage hardware, since it guarantees that the final design will pass the mandatory standard corona test.

3.5.4 Experimental and FEM results

Table 3.5 summarizes the results of CEV of the visual corona tests performed to the five connectors presented in *'3.5.2 Analysed substation connectors'*. It also shows the height at which each of the connectors were tested. These results are the starting point for the calculation of the electric field on the critical points of the connectors by means of FEM simulations. They are also meaningful to infer a mathematical law to correlate the values of extinction voltage obtained in reduced-scale connectors with the ones obtained on full-scale models.

Figure 3.14 depicts the corona streamers recorded with a digital camera.

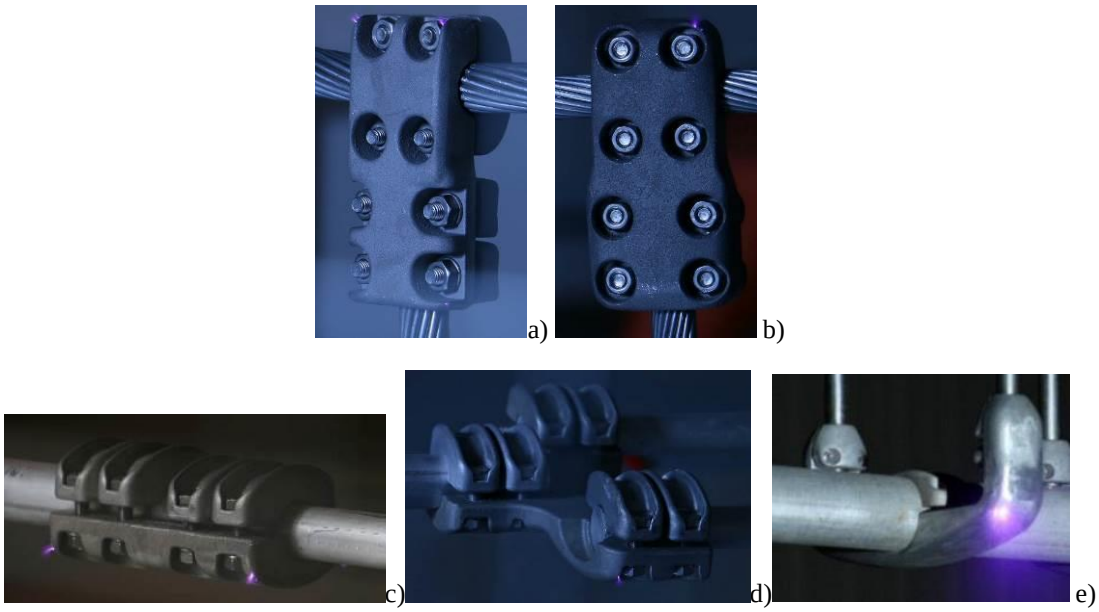

Figure 3.14: Visual positive corona photographs taken with the digital camera of the different models of substation connectors analysed in this section. a) T-type connector J285TLS. b) T-type connector S285TLS. c) Coupler connector J40S33PK. d) Double coupler connector J40S33DPK. e) Duplex T-type connector Z12T390D9DLSP.

Table 3.5: Visual corona tests. Positive corona extinction voltage and height above ground level.

Connector reference	Corrected extinction voltage (kV_{RMS})*	Height above ground (m)
J285TLS (FS)	105.9	1.05
J285TLS (RS)	68.7	0.60
S285TLS(FS)	133.4	1.05
S285TLS(RS)	91.9	0.60
J40S33PK	98.0	0.32
J40S33DPK	101.0	0.45
Z12T390D9DLS	663.0	6.00

*Corrected to standard atmospheric conditions as suggested in [94].

Results of the electric field distribution on the surface of the previously tested connectors appear in Figure 3.15. The same geometry and clearances are employed in the FEM simulations. The voltage applied in the simulations is the corona extinction voltage CEV obtained in the previous stage of visual corona testing.

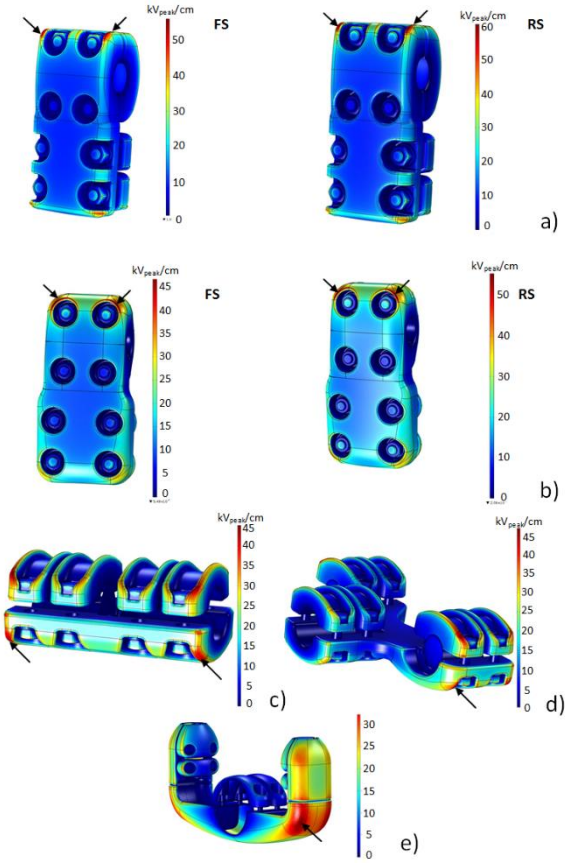

Figure 3.15: Summary Surface voltage gradient obtained by means of FEM simulations, highlighting the critical corona points. a) T-type connector J285TLS (FS and RS). b) T-type connector S285TLS (FS and RS). c) Coupler connector J40S33PK. d) Double coupler connector J40S33DPK. e) Duplex T-type connector Z12T390D9DLSP.

3.5.5 General Peek equation

Recalling *'3.2.3 Peek law'*, the general form of Peek's is as in (3.5).

$$E_c = b \cdot (1 + c/\sqrt{r}) \qquad 3.5$$

Where b (kV_{peak}/cm) and c ($cm^{1/2}$) are parameters, whose values depend on the specific geometry of the problem. This expression is used to determine the relationship between visual corona inception electric field and the curvature radius of the critical corona points. Figure 3.16 depicts the electric field versus the curvature radius of the critical corona points of the seven connectors presented in Table 3.5, two of them being the reduced-scale version of other two. Curvature radius was obtained by means of the CAD designs of each of the connectors. Values of electric field for each connector correspond with the ones obtained for the critical corona points in the 3D-FEM simulations presented in *'3.5.4 Experimental and FEM results'*. Hence, Figure 3.15 uses the data obtained from the visual corona tests, which has been transformed to values of electric field on the critical corona points, and compares the electric field strength at CEV conditions with the curvature radius of the connectors. This results in a hybrid experimental-simulations based approach.

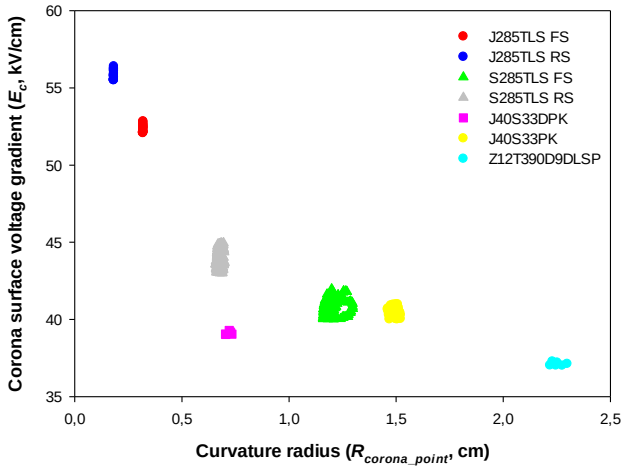

Figure 3.16: Peak value of the visual corona voltage gradient versus the curvature radius of the critical corona points at the connector surface. FS stands for full scale, whereas RS stands for reduced scale.

Figure 3.16 shows a cloud of points (R_{corona_point},E_c) characterizing each of the connectors studied. Each cloud represents the neighbouring points around the critical corona point on the surface of such connector. A unique point for each connector would not be a realistic approach for this study, since corona streamers are never detected in discrete single points. Inopportunely, Figure 3.16 results are far from being properly fitted by applying (3.5). This issue is tackled developing a so-called corrected curvature radius R_c (3.6) that does not only take into account the curvature radius of the critical point, but also its distance with respect to the conductor axis of the connector.

$$R_c = R_{corona\_point} \cdot \frac{D_{corona\_point}}{R_{conductor}} \qquad 3.6$$

R_{corona_point} (cm) being the curvature radius of the corona inception point, D_{corona_point} (cm) the distance between the corona inception point and the symmetry axis of the connector (see Figure 3.17) and $R_{conductor}$ (cm) the radius of the reference conductor. The use of (3.6) makes sense since the connector dimensions grow with the conductor radius. When R_{corona_point} and D_{corona_point} rise, the electric field on the connector surface tends to decrease. This is also seen on bundled conductors in power lines, where the effective radius of conduction is risen in order to reduce the electric field strength on the conductors' surface for a given applied voltage. Hence, instead of (3.5), the expression tailored to deal with diverse curvature radius with their critical corona electric field strength is (3.7).

$$E_c = b \cdot (1 + c / \sqrt{R_c}) \qquad 3.7$$

where E_c (kV_{peak}/cm) is expressed by assuming standard atmospheric conditions, so there is no need to include the relative air density δ.

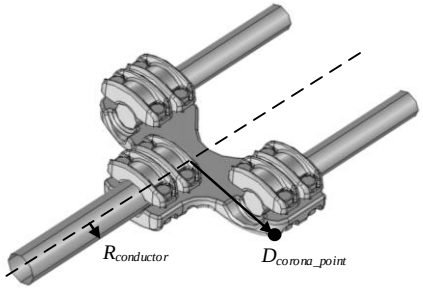

Figure 3.17: a) Connector and the parameters $R_{conductor}$ and D_{corona_point} to calculate the corrected curvature radius R_c.

Table 3.6 summarizes the values of the parameters in (3.6) for all studied connectors.

Table 3.6: Parameters in (3.6)

Connector reference	R_{corona_point} (mm)	D_{corona_point} (mm)	$R_{conductor}$ (mm)	r* (-)
J285TLS (FS)	3.1922	42.8	13.8	3.10
J285TLS (RS)	1.8197	24.5	7.9	3.11
S285TLS(FS)	11.9687	46.0	13.8	3.33
S285TLS(RS)	6.7507	26.3	7.9	3.34
J40S33PK	14.9976	46.7	16.5	2.83
J40S33DPK	7.1904	141.2	16.5	8.56
Z12T390D9DLS	22.5078	252.5	60	4.21

* $r = D_{corona\_point}/R_{conductor}$

Figure 3.18 plots the electric field on the critical corona points of the studied connectors versus the corrected curvature of such areas as well as the fitting of (3.5). For the fitting, the central point of each cloud has been taken into account.

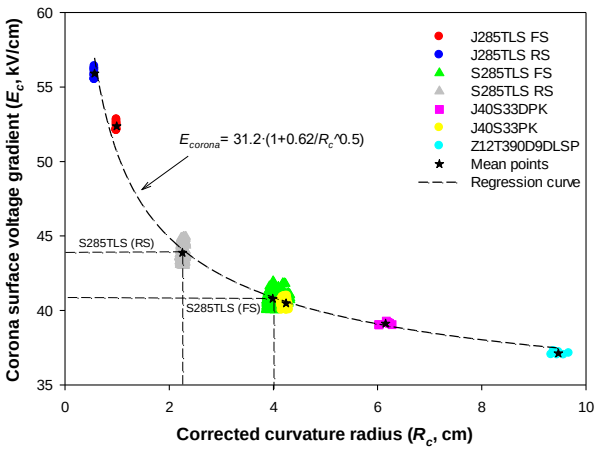

b)

Figure 3.18: Peak value of the visual corona surface voltage gradient versus the corrected curvature radius of the critical corona points at the connector surface.

Table 3.7 summarizes the parameters resulting from the least squares fitting of (3.7) from the experimental/simulation data shown in Figure 3.18.

Table 3.7: Fitting of the parameters of Equation (3.7)

Parameter	Value
b (kV_{peak}/cm)	31.17 (29.17, 33.16)[1]
c ($cm^{1/2}$)	0.6225 (0.5006, 0.7444)[1]
R-square[2]	0.9861
Adjusted R-square[2]	0.9833
SSE (sum of squares due to error) [2]	4.246
RMSE (root mean squared error) [2]	0.9215

[1] 95% confidence bounds

[2] Goodness of fit statistics

Results in Figure 3.18 and Table 3.7 prove a good match between experimental/simulated results and (3.7). Thus, it is validated that (3.7) is able to determine the visual corona electric field and the visual corona onset voltage (from FEM simulations) of the FS connector once those of the RS connector have been obtained from a reduced-scale visual corona test. A relevant observation of the parameters of (3.7) shown in Table 3.7 is that the obtained value of parameter *b* (31.17 kV_{peak}/cm) is very similar to that proposed by Peek for polished round conductors (30-31 kV_{peak}/cm depending on the specific basic geometry).

As a second conclusion of this study, it has also been proved that (3.7) is almost independent of the height at which the connector has been tested, since the results presented herein are based on wide range of heights, between 0.32 and 6 m. Further than the important decrease on corona onset voltage, it is interesting to point out that the height reduction of the tests implies a significant reduction of assembling and testing times.

3.6 Conclusions

Standard corona testing for substation connectors and, extensively, for any high-voltage component require very specific facilities, which are costly and the tests are time-consuming. Two methodologies to tackle the problematic of corona testing have been presented through this chapter. Both methodologies are intended to be used during the optimization stage of high-voltage product development. However, they do not aim to supress standard conformance tests. The first approach aims to reduce the requirements to get insight of corona behaviour of connector combining experimental tests performed in manufacturer facilities and FEM simulations performed under realistic conditions. The most remarkable result is that the extinction electric field for the visual corona tests performed in large-size and small-size laboratories are very similar. This ensures that the results obtained in small-scale industrial laboratories following the approach proposed *'3.3 Reduced voltage tests'* can be useful during the optimal design stage of substation connectors.

The second methodology explores the possibility of performing reduced-scale tests for high-voltage hardware. Based on Peek's law, relationships between scales of connectors have been calculated. To do so, the different values of electric field during corona inception conditions, for different curvature radii of connector surfaces have been taken into account.

Results of both experiences suggest that manufacturer tests empowered with numerical simulations can be an essential tool to assess the corona behaviour of high-voltage hardware and, specifically, of substation connectors.

4 RELIABILITY TESTS

4.1 Introduction

This chapter aims evaluating the life-span of connectors, thus going further from the approaches found in the most extended international standards related to high-voltage accessories. The expected life-span of HTLS connectors is of utterly necessity to be determined as these are intended to work at a superior temperature than their non-HTLS homologs. Substation connections are critical parts of substations, as they simultaneously provide structural and electrical conducting paths. They are supposed to last for decades, and a failure of one of them can drive a part or all of the substation to a major failure. In some cases, it can be pernicious for the rest of the installation or the utility customers. Therefore, in the upcoming scenario of the deployment of substations connected to HTLS power lines, it is a necessity to assess the reliability of the installed products.

Following this brief introduction, the physical origin of the ageing problematic is explained. Later, the standard approaches taken by industry to evaluate the life-span are described, as well as several non-standard approaches to evaluate the life-span of products that already are developed in the bibliography. The last part of the chapter describes the mathematical development of the analysis of a step-stress accelerated degradation test (SSADT) which is the type of test selected as suitable for substation connectors. It also shows the experimental results obtained after a SSADT of a S285TLS connector manufactured by “SBI Connectors, SAU” and the conclusions derived from it.

4.2 State of the art

4.2.1 Contact resistance and contact degradation

When studying the electrical conduction between surfaces, it is necessary to take into account that surfaces are not perfectly flat, nor smooth. If surfaces are explored at micro and nanoscale levels, it is seen how the contacting surfaces form a set of peaks and valleys that resembles the Earth's crust [18], [115], [116]. Therefore, electrical conduction, a path of electrons crossing from one surface to another, is effectively performed in the areas where two of these peaks collide. A study performed within the frame of the Superconnector project, from which this thesis has been carried out, and performed with copper bars with a surface roughness of 0.25 μm, affirms that the ratio of real surface involved in conduction is around 10^{-5} per unit of surface [117]. This fact has important implications in terms of current circulation. Current is forced to transit through the contacts between surfaces called a-spots. Hence, current lines are heavily constricted. This phenomenon is observed as an important drop of voltage through surfaces [18], [118]–[120]. The effect itself is commonly known as contact resistance.

The number of a-spots is directly related to the material, the roughness of the surface and the force applied between the surfaces to ensure the contact. Through time, the amount of a-spots tends to decrease [115] [116]. This is mainly due to mechanical relaxation of materials [121], [122], inference of contaminants and oxides in the a-spots, and under some circumstances, although with far less frequency when dealing with substation connectors, due to electromigration [123], [124] and thermal migration of species [122].

Experimentally, the decrease of the number of a-spots in a contact surface is seen as a rise of the contact-resistance. Contact resistance affects the overall temperature of the connector [125], [126] and simultaneously the aging of a contact is directly related to its temperature. Thus, the drop of the number of a-spots finally drives the contact to a self-accelerated reaction, where its resistance rapidly increases until the contact losses its capacity to conduct electricity [119], [127], [128].

4.2.2 Standard and non-standard study of substation connectors aging

4.2.2.1 Introduction to standard life tests for substation connectors

As previously stated, substation connectors are among the most critical devices of substations. These elements are designed to ensure the current path between different parts of the substation. Simultaneously, they are structural parts of the substation itself. Thus, power utilities and the related industries have developed standards through the national and international certification institutes, to evaluate their reliability under different working conditions through time.

Generally, all standards combine a set of heating-cooling temperature cycles [18] and some of them add planned short-circuits performed to the test loops. The criteria to pass the tests are focused on ensuring that the temperature of the conductor after the cycles and the resistance of the connectors have not surpassed a defined threshold.

These tests barely analyse the real causes of the aging of connectors and propose performance criteria easily applicable for the manufacturers. In the following subsections the most common standard used by the industry is defined in detail. At the same time, an approach to conduct accelerated degradation tests is introduced in order to estimate the reliability of contacts focusing on the real origin of their degradation. To do so, heuristics of aging approaches applied by other industries are reviewed.

4.2.2.2 ANSI C119.4-standard

The ANSI-C119.4 [17] standard proposes the application of temperature cycles to a series of substation connectors. The number of cycles depends on the typology of the connector itself. The temperature of the connector during the test must be 100ºC above the ambient temperature. Tests are passed if during the test, the resistance change is below 5%.

Specifically, for the S285TLS connectors and similar, manufacturers apply 125 cycles as suggested by utilities and installers. Taking into consideration that HTLS conductors can work up to 250ºC, and specifically, for our case of study, that the GTACSR 464 conductor used with the S285TLS connector works at 150ºC, the ANSI-C119.4 test does not represent a real HTLS installation situation.

4.2.2.3 Limits of the standard tests and necessity of non-standard tests

The experience acquired in AMBER laboratory and the experienced opinion of other authors [18] suggests that the information obtained at the end of these standard tests is of questionable use in order to determine the reliability of substation connectors. Specifically, for the S285TLS connector, the HTLS connector focus of this aging study, it is a necessity to know its reliability, as it is intended to work at superior temperatures than those of similar products used in non-HTLS power lines.

The classical study of aging requires the performance of tests where the item under study reaches the end of its life. Then with the temporal data recorded during the tests, the reliability of the product is inferred [129]. In order to get reliable ageing data in a reasonable time, within the temporal frame of normal development of a product, processes of degradation must be accelerated [130], [131]. Several examples of these tests have been applied by different industries. For instance, these methodologies have been successfully applied to estimate the lifetime of home appliances [132], LEDs [133] or MW electronic assemblies [134].

Commonly, these tests are known as ALT (Accelerated Life Tests). In order to determine the life of a product it is necessary to test the same object under different levels of stress of degradation (temperature, humidity, voltage, etc.). Unfortunately, the amount of samples needed for such tests and the life-span of substation connectors, in the order of decades, make them unfeasible even accelerating the ageing process.

Therefore, products such as substation connectors are usually tested by means of another methodology, that not only uses the information of the aging time of the product, but also the information of the degradation process until reaching the end of live. These tests, are known as ADT (accelerated degradation tests). They adjust a mathematical expression based on the kinetic of the reactions involved in the aging of the product, to the data obtained throughout the test. ADT tests avoid reaching the end of the life of the product under test [135], [136].

Although ADTs can ease the performance of substation connectors aging tests, the realization of these tests still involves unaffordable resources for many industries. Specifically, they usually require an important amount of test items to obtain reliable aging data. For instance, for a classical aging study where the ageing is evaluated by means of three levels of temperature, it is necessary to use 3x*n* connectors (where *n* is the number of connectors of one temperature level) to perform the test. Usually in the development stages of a product, when aging tests are required, it is difficult to get such amount of test samples. Also, focusing on substation connectors, these are heated using current circulation so, in most cases, they are connected in series forming a test loop. Therefore, three transformers working simultaneously or three consecutive tests are required.

Realizing that all of the above introduced test methodologies are unpractical to test substation connectors, and taking into account both the knowledge in the degradation physics of contacts previously introduced in 4.2.1, and under the assumption of cumulative exposition described by Nelson [129], it can be proposed that the degradation of the connectors is a memoryless property. So, it is assumed that its rate of degradation is a function only of the applied stress level and it is independent of the previous degradation of the connector.

Under these premises, it is feasible to propose a test where different temperature-stress levels are applied consecutively to the same test population, a SSADT (Step-stress accelerated degradation test). Figure 4.1 graphically explains the concept of the SSADT.

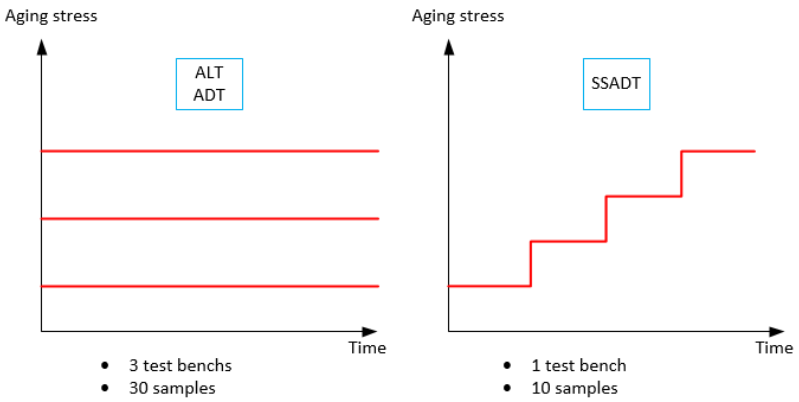

Figure 4.1: Schematic diagram that shows the differences between ALT, ADT, and SSALT and SSADT. The amount of test units necessary to perform the SSADT decreases as the same units are used through different stress-steps.

The mathematical development for the calculation of a reliability value using the data obtained from a SSADT performed to a sample of S285TLS substation connectors is described in the following sections.

4.3 Mathematical development of the step-stress acceleration degradation test (SSADT) for substation connectors

4.3.1 Degradation model of electrical contacts

The degradation process of the electrical resistance $R_j(t)$ of a S285TLS substation connector can be described by the mixed-effect model [137](4.1).

$$R_j(t) = R_{j0} + \alpha_{ij} \cdot t^{\beta} + \varepsilon_{ijk} \quad 4.1$$

Where r_{j0} is the initial resistance at time zero of the *j*th connector, α_{ij} represents the lognormal (LN) distributed drift of the resistance of the different connectors throughout the test (4.2, 4.3), t is the time (in cycles for the test of our concern), β is a constant associated with the degradation mechanism and ε_{ijk} is the measurement error. The error is supposed independent and distributed according to a $N(0, \sigma_{\varepsilon}^{2})$ distribution.

$$\alpha_{ij} \approx LN(\mu_i, \sigma^2) \quad 4.2$$

$\mu_i = a + bx_i$ $x_i = \frac{1000}{273 + T[^{\circ}C]}$	4.3

Thus, the test is defined by six parameters, $\theta = (r_0, a, b, \beta, \sigma, \sigma_{\varepsilon})$.

4.3.2 Reliability model

The reliability of a contact, the resistance of which is distributed following a log-normal distribution, is described in (4.4) as the probability that the resistance measured at a time t is below a maximum allowable threshold value R_{max}. Thus, for a multiple contact connector, its reliability is the product of the probabilities of each contact of the connector to fail (4.5) [137]. The reliability of a contact depends on its initial resistance, the maximum allowable contact resistance and on a set of unknown parameters. The process for obtaining these parameters is described in the following sections.

$$\Re(t \mid r_0) = P\{r_0 + \alpha[t]^{\beta} \le R_{\max}\} = P\{\ln(t) \le \ln(R_{\max} - r_0)/\beta - \ln(\alpha)\} \quad 4.4$$

The probability that the resistance of the connector is bellow an R_{max} value is the integral of the probability density function of values of resistance. Or, 1 minus the cumulative distribution function of the *LN* distribution function $\Phi\{\cdot\}$ (4.5).

$$\Re(t) = \left[1 - \Phi\left\{\frac{\ln(t) - \left(\ln\left(R_{\max} - r_0\right) - \mu\right)/\beta}{\sigma/\beta}\right\}\right]^N \qquad 4.5$$

The first five values of θ_{best} are introduced in (4.5) in order to obtain the percentage of connectors still working at a determined temperature after a determined time –the expected reliability of the connector-. Equation (4.5) takes the form of (4.6) after substitution.

$$\Re(t,T) = \left[1 - \Phi\left\{\frac{\ln(t) - \left(\ln\left(R_{\max} - r_0\right) - \left(a + b\cdot\frac{1000}{273.15+T}\right)\right)\Big/\beta}{\sigma/\beta}\right\}\right]^N \qquad 4.6$$

The sixth value σ_ε, also included within the parameter search, gives insight about the dispersion of the initial values of the contact resistance. It is directly related to the size of the population under test and the number of measurements performed.

It is noted that σ_ε is not included n (4.6) because it represents the standard deviation of ε_{ijk}. Its value is distributed as a $N(0,\sigma_\varepsilon^{\,2})$. And thus, its E($\varepsilon_{ijk}$) = 0. Therefore, when in (4.4) it is stated that the reliability $\Re(t,T)$ is the probability of being the resistance of a contact $r_j(t)$ below a certain value R_{max}, the error in $r_j(t)$ is not introduced as its average value is 0.

4.3.3 Parametric model

At the end of an SSADT, a set of $\{x_1,\ldots,x_K\}$ resistance measurements is obtained, K being the total amount of independent and identically distributed observations. Each of these measurements x_i represents a vector of resistance values, where each one corresponds to the resistance of a contact after the i-th time-step. The data of the test altogether forms an unknown distribution function, where $f_0(\cdot)$ is its pdf.

This unknown distribution belongs to a family of distributions $\{f(\cdot|\theta),\ \theta \in \Theta\}$ known as parametric model. Thus, f_0 corresponds to $\theta = \theta_0$, the true value of the set of parameters. Therefore, the aim of the study is to calculate $\hat{\theta}$, the closest estimator of the true value θ_0.

The probability that the set of measurements fits a determined set of parameters is the product of the probabilities that each of the sets fits with the same set of parameters. This is usually called the joint probability function [137], [138] :

$$f(x_1,x_2,\ldots,x_K|\theta) = f(x_1|\theta)\cdot f(x_2|\theta)\ldots f(x_K|\theta) \qquad 4.7$$

Summarizing, (4.7) is the probability that $\{x_1,\ldots,x_K\}$ correspond to a set of parameters θ.

Usually, the concept of probability is used to calculate the existing chances that a value x_i fits a parametric model θ. Our case differs slightly from the probability definition as a model is intended to be obtained by means of a set of existing data. The resulting function is called Likelihood function and it is mathematically expressed as in (4.8). Note that in (4.7) f is considered a function of θ given the set of measurements $\{x_1,\ldots,x_K\}$.

$$f(\theta|x_1,x_2,\ldots,x_K) = f(\theta|x_1)\cdot f(\theta|x_2)\ldots f(\theta|x_K) \quad 4.8$$

Each of the products of the right-side of (4.8) stand for the pdf of the data sets for each contact, temperature step and measurements taken at each of the temperature-steps. Equation (4.9) expresses equation (4.8) in a more formal manner showing on the left-hand of the expression the likelihood L as the function of the previously described parameters, conditioned by the experimental measurements of resistance of each of the evaluated contacts. On the right-hand it is formally descripted the product that appears in (4.8), as the products of the aforementioned pdfs. It is noted that P is the product of the n evaluated connectors per N contacts in the connectors, thus resulting in $P=nxN$. M is the number of steps of temperature considered in the SSADT and k_i the number of measurements performed at each temperature step.

From (4.8) it results,

$$L = \prod_{i=1}^{M}\prod_{j=1}^{P}\prod_{k=1}^{k_i} f(r_{ijk}) \quad 4.9$$

The product form of expression (4.9) complicates the following task of finding the parameters that best describe the ageing model. Hence, logarithms are applied at both sides of the equation (see 4.10). So, the log-likelihood function for all degradation increments of P items at each M temperature step and for k_i inspections (the sum of all inspections is $K=\sum_{i=1}^{M} k_i$) within the i^{th} step is given as,

$$\ln L = -\frac{1}{2}\sum_{j=1}^{P}\ln\left\{\int_{-\infty}^{\infty}\prod_{i=1}^{M}\prod_{k=1}^{k_i}\frac{1}{\sqrt{2\pi}\sigma_\varepsilon}\exp\left\{\frac{\left[r_{ijk}-r_0-\alpha_{ij}\cdot {t^*}_{ik}^{\beta}\right]^2}{2{\sigma_\varepsilon}^2}\right\} f(\alpha_{ij})d\alpha_{ij}\right\} \quad 4.10$$

Note that $f(r_{ijk})$ stands for the pdf of a normal distribution $N(\alpha_{ij}\cdot {t^*}_{ik}^{\beta},\sigma_\varepsilon)$. The integral in (4.10) can be simplified using the integral mean value theorem. To do so, it is necessary to consider that α is the same for all connectors and so $\alpha_{ij}=\alpha_i$.

As α_i is an infinite distribution of values, the way to infer a representative value of it, is to calculate its expected value. For a LN distribution the expected value takes the form of $E(\alpha_{ij}) = \exp(\mu_i + \sigma^2/2)$. Substituting $E(\alpha_{ij})$ in (4.10), results in (4.11).

$$\ln L = -\frac{1}{2}\sum_{i=1}^{M}\sum_{j=1}^{P}\sum_{k=1}^{k_{i+1}}\left\{\left[\ln(2\pi)+2\ln(\sigma_\varepsilon)\right]+\left[\frac{\left[r_{ijk}-r_0-\exp(a+b\cdot x_i+\sigma^2/2)\cdot {t^*}_{ik}^{\beta}\right]^2}{{\sigma_\varepsilon}^2}\right]\right\} \quad 4.11$$

In (4.11), t^* is the equivalent time of the time-step, which is given by (4.12).

$$t_{ik}^{*} = w_i + t_{ik} - \tau_i \quad 4.12$$

$$w_i = \left(\frac{\alpha_{i-1}}{\alpha_i}\right)^{1/\beta}\cdot(w_{i-1}+\tau_i-\tau_{i-1}) \quad 4.13$$

The necessity of an equivalent time t^* is graphically described in Figure 4.2. In blue, three paths of degradation appear due to three different degradation stresses. Each of the subsequent stresses is harder than the previous. So, each degradation path has a larger slope than the previous one. As temperature is the main contributing factor to the acceleration of the kinetic of the chemical reactions that lead to degradation of the contact and its ulterior failure[119], [137] the three levels of degradation correspond to three levels of temperature.

The data obtained by means of a SSADT follows different degradation paths as the test is performed over the same population and by applying different levels of temperature through time. Hence, in order to effectively concatenate the data when searching the parameters of the parametric model that describes the aging of the contact under study, it is necessary to place the starting value of resistance after a cycle exactly at the time where it was supposed to be in the next step if this has been applied since the beginning of the test. This value of time is known as w_i and its calculation appears detailed in (4.13).

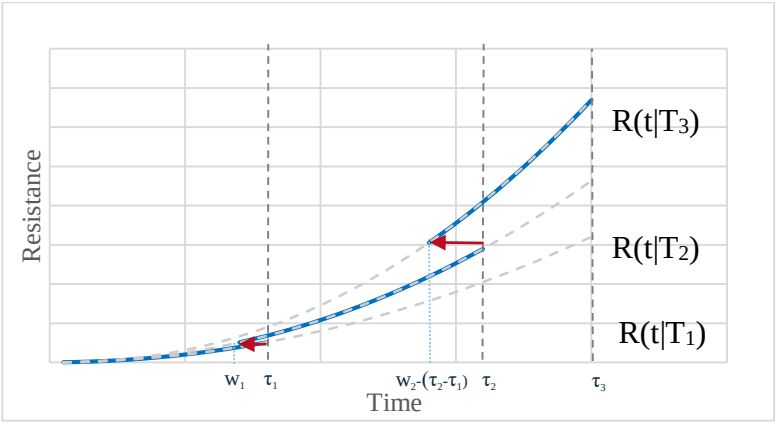

Figure 4.2: Explanatory plot of the degradation process due to different temperature stress paths in an SSADT.

4.3.4 Maximum Likelihood Estimation (MLE)

Previously, it has been stated that the parameters within a parametric model that provide the highest value of likelihood, are the ones that best fit with the experimental data. Therefore, the parameter search is a maximization problem that can be tackled using an optimization approach. Specifically, the optimization objective is to maximize the value of ln$L$ in equation (4.11). As stated, the θ_{best} parameters obtained are the ones which are closest to the ideal set of parameters θ_0 that fit the connector aging process, and thus the ones that would let to calculate the closest value of reliability to the real reliability of the product.

There are several derivative and non-derivative algorithms to tackle with optimization problems in the literature. Due to the non-linearity of the ln$L$ equation, and for facility to implement, an evolutionary optimization approach has been proposed. Specifically the 'Stochastic Fractal Search' is recommended for ease of use and velocity to obtain results comparing with other known methodologies, such as genetic algorithm or particle swarm optimization [139]. All of these methodologies are designed to find out optimal values of a function. So, in order to get a maximum, the objective function of the algorithms is the minimum of the negative of the ln$L$ (4.11) as shown in (4.14).

$$obj : \min - \ln L \qquad 4.14$$

As a result of the optimization, the best parameter set obtained is $\theta_{best} = (r_0, a, b, \beta, \sigma, \sigma_\varepsilon)$.

4.3.5 Description of the optimization method: *Stochastic Fractal Search (SFS)*

4.3.5.1 Introduction to optimization metaheuristics

In the preceding sections of this chapter it has been introduced that the calculation of the parameters that maximize the ln$L$ is unfeasible by means of derivative approaches.

Thus, the use of a metaheuristic, a general procedure –non-restricted to a specific problem- properly tailored to efficiently sample the space of near-optimal solutions of the optimization problem, becomes necessary [140].

Most optimization metaheuristics are inspired by natural phenomenon. For instance, the genetic algorithm (GA) [141] uses Darwin theory to mimic the natural evolution process in order to create more robust individuals. Other popular metaheuristics such as the particle swarm optimization (PSO)[142] and the artificial bee colony (ABC)[143] base their rules in the behaviour of bird flocks and bee colonies respectively. All these examples of metaheuristics and many others face the problem that they don't guarantee fast convergence along with accuracy. Also, in many cases their use requires a deep understanding of the underlying mechanism of the algorithm in order to properly set a numerous amount of ruling parameters.

In order to overcome the shortcomings of other metaheuristics, Salimi [139] developed the stochastic fractal search (SFS) algorithm. The algorithm provides a new insight into finding the solution of optimization problems based on the branching property of dielectric breakdown (see Figure 4.3). This phenomenon can be successfully described with fractals. And so, a set of particles that have the function of browsing the solution space are programed to move among this space following the mentioned fractal behaviour. The method is able, thus, to provide a solution that has a small error with respect to the global optimum solution, with a minimal number of iterations. A comparison of the performance of this metaheuristic with respect to other optimization algorithms is found in Salimi [139].

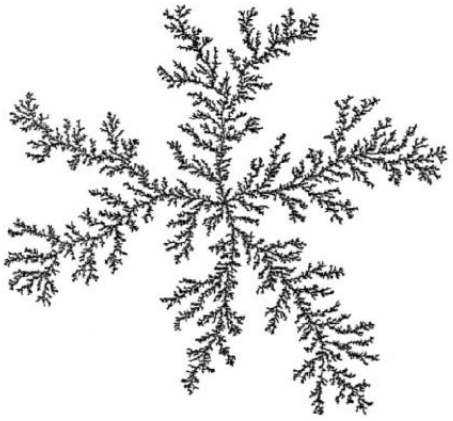

Figure 4.3: Example of fractal growth imitating the breakdown of an insulator [139]

4.3.5.2 SFS metaheuristic working principle

Stochastic fractal search metaheuristic works as follows. First, a set of particles is randomly initiated all over the domain of the solution. The space of solution has as many dimensions as unknown variables of the equation to optimize, six in this study. These particles have a value of electrical potential that is the result of the ln$L$ for the exact location of the solution domain. After the initial step, the particles randomly diffuse around its current position to intensify the range of the solution domain explored by the algorithm. Diffusion stands for division of the particle into several particles. The random process employed for simulating diffusion is the Gaussian walk. The length of this walk is reduced as the algorithm performs iterations. This first step is intended to increase the chances of finding the global minima and for preventing falling in local minima. Then, the best generated particles of each former particle, the ones with lowest value of ln$L$, are selected for the second step of the algorithm. In this step, the selected particles update their position based on the position of other particles. Once again the value of ln$L$ is computed and the lowest one is selected as the best solution.

The process described in the previous lines is repeated until finding convergence. Convergence is reached when the value of the resulting lowest value of ln$L$ after several iterations, changes less than a specified tolerance value.

4.4 Experimental analysis of the reliability of the HTLS connector

4.4.1 Test assembly

Figure 4.4 shows a draft of the test assembly used for the determination of the reliability of substation connectors. Figure 4.5 shows the assembly, once physically mounted in the facilities of AMBER laboratory. Ten S285TLS HTLS substation connectors of SBI Connectors, S.A.U. were tested, once attached to eleven segments of HTLS conductor GTACSR464 of Trefinasa of D = 27.6mm (Annex 1 and 2 includes the physical properties of the test elements).

The number of connectors under test was the total number of available connectors in AMBER laboratory. Nevertheless, it is worth pointing out that the number of connectors under test could not be much higher, due to limitations of the maximum available thermocouples and tests running in parallel. It is also important to note that a higher number of connectors leads to a better accuracy of the calculated value of the reliability of the object under test.

During the test, and due to a human error, one of the connectors (R1) was damaged during one of the required temperature cycle stops necessary to measure the resistance. Consequently, it was replaced by another similar connector and the results obtained from the resistance measurements were discarded. So, the data shown hereafter will include the analysis of 9 identical S285TLS connectors.

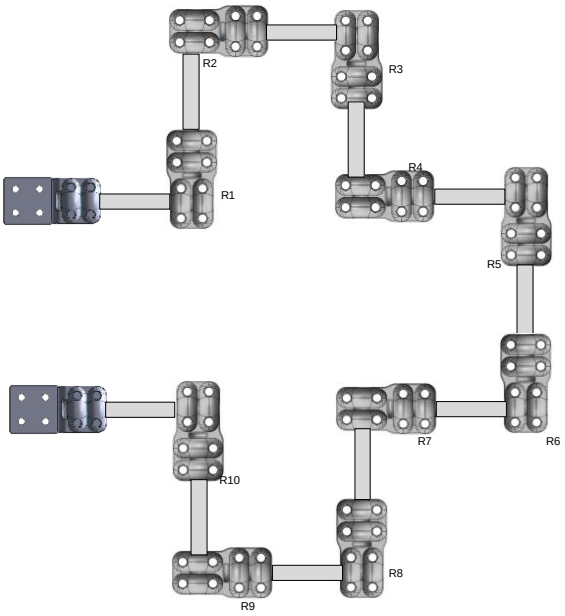

Figure 4.4: Draft of the distribution of connectors for the SSADT test.

Figure 4.5: Experimental loop tested in AMBER facilities of the UPC to conduct the SSADT test.

4.4.2 Resistance evolution test results

Figure 4.6 shows 18 curves of the resistance evolution of each of the contacts of the S285TLS connectors dealt with. To obtain these data, several temperature cycle tests were performed between the months of July and October of 2017. Four steps of temperature T[ºC] = (100, 110, 125, 150) were applied consecutively to the connectors under study. Whenever a connector failed, it was substituted by a similar connector in order to maintain the electric path and let the test to continue. Failure of connector was seen as a sudden rise of resistance linked with a visible deterioration of the connector, as seen in Figure 4.6. Failed connectors had their contacts burned due to the temperatures reached because of the rise of resistance as it is seen in Figure 4.7.

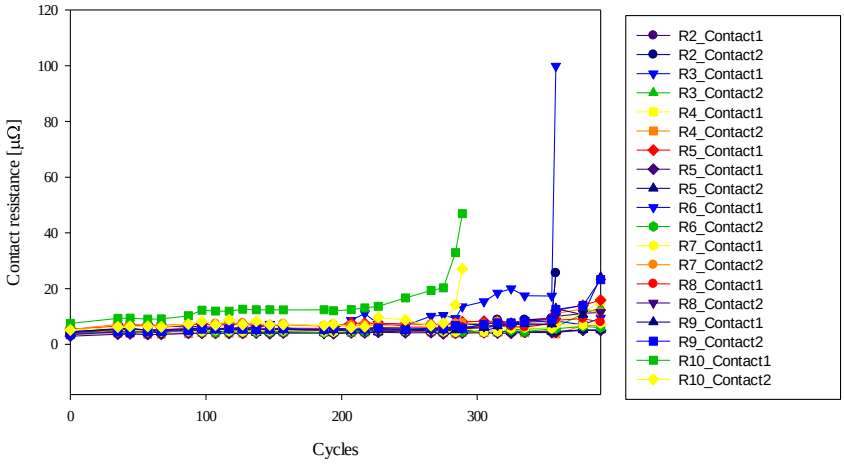

Figure 4.6: Evolution of resistance through cycling tests

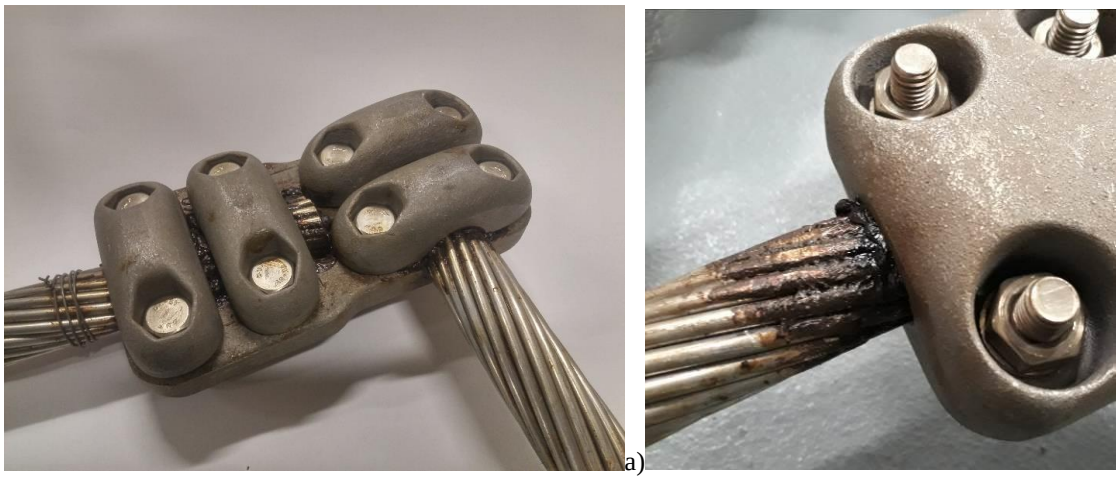

a)

Figure 4.7: a) Failed connector after SSADT test b) Detail of the burned contacts of the connector

4.5 Discussion of results

4.5.1 First model results and reliability calculation

After the test performance, the parameters required to infer the value of connector reliability are calculated following the previously explained methodology based on the SFS metaheuristic. These values are shown in Table 4.1.

Table 4.1: Parameters obtained by means of SFS that best fit the aging of the S285TLS connector

Parameter	Value
R_0 (Ω)	5.2465
a	17.4758
b	-10.1395
β	0.2738
σ	3.7473
σ_ε	5.0091

Figure 4.8 shows the evolution of reliability of the connectors calculated by means of the parameters in Table 4.1. These values have been calculated taking into account an expected life of a substation -40 years- and an operating temperature of the connector of 100ºC. From the curve it can be concluded that it exists a percentage of 'child-death' of substation connectors within the range of 0.5 – 1.5%. Data in Figure 4.6 shows that the connectors with higher initial resistance suffer from a clear tendency to age faster. Thus, it is evident that these are the connectors related with the values of 'child-death' seen in Figure 4.8. Hence, an efficient manner to increase the reliability is to ensure, during installation, a sufficiently similitude among the resistance of all connectors. If the resistance of the connector during installation is not below a settled threshold value, it is recommended to substitute the connector in order to avoid future problems of fast aging.

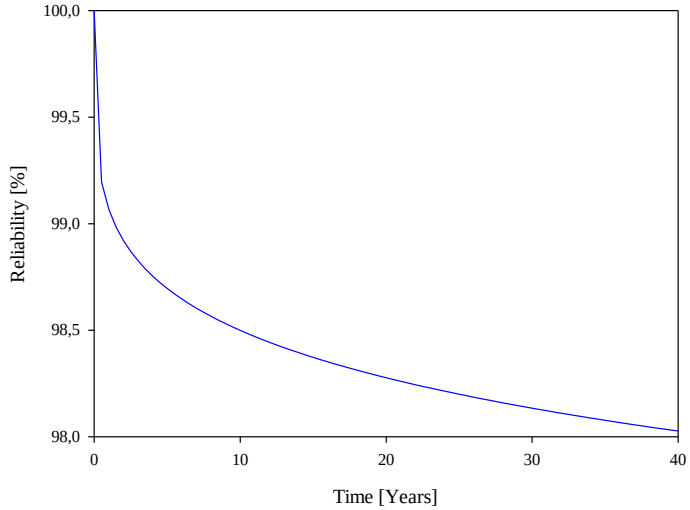

Figure 4.8: Reliability evolution of the S285TLS connector working at 100ºC

4.5.2 Sensitivity analysis

4.5.2.1 Introduction

The use of a parametric model to infer the value of reliability of a product has implicitly a factor of uncertainty. This uncertainty has different origins and can be assigned to the values of the parameters used as input of the model [144].

Therefore, this section aims to variate the assumptions by which the reliability of connectors has been calculated in *'4.5.1 First model results and reliability calculations'*. This is carried out in order to test the robustness of the model itself and to increase the understanding of the relationship between the inputs and outputs of the model [145].

Four factors are analysed in this section. The first of them is the temperature of the connector considered as working temperature. In the previous section this has been set to 100ºC. The chosen value is based on the temperature observed during the temperature rise tests (TRT) performed over the S285TLS connector and shown in *Chapter 2*. Nevertheless, the value of temperature obtained on such tests depends on the ambient temperature and the position of connectors with respect with the testing room. So, the working temperature is a value obtained under restrictive test conditions, and which occasionally can differ from the final temperature at which the connectors will work. For instance, this is seen when connectors are installed on warmer or colder places than the ones where they were tested.

The second factor to be analysed is the expected lifetime of the connector. Commonly, when manufacturers think in the life of a connector, they assume about 40 years of use, as this value matches with the common life of substations. Nonetheless, the number of years that the product will actually face installed is unknown, and there could be chances to find connectors installed further than the life-times proposed by manufacturers. Thus, it is an interesting exercise to propose longer times of installation for the assessment of reliability.

Following, after analysing the experimental data of *'4.4.2 Resistance evolution test results'*, it is seen that one connector (R10) started the test with a too high value of r_0. To evaluate the inference on the reliability results presented on the preceding section, this results will be discarded and the reliability will be calculated with the remaining data-set.

Also, due to a series of observations detailed thoroughly in its section, it has been considered to perform a sensitivity analysis where the outlier of the data sample is removed. Specifically, the results of reliability will be calculated without taking into account for its calculation the evolution of resistance of the connector that starts the test with the highest resistance, R10.

Finally, as a way to show the influence of R_{max} in the calculation of the reliability of connectors, three curves will be shown for the two first evaluated parameters. Each of these studies will show the reliability of the connector versus the evaluated parameter, considering R_{max} as a value of contact resistance 1.5, 2 and 3 times higher than the original one. It is worth noting that R_{max} has been chosen originally as 3 times the original one, taking into account that the resistance of the connector exhibits a behaviour of rapid and irreversible deterioration. Nevertheless, a manufacturer would like to assure that its product never reaches an irreversibly destructive state. This is the reason why it is interesting to explore how life-expectancy evolves by modifying this parameter.

4.5.2.2 Temperature sensitivity

Figure 4.9 shows the evolution of reliability of connectors with respect to the working-temperature of the connector after 40 years of use. Reliability exponentially decays with the rise of working temperature. It is worth noting that the accuracy of the predicted values of reliability for values of temperature that fall beyond the maximum tested temperature is discussible.

Altering the value of R_{max}, affects the slope of the evolution of reliability with respect to temperature. So, for lower values of R_{max} the reliability of connectors drops after 40 years for the same working temperature.

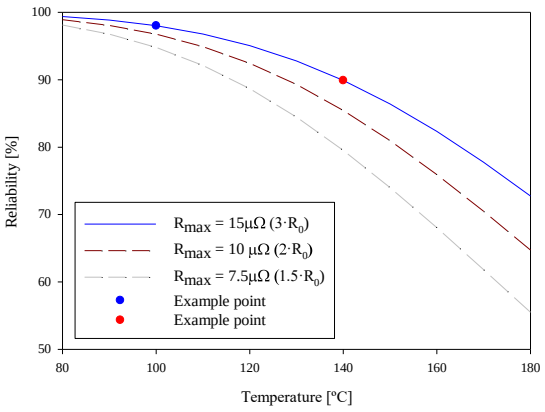

Figure 4.9: Drop of expected reliability of connectors after 40 years of use with respect with the working temperature of the connector

For instance, in the example shown in Figure 4.9, a connector working at a temperature of 100ºC, see blue marker, would have a reliability of 98.03% after 40 years. Meanwhile, the same connector working at 140ºC, see red marker, would have a lower value of reliability, 89.91%.

4.5.2.3 Lifetime sensitivity

The use of longer life-time values shows again (see Figure 4.10) that the percentage of failure is mainly occasioned due to early-life deterioration. Setting lower values of R_{max}, the main effect is that more connectors fall during their early-life.

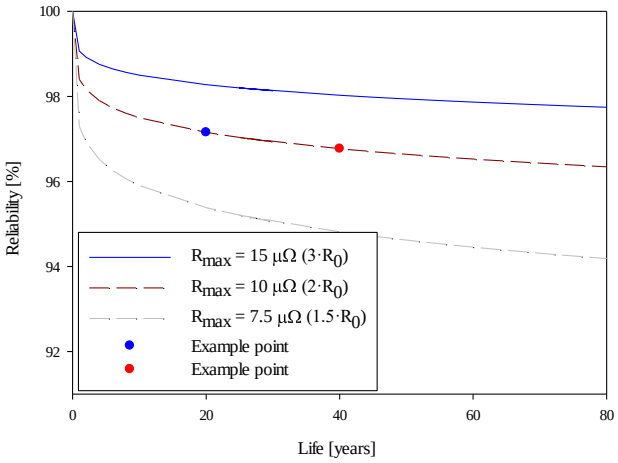

Figure 4.10: Reliability of substation connector further for very long times of installation for T=100ºC

For instance, in the example shown in Figure 4.10, the reliability of a set of connectors after 20 years would be 97.16%. For a longer time of 40 years, the reliability of the same set of connectors, see red marker, would be 96.77%. Reliability decreases faster between the start of the operation time and the blue example point in Figure 4.10, than between this point and the red example point. This remarks the importance of the decrease of early-life deterioration in order to increase the reliability of such products.

4.5.2.4 Effect of outlier removal

Recalling *'4.3.2 Reliability model'*, the value of σ_ε, calculated using the aforementioned model and shown in Table 4.1, is the variance of the error of the evolution of the contact resistance, which is distributed as a $N(0,\sigma_\varepsilon^2)$. The value obtained for the parameter in *'4.5.1 First model results and reliability calculation'* is abnormally high. It is about the same value as the contact resistance initial value for the S285TLS connector.

The origin of such high value could be found either in an abnormal recorded test value or in insufficient number of samples used during the test. As it has been explained in *'4.4.1 Test assembly'*, the number of samples used has been the maximum available by that time of the S285TLS connector. The assembly of the connectors was the same for all of them, and special care was taken in order to ensure that the same torque strength was applied to all bolted unions, to ensure a suitable and uniform installation. One of the connectors, the one closer to one of the transformer terminals, failed during the test due to an accidental overheating, and thus, was discarded for the test. The rest of the connectors had similar initial resistance values, despite of R10, which started the test with almost twice the initial resistance of the rest. To see its inference in the global result of the model and its effect in σ_ε, a parametric study has been run after removing the data of this test.

Table 4.2 shows the results of the parametric study discarding R10. The value of R_0 is very close to that obtained without removing the outlier. Values *a*, *b* and β differ notably because they have to adapt to a less dispersed set of resistance values. Considering that the parameters do not have a direct physical meaning, their change is because of the optimization algorithm adapts the parameters to the input data. The value of σ increases because the resistance distribution resembles less to a LN distribution. This fact implies that the fidelity of the equation describing the resistance evolution is compromised. Finally, σ_ε drops by 5 times below the average initial resistance, sincethe data set is more concentrated in one point.

Table 4.2: Parameters obtained by means of SFS that best fit the aging of the S285TLS connector discarding R10 connector.

Parameter	Value removing R10	Value withouth removing R10
R_0 (Ω)	4.9510	5.2465
a	1.3205	17.4758
b	-8.6959	-10.1395
β	0.6083	0.2738
σ	5.8939	3.7473
σ_ε	1.6203	5.0091

Figure 4.11 displays the effect on the predicted resistance evolution of the different parameters obtained with and without removing the outlier R10. Equation (4.1), shown below these lines as (4.15), has been used to calculate the curves. The parameters obtained from the original data set give a curve (black curve in Fig. 4.11) of resistance evolution seen as a steady rise of resistance that matches with what experience suggests as normal. On the contrary, when introducing in Equation (4.15) the parameters obtained after eliminating the supposed R10 outlier, the evolution of resistance obtained lacks of physical resemblance with reality. It rises at a velocity higher than expected (blue curve in Fig. 4.12). The cause of this effect can be found in the rise of σ. The parameter σ accounts for the goodness of the fitting of the data set in the proposed LN distribution. It has a quadratic effect on the calculation of $E(\alpha_{ij})$, which is one of the parameters that modulate the growth of resistance through time. The LN distribution is especially suited for data samples where values far from the statistical mode appear in one of the extremes of the distribution. So, the LN distribution is designed to take into account values that a priori could be considered as outliers. Therefore, the removal of these values produces an ill calculation of the parameters, thus generating odd solutions, as seen in Figure 4.11.

$$R_j(t) = R_{j0} + E(\alpha_{ij}) \cdot t^{\beta} + \varepsilon_{ijk}$$

$$E(\alpha_{ij}) = \exp(\mu_i + \sigma^2/2) \qquad 4.15$$

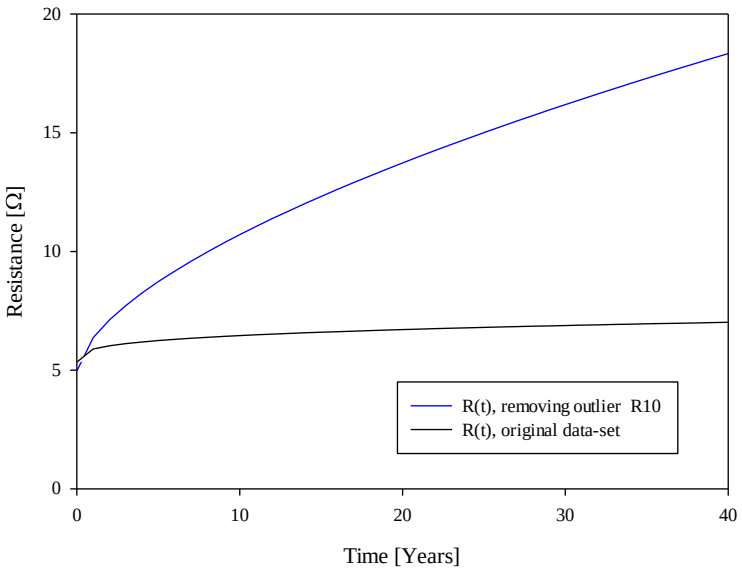

Figure 4.11: Reliability evolution of the S285TLS connector working at 100º C

Figure 4.12 shows the reliability evolution through the expected in-service time of substation connectors. The percentage of failed connectors after 40 years is around 0.35% is almost 6 times less than the 2% obtained previously.

The rise in connector reliability suggests that by neglecting the connector that started the test with highest resistance, the remaining sample set lacks of the real variability of contact resistance seen during field assembly. The important drop in error variability is because the parameters have been calculated with a more homogeneous set of experimental results. Once again, the important value of σ affects the value introduced in $\Phi\{\cdot\}$ in Equation (4.6), shown below as (4.16).

$$\Re(t,T) = \left[1 - \Phi\left\{\frac{\ln(t) - \left(\ln\left(R_{max} - r_0\right) - \left(a + b \cdot \frac{1000}{273.15 + T}\right)\right) \Big/ \beta}{\sigma / \beta}\right\}\right]^N \qquad 4.16$$

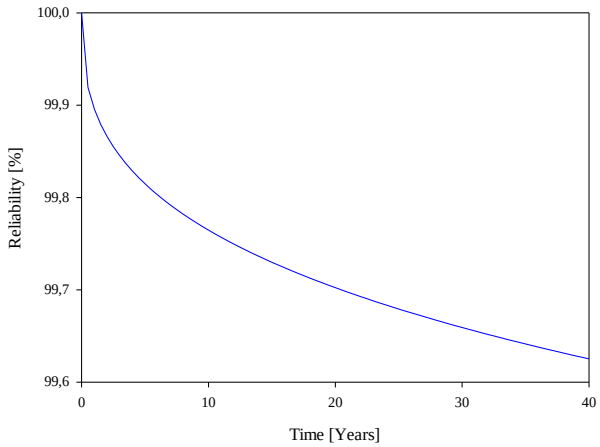

Figure 4.12: Reliability evolution of the S285TLS connector working at 100ºC

The aim of neglecting the highest resistance data has not been to suggest that an abnormal value of resistance must not be considered for the model. On the contrary, the connector that failed prematurely was properly assembled. After noting the anomalous high initial resistance, it was reassembled and retightened, not noticing any relevant drop in resistance. So, the cause of the initial resistance of the connector was out of human control. This scenario is perfectly normal in real conditions and thus it has to be taken into account as done in *'4.5.1 First model results and reliability calculation'*. Therefore, the reason for which the sensitivity study has been performed, is to point out that when testing real connectors samples, due to the LN shape of the distribution of these data, abnormally high values of error variance σ_ε can appear. This fact does not necessary mean that the tests performed are invalid. Quite the reverse, the resistance evolution curve introduced in the model to infer values of reliability takes into account natural but high values of initial contact resistance.

As a conclusion, when the data-set is not very numerous an outlier element can affect notably σ_ε, which accounts for the dispersion of the paths of resistance increase.

4.6 Conclusions

Determining the reliability of a long-lasting product is an exercise of paramount complexity. Frequently, the time to obtain data is short, the samples scarce and the facilities are limited. After a thorough review of the standards and based on several experiences performed in AMBER laboratory and respected opinions found in the bibliography [18], it has been determined that standard ageing tests lack of a physical approach of the phenomena involved during the ageing process. The duration of them is usually short and the data obtained is useless in terms of inferring the reliability of the product under test.

This chapter aimed to apply methodologies successfully implemented in other engineering fields to get an insight of the real life-expectancy of substation connectors. Specifically, the SSADT has been applied over a sample of ten S285TLS connectors.

The result of the test has brought up that the reliability after 40 years of this model of connectors working at a temperature of 100ºC is around 98%. The temperature used for this calculation is the working temperature of the connector under normal conditions, when attached to a HTLS conductor. It is worth noting, as well, that most of the failure of the connectors appears during the "infancy" of the installed connector. Results also show a direct relationship between initial resistance and expected life of the connector. Higher values of contact resistance after installation, lead to higher temperatures during connector use, and finally, to early failure of connectors. Thus, this study lets to firstly conclude that a right assessment of the contact resistance of connectors just when these are installed ensures a longer life in service.

Finally, due to an abnormally high value of variance of the measurement error, a sensitivity analysis of the data has been performed. The value of σ_ε notably decreases when neglecting the connectors with higher initial resistance. The drop of σ_ε gives insight of the real meaning of the parameter, when taking into account the full sample of connectors. The only way to effectively decrease the value of σ_ε, without neglecting any dataset, is by increasing the amount of samples used during the test. However, in many cases, due to the aforementioned limitations (time, samples, facilities), this is unfeasible.

Compared to the standard approaches used nowadays by industry, the application of new approaches of accelerated ageing tests based on the evolution of the resistance of the connectors, is able to provide a value of reliability for a product. To do so, it forces the samples to be degraded. This state of degradation is not observed when performing standard tests. In them, apart from an initial rise of resistance due to mechanical relaxation, no other rise of resistance is measured. The results herein presented, aim to encourage other participants of the power industry to question the methodology by which they are assessing the life of the items that they design or install.

5 CONCLUSIONS

From 2015 to 2040 it is expected a rise of net electricity generation of 1.9%/year for non-OECD countries and a 1.0%/year for OECD countries. Installing new power lines in developed countries is either unfeasible in terms of right-of-way restrictions or costly. Rising the distribution voltage or increasing the section of conductors involves structural changes on power grids that end being as expensive as adding new power lines to the system. Thus, HTLS conductor technology arises as the best option to adapt the power grid to the future increase of power demand. Nevertheless, the fact that these sort of conductors work at a higher temperature due to their higher current density, makes it necessary to develop new accessories for power lines. Specifically, this work has been devoted to substation connectors, as it was conceived as a public-private collaboration between Universitat Politècnica de Catalunya and SBI Connectors SAU, a Spanish connectors manufacturer. This hardware has to be designed to work at higher thermal stresses for HTLS applications. It also requires a similar expected lifetime as the actual substation hardware, and to be corona-free. To check the suitability of the developed HTLS products, all testing methodologies applied during the optimization stage of the products had to be reviewed as they were designed for less demanding stresses. The fact that higher-demanding products need higher-demanding tests, and that industrial tests need to be performed in industrial laboratories, which are usually limited in terms of power, size and disposable time to perform tests, justified this work in the form of a doctoral thesis.

After the introductory chapter, the second chapter of the thesis was devoted to the redesign of thermal tests performed on substation connectors. Up to now, the tests to validate these products require the use of powerful high-current transformers. Using HTLS conductors implies a notable rise in the current circulating through power-lines and fittings, such as connectors. Therefore, a reduced-scale test approach was suitable to study their behaviour, while simplifying test requirements, such as maximum current, energy consumption, size of the generators, or testing time among others. In order to ensure similarity between scales, it is a necessary condition to ensure that the non-dimensional numbers that govern the equations describing the phenomena are the same. The process of heating involved in the temperature rise test is the non-adiabatic heating with cooling by means of conduction, convection and radiation.

Therefore, by means of the Pi Buckingham theorem, the non-dimensional values that describe the physics of the problem are obtained. From these values, the relationship between applied current and scale of the reduced-scale sample has been obtained (5.1).

$\frac{I_{RS}}{I_{FS}} = \frac{1}{n^{3/2}}$	5.1

The other thermal test studied has been the short-circuit test. The heating process of connectors under this test is adiabatic. Thus, no cooling by means of conduction, convection or radiation is considered during the application of current. This time, due to the simplicity of the equations, it has not been necessary the Pi Buckingham theorem to obtain the non-dimensional relationship that characterize the problem (5.2).

$$\frac{I_{RS}}{I_{FS}} = \frac{1}{n^2} \qquad 5.2$$

Equations (5.1) and (5.2) have been validated by means of computational simulation and experimentation.

Computational simulations aimed to validate the approach to reduce the scale of tests were carried out by means of the 3D-FEM method. Also, a 1D-FDM methodology was developed in order to obtain data of the temperature profiles along the conductor and the connector faster than using a 3D-FEM approach. Both methodologies of calculation have taken into account the material properties of the connector, the behaviour of the contact, and the mechanism of the cooling by means of conduction, convection and radiation. The evolution and final values of temperature matched with the predicted by means of the developed relationships and the 3D-FEM simulations. In order to get reliable simulation results, the values of the parameters characterizing the material and the contacts have been used from the a previous work related to the design of HTLS connectors of Capelli. This work has been part as well of the project Superconnector from which this thesis was funded. Experiments where run both at Amber laboratories (Terrassa, Spain) and Veiki laboratories (Budapest, Hungary).

The third chapter has been dedicated to explore the methodologies to simplify experimental corona tests for substation connectors. Nowadays, these tests need to be performed in screened laboratories. They also require complex and expensive PD detection measurement devices, thus limiting their applicability in many industrial laboratories. Two methodologies to reduce the requirements to perform these tests have been developed. Both are based on the determination of the electric field on the surface of the connector by means of 3D-FEM simulations, and on the detection of visual corona by means of a commercial digital camera. The first methodology, the reduced voltage corona test, is designed to reduce the spatial and technical requirements to perform such tests. To reproduce the tests at a lower height, the electric field on the surface of the connectors placed at the original test height has been calculated by means of 3D-FEM simulations. Corona inception is produced whenever the electric field on the surface of a connector surpasses a threshold value. Thus, in order to reproduce the test at a lower height, the voltage at the reduced height has to be calculated by means of 3D-FEM simulation as well. Decreasing the height of the connector involves lower values of voltage to reach the corona inception electric field. As a result of this study, substation connectors that needed to be tested at voltages over 200 kV and at a height of 7 m, have been tested using a facility with a maximum output voltage of 130 kV and at less than half a meter over the ground-plane. Thus, the facilities involved (generator, room, elevator) decrease notably, as well as the assembling time and the laboratory requirements decrease dramatically.

The third chapter has introduced a methodology to perform corona tests for reduced scale samples. Corona inception is a nonlinear process, since for identical ambient conditions and applied voltage, it depends on the curvature radius of the electrode surface. This study extends the Peek law, which relates the radius of cylinders with the electric field value at which corona discharges appear, to more complex geometries, such as connectors. To do so, the electric field strength on the surfaces of connectors calculated by means of 3D-FEM has been correlated with the applied voltage, curvature and eccentricity with respect to the axis of the connector of that surface point. At the end of this study, equation (5.3) relating the aforementioned factors has been obtained.

$$E_c = 31.67 \cdot (1 + 0.6225 / \sqrt{R_c})$$

$$R_c = R_{corona\_point} \cdot \frac{D_{corona\_point}}{R_{conductor}} \qquad 5.3$$

Equation 5.3 lets to know the electric field for corona inception for a curvature radius of a complex geometry. Therefore, it provides the relationship of the inception electric field for connectors of different scales with their curvature radius.

The benefits of the development of a method to test connectors at a reduced scale are multiple. First, facility requirements to perform the tests are decreased notably, as voltage to perform tests on reduced-scale samples decreases. Also, the assembly of reduced-scale samples is easier, as samples are lighter and more manageable. Finally, the use of reduced-scale samples opens the possibility of employing new additive manufacturing methodologies to rapidly manufacture test samples.

The final chapter of the thesis explored the problematic of ageing assessment of long-lasting products. Substation connectors, as most parts of substations, have lifetimes that exceed the decades. Hence, the assessment of the life expectancy of such products results utterly challenging, due to the difficulty to analyse ageing parameters in a reasonable time that does not compromise product development. Standard ageing tests are based on the performance of cycling tests at a temperature slightly above their rated temperature. These tests are based on as the so-called accelerated degradation tests, tests where the degradation stress cause is augmented in order to fasten the degradation process. Although the standard approach relies in a physical approach to assess the reliability of products, it exists a consensus that the number of cycles suggested by standards, the measures taken, and the applied stresses have a notable lack of scientific basis. Therefore, current standard tests do not provide relevant data about the life expectancy of the tested connectors. For this reason, this chapter proposed the application of the step-stress accelerated degradation test (SSADT) methodology to a set of HTLS substation connectors. This methodology, which has been successfully applied to other products, gives a numeric result of the expected reliability of the tested product after the test. Specifically, the test consisted of the performance of thermal cycles over a sample of ten connectors.

The reliability of the connector, that is, the percentage of working connectors after a determined time, is inferred after calculating a set of parameters that characterize the ageing process. These parameters are the ones that best fit an equation that describes the ageing of the connector. They are obtained by considering some premises about the ageing of connectors. The first is that the connectors' behaviour follows a log-normal distribution. The second is that the electrical resistance evolution has an exponential behaviour. In order to determine the parameters that best characterize the process of deterioration of connectors, an optimization problem has been proposed, which has been solved by means of the stochastic fractal search (SFS) algorithm. The optimization heuristic pursues to maximize the likelihood to find a set of parameters that describe the degradation of the connectors under study. From these parameters, the reliability of the connectors has been calculated, by considering that it is the probability that the connector still performs well after a time-period. The result of this estimation has shown that 98% of the connectors installed, when working at 100ºC, would perform well after 40 years, considering that the maximum allowable final resistance is three times the original one. Several sensitivity analyses have been performed in order to check the validity of the study.

The conclusions of the sensitivity analyses are that the degradation of connectors is basically seen as early-life deterioration. Thus, a special effort during installation of the connectors, including initial measurements of electrical resistance have to be performed in order to minimise early-life deterioration related problems. The sensitivity analyses have been meaningful as well to detect the effect of outliers in the data obtained, as well as the effect of the imposed threshold value of the maximum allowable resistance of the connectors. Conclusions of these sensitivity analyses have shown that the number of samples used for the ageing test performed in this thesis is too short, to avoid problems with outlier samples. However, this limitation is difficult to overcome due to limitations related to the available test-samples and technical requirements of the test facility. It has also been proved that even considering much more restrictive threshold resistance value of 1.5 times the original resistance, the reliability of the substation connectors is still close to 90% after 40 years. Hence, the analysed connector is able to work without observing any remarkable modification of its properties, when used for the application that it has been designed, during the expected time of life considered by the manufacturer. This methodology, as the rest developed through all the thesis, can be and it is aimed to be applied on other high-voltage hardware applications.

6 FURTHER WORK

The elaboration of this thesis has uncover several spots of knowledge still to explore. These are mainly centred on the topics of reduced scale corona tests and ageing tests.

The use of metallic samples produced by means of additive manufacturing, commonly known as 3D printing, is especially appealing when performing reduced-scale corona tests. This is because for determined ambient conditions, corona only depends on the shape of the outer surface of the connector and the applied voltage. The use of 3D printed samples with enough accuracy, would decrease enormously the time required to obtain test samples. This is especially true if these need to be produced by means of sandcasting. Nowadays, the use of such samples is technically feasible, but economically unaffordable. However, it is expected that as in many other applications related to mechatronics, the costs will decrease fast and notably in the following years.

Related to the topic of visual corona, another task that could be carried out in the immediate future is the performance of a much thorough study of the limits of visual corona detection. To do so, it is necessary to explore the use of different lenses or camera accessories. These can be useful to focus the area of interest of connectors more closely and so, to increase the resolution of the photography. At the same time, the values of corona inception obtained by means of a refined visual corona system, can be benchmarked against a system of PD detection all installed this time on a fully screened laboratory.

Another of the topics that has been left out of this thesis is the study of reduced-scale corona tests under DC stresses. A similar approach as the performed in *Chapter 3* of this thesis can be performed using similar connectors. Probably, a more powerful DC source should be used as the inception electric fields for DC excitation are above the values of AC.

Furthermore, among this thesis it has not been completely tackled the subject of the accelerated degradation tests. The ageing test analysed in this thesis only considers the effect of temperature. Other ageing stresses could be added to the study, for instance vibrations or ambient debris infiltration on contacts. Also, a thorough study of the ideal numbers of samples required to perform these tests, the stress steps, and the duration of such steps has to be performed. This, on the end, can drive to the application of test design methodologies to systematically design ageing tests and to apply a systematic approach to help the quality systems of manufacturing companies.

Finally, in the line of the rapid extension of IoT (Internet of Things) in all industrial fields, and especially in the field of high-voltage facilities, there are many possibilities that arise in the field of ageing assessment by using the data obtained from on-line measurements on installed sensed connectors. This data, that will be potentially available for manufacturers and utilities in a frame time of 5 to 10 years, will be able to be analysed adapting the methodologies presented in this thesis related for reliability calculation.

7 REFERENCES

[1] International Energy Agency, “World Energy Outlook 2017.”

[2] “EIA - International Energy Outlook 2017 DOE/EIA-0484(2017),” 2017.

[3] ANSI/NEMA, “ANSI/NEMA CC1. Electric Power Connection for Substation.” Rosslyn, Virginia, 2009.

[4] “Gallery Substations Connectors - Gorny GmbH.” [Online]. Available: http://www.gorny-gmbh.de/gallery-substations-connectors/?lang=en. [Accessed: 10-May-2018].

[5] F. Capelli, J.-R. Riba, and J. Sanllehí, “Finite element analysis to predict temperature rise tests in high-capacity substation connectors,” *IET Gener. Transm. Distrib.*, vol. 11, no. 9, pp. 2283–2291, Jun. 2017.

[6] F. Capelli, J.-R. Riba, and D. Gonzalez, “Optimization of short-circuit tests based on finite element analysis,” in *2015 IEEE International Conference on Industrial Technology (ICIT)*, 2015, pp. 1368–1374.

[7] IEEE Power Engineering Society, “IEEE Standard for Calculating the Current-Temperature Relationship of Bare Overhead Conductors,” *IEEE Std 738-2012 (Revision IEEE Std 738-2006 - Inc. IEEE Std 738-2012 Cor 1-2013)*, pp. 1–72, 2013.

[8] H. Li, A. Bose, and Y. Zhang, “On-line short-circuit current analysis and preventive control to extend equipment life,” *IET Gener. Transm. Distrib.*, vol. 7, no. 1, pp. 69–75, Jan. 2013.

[9] International Electrotechnical Commission, “IEC 62271-1:2007. High-voltage switchgear and controlgear - Part 1: Common specifications.” International Electrotechnical Commission, p. 252, 2007.

[10] E. Kuffel, W. S. Zaengl, and J. Kuffel, *High voltage engineering : fundamentals*. Butterworth-Heinemann/Newnes, 2000.

[11] J. Hernandez-Guiteras, J. Riba, and P. Casals-Torrens, “Determination of the corona inception voltage in an extra high voltage substation connector,” *IEEE Trans. Dielectr. Electr. Insul.*, vol. 20, no. 1, pp. 82–88, Feb. 2013.

[12] Z.-X. Li, J.-B. Fan, Y. Yin, and G. Chen, “Numerical calculation of the negative onset corona voltage of high-voltage direct current bare overhead transmission conductors,” *IET Gener. Transm. Distrib.*, vol. 4, no. 9, p. 1009, 2010.

[13] C. Zhang, Y. Yi, and L. Wang, “Positive dc corona inception on dielectric-coated stranded conductors in air,” *IET Sci. Meas. Technol.*, vol. 10, no. 6, pp. 557–563, Sep. 2016.

[14] J. Hernández-Guiteras, J.-R. R. Riba, L. L. Romeral, J. Hern??ndez-Guiteras, J.-R. R. Riba, and L. L. Romeral, "Improved design of an extra-high-voltage expansion substation connector through magnetic field analysis," *Simul. Model. Pract. Theory*, vol. 43, pp. 96–105, Apr. 2014.

[15] "Ensayos de Alta Tensión con nuevo Generador de Impulso." [Online]. Available: https://www.tecnalia.com/es/actualidad/noticias/ensayos-de-alta-tension-con-nuevo-generador-de-impulso.htm. [Accessed: 10-May-2018].

[16] "ISO 3506-1:2009 - Mechanical properties of corrosion-resistant stainless steel fasteners -- Part 1: Bolts, screws and studs," Geneve, 2009.

[17] ANSI/NEMA, "ANSI/NEMA C119.4 - American National Standard for Electric Connectors— Connectors for Use b etween Aluminum -to-Aluminum and Aluminum -to-Copper Conductors Designed for Normal Operat ion at or Below 93°C and Copper -to-Copper Conductors Designed for Normal Operation at or Below 100°C," 2016.

[18] P. G. Slade, *Electrical contacts : principles and applications*, 2nd Editio. Boca Raton, Florida: CRC Press, 2017.

[19] J. E. Gruzleski, B. M. Closset, and American Foundrymen's Society., *The treatment of liquid aluminum-silicon alloys*. American Foundrymen's Society, 1990.

[20] S.-Z. Lu and A. Hellawell, "The mechanism of silicon modification in aluminum-silicon alloys: Impurity induced twinning," *Metall. Trans. A*, vol. 18, no. 10, pp. 1721–1733, Oct. 1987.

[21] J. F. Hernández Paz, "Heat treatment and precipitation in A356 aluminum alloy," McGill University, Montreal, 2003.

[22] W. D. Callister and W. D. Callister, *Fundamentals of materials science and engineering : an interactive etext*. Wiley, 2001.

[23] F. Capelli, "Development of high-capacity substation connectors compatible with HTLS technology," *TDX (Tesis Dr. en Xarxa)*, Mar. 2019.

[24] F. Capelli, J.-R. Riba, A. Rodriguez, and S. Lalaouna, "Research Towards Energy-Efficient Substation Connectors," Springer, Cham, 2017, pp. 295–301.

[25] J. W. H. Hayt and J. A. Buck, *Engineering Electromagnetics*, 8th Editio. New York, 2011.

[26] International Electrotechnical Commission, "IEC-60694. Common specifications for high-voltage switchgear and controlgear standards." p. 179, 1996.

[27] IEC, "IEC 60059:1999 Standard current ratings," 1999. [Online]. Available: https://webstore.iec.ch/publication/298. [Accessed: 11-Apr-2016].

[28] F. Capelli, J.-R. Riba, and J. Pérez, "Three-Dimensional Finite-Element Analysis of the Short-Time and Peak Withstand Current Tests in Substation Connectors," *Energies*, vol. 9, no. 6, p. 418, May 2016.

[29] P. Huang, C. Mao, and D. Wang, "Analysis of electromagnetic force for medium frequency transformer with interleaved windings," *IET Gener. Transm. Distrib.*, vol. 11, no. 8, pp. 2023–2030, Jun. 2017.

[30] "COMSOL 4.3 Multiphysics User's Guide." 2012.

[31] M. N. Özişik, *Heat Transfer: A Basic Approach*. McGraw-Hill, 1985.

[32] R. L. Shannon, “Thermal Scale Modeling of Radiation-Conduction-Convection Systems,” *J. Spacecr. Rockets*, vol. 10, no. 8, pp. 485–492, Aug. 1973.

[33] S. Kakaç and Y. Yener, *Convective Heat Transfer, Second Edition*. CRC Press, 1994.

[34] G. Buonanno, “Effect of radiative and convective heat transfer on thermal transients in power cables,” *IEE Proc. - Gener. Transm. Distrib.*, vol. 142, no. 4, p. 436, 1995.

[35] J. Hernández-Guiteras, J.-R. Riba, and L. Romeral, “Improved design of an extra-high-voltage expansion substation connector through magnetic field analysis,” *Simul. Model. Pract. Theory*, vol. 43, pp. 96–105, Apr. 2014.

[36] K. Hameyer, J. Driesen, H. De Gersem, and R. Belmans, “The classification of coupled field problems,” *IEEE Trans. Magn.*, vol. 35, no. 3, pp. 1618–1621, May 1999.

[37] Jeong-Hoon Yoon, Heui-Sub Ahn, Jongung Choi, and Il-Sung Oh, “An Estimation Technology of Temperature Rise in GIS Bus Bar using Three-Dimensional Coupled-Field Multiphysics,” in *Conference Record of the 2008 IEEE International Symposium on Electrical Insulation*, 2008, pp. 432–436.

[38] X. Li, J. Qu, Q. Wang, H. Zhao, and D. Chen, “Numerical and Experimental Study of the Short-Time Withstand Current Capability for Air Circuit Breaker,” *IEEE Trans. Power Deliv.*, vol. 28, no. 4, pp. 2610–2615, Oct. 2013.

[39] Jianyu Qu, Qian Wang, Junmin Zhang, Hu Zhao, Gang Wu, and Xingwen Li, “3-D Transient Finite-Element Analysis and Experimental Investigation of Short-Circuit Dynamic Stability for Air Circuit Breaker,” *IEEE Trans. Components, Packag. Manuf. Technol.*, vol. 5, no. 11, pp. 1610–1617, Nov. 2015.

[40] X. Guan, N. Shu, B. Kang, and M. Zou, “Multiphysics Analysis of Plug-In Connector Under Steady and Short Circuit Conditions,” *IEEE Trans. Components, Packag. Manuf. Technol.*, vol. 5, no. 3, pp. 320–327, 2015.

[41] A. Mauri, R. Sacco, and M. Verri, “Electro-thermo-chemical computational models for 3D heterogeneous semiconductor device simulation,” *Appl. Math. Model.*, vol. 39, no. 14, pp. 4057–4074, Jul. 2015.

[42] R. Naar and F. Bay, “Numerical optimisation for induction heat treatment processes,” *Appl. Math. Model.*, vol. 37, no. 4, pp. 2074–2085, Feb. 2013.

[43] C. Geuzaine and N. Marsic, “Efficient finite element assembly of high order Whitney forms,” *IET Sci. Meas. Technol.*, vol. 9, no. 2, pp. 204–210, Mar. 2015.

[44] Y. Sato and H. Igarashi, “Model Reduction of Three-Dimensional Eddy Current Problems Based on the Method of Snapshots,” *IEEE Trans. Magn.*, vol. 49, no. 5, pp. 1697–1700, May 2013.

[45] K. Rezk and J. Forsberg, “A fast running numerical model based on the implementation of volume forces for prediction of pressure drop in a fin tube heat exchanger,” *Appl. Math. Model.*, vol. 38, no. 24, pp. 5822–5835, Dec. 2014.

[46] X. Wang and Y. Jiang, “Model reduction of discrete-time bilinear systems by a Laguerre expansion technique,” *Appl. Math. Model.*, Feb. 2016.

[47] A. A. P. da Silva and J. M. de Barros Bezerra, “A Model for Uprating Transmission Lines by Using HTLS Conductors,” *Power Delivery, IEEE Transactions on*, vol. 26, no. 4. pp. 2180–2188, 2011.

[48] H. Cotal and J. Frost, “Heat transfer modeling of concentrator multijunction solar cell assemblies using finite difference techniques,” in *2010 35th IEEE Photovoltaic Specialists Conference*, 2010, pp. 000213–000218.

[49] G. R. Kefayati, “Simulation of heat transfer and entropy generation of MHD natural convection of non-Newtonian nanofluid in an enclosure,” *Int. J. Heat Mass Transf.*, vol. 92, pp. 1066–1089, Jan. 2016.

[50] G. R. Kefayati, “FDLBM simulation of entropy generation due to natural convection in an enclosure filled with non-Newtonian nanofluid,” *Powder Technol.*, vol. 273, pp. 176–190, Mar. 2015.

[51] J. Sui, N. Sugita, and M. Mitsuishi, “Thermal Modeling of Temperature Rise for Bone Drilling With Experimental Validation,” *J. Manuf. Sci. Eng.*, vol. 137, no. 6, p. 061008, Sep. 2015.

[52] C. Islam, I. Lazoglu, and Y. Altintas, “A Three-Dimensional Transient Thermal Model for Machining,” *J. Manuf. Sci. Eng.*, vol. 138, no. 2, p. 021003, Sep. 2015.

[53] S.-C. Chung and B.-K. Min, “Thermal Analysis of Ballscrew Systems by Explicit Finite Difference Method,” *Trans. KSME, A*, vol. 41, no. 1, pp. 41–51, 2016.

[54] S. A. Mohamed, R. A. Shanab, and L. F. Seddek, “Vibration analysis of Euler–Bernoulli nanobeams embedded in an elastic medium by a sixth-order compact finite difference method,” *Appl. Math. Model.*, vol. 40, no. 3, pp. 2396–2406, Feb. 2016.

[55] B. N. Datta, *Numerical Linear Algebra and Applications, Second Edition*, Second edi. Philadelphia, PA: SIAM, 2010.

[56] C. Abomailek, F. Capelli, J.-R. Riba, and P. Casals-Torrens, “Transient thermal modelling of substation connectors by means of dimensionality reduction,” *Appl. Therm. Eng.*, vol. 111, pp. 562–572, 2017.

[57] A. D. Polykrati, C. G. Karagiannopoulos, and P. D. Bourkas, “Thermal effect on electric power network components under short-circuit currents,” *Electr. Power Syst. Res.*, vol. 72, no. 3, pp. 261–267, 2004.

[58] J. L. J.Oliver, M. Cervera, S. Oller, “Isotropic damage models and smeared crack analysis of concrete,” *Proc. SCI-C Comput. Aided Anal. Des. Concr. Struct.*, vol. 945958, 1990.

[59] S. W. Churchill and H. H. S. Chu, “Correlating equations for laminar and turbulent free convection from a horizontal cylinder,” *Int. J. Heat Mass Transf.*, vol. 18, no. 9, pp. 1049–1053, Sep. 1975.

[60] S. Boetcher, *Natural Convection from Circular Cylinders*. Springer, 2014.

[61] Z. H. Qureshi and R. Ahmad, “Natural convection from a uniform heat flux horizontal cylinder at moderate rayleigh numbers,” *Numer. Heat Transf.*, vol. 11, no. 2, pp. 199–212, Feb. 1987.

[62] L. P. Yarin, *The Pi-Theorem*. Berlin, Heidelberg: Springer Berlin Heidelberg, 2012.

[63] E. Buckingham, “On Physically Similar Systems; Illustrations of the Use of Dimensional Equations,” *Phys. Rev.*, vol. 4, no. 4, pp. 345–376, Oct. 1914.

[64] A. L. Garner and K. Lewis, “Buckingham Pi Analysis of Railgun Multiphysics,” *IEEE Trans. Plasma Sci.*, vol. 42, no. 8, pp. 2104–2112, Aug. 2014.

[65] C. P. Coutinho, A. J. Baptista, and J. Dias Rodrigues, “Reduced scale models based on similitude theory: A review up to 2015,” *Eng. Struct.*, vol. 119, pp. 81–94, 2016.

[66] Shannon and R. L., “Thermal scale modeling of radiation-conduction-convection systems.,” Apr. 1972.

[67] T. Szirtes and P. Rózsa, *Applied dimensional analysis and modeling*. Elsevier/Butterworth-Heinemann, 2007.

[68] C. Abomailek, J.-R. Riba, F. Capelli, and M. Moreno-Eguilaz, “Fast electro-thermal simulation of short-circuit tests,” *IET Gener. Transm. Distrib.*, vol. 11, no. 8, 2017.

[69] A. D. Polykrati, C. G. Karagiannopoulos, and P. D. Bourkas, “Thermal effect on electric power network components under short-circuit currents,” *Electr. Power Syst. Res.*, vol. 72, no. 3, pp. 261–267, Dec. 2004.

[70] International Electrotechnical Commission, “IEC 62271-1:2007. High-voltage switchgear and controlgear - Part 1: Common specifications.” International Electrotechnical Commission, p. 252, 2007.

[71] IEEE, “IEEE Std 100-2000 The Authoritative Dictionary of IEEE Standards Terms, Seventh Edition,” *IEEE Std 100-2000*. pp. 1–1362, 2000.

[72] Z. Du, D. Huang, Z. Qiu, S. Shu, and J. Ruan, “Prediction study on positive DC corona onset voltage of rod-plane air gaps and its application to the design of valve hall fittings,” *IET Gener. Transm. Distrib.*, vol. 10, no. 7, pp. 1519–1526, May 2016.

[73] W. W. Strong, “The Positive and the Negative Corona and Electrical Precipitation,” *Trans. Am. Inst. Electr. Eng.*, vol. XXXII, no. 2, pp. 1755–1765, May 1913.

[74] M. M. Abouelsaad, “Modelling of corona discharge of a tri-electrode system for electrostatic separation processes,” *IET Sci. Meas. Technol.*, vol. 8, no. 6, pp. 497–504, Nov. 2014.

[75] X. Zhang, K. Huang, and X. Xiao, “Modelling of the corona characteristics under damped oscillation impulses,” *IET Gener. Transm. Distrib.*, vol. 10, no. 7, pp. 1648–1653, May 2016.

[76] E. Kuffel, W. S. Zaengl, and J. Kuffel, *High voltage engineering : fundamentals*. Butterworth-Heinemann/Newnes, 2000.

[77] K. Adamiak and P. Atten, “Simulation of corona discharge in point-plane configuration,” 2003, pp. 104–118.

[78] Comsol, “COMSOL 4.3 Multiphysics User’s Guide.” COMSOL, p. 1292, 2012.

[79] F. W. (Frank W. Peek, *Dielectric phenomena in high voltage engineering*. [Lightning Source UK?], 2007.

[80] L. B. Loeb and S. C. Brown, “Electrical Coronas: Their Basic Physical Mechanisms,” *Phys. Today*, vol. 19, no. 1, pp. 109–111, Jan. 1966.

[81] X. Cui *et al.*, “Accurate measurement of original current pulses because of positive corona in the coaxial cylindrical arrangement,” *IET Sci. Meas. Technol.*, vol. 9, no. 1, pp. 12–19, Jan. 2015.

[82] E. A. Yahaya, M. Tsado Jacob, and A. A. Nwohu, "Power loss due to Corona on High Voltage Transmission Lines," *IOSR J. Electr. Electron. Eng.*, vol. 8, no. 3, pp. 14–19, 2013.

[83] The Central Station Engineers of The Westinghouse Eectric and Corporation, *Electrical Transmission and Distribution Reference Book*, Fourth edi. East Pittsburgh, Pennsylvania: Westinghouse, 1964.

[84] Electric Power Research Institute, *Transmission line reference book 345 kV and above*, 2014 Editi. Palo Alto, CA: Electric Power Research Institute (EPRI), 2014.

[85] M. S. Naidu and V. Kamaraju, *High Voltage Engineering*. New York: Tata McGraw-Hill Publishing Company Limited, 1996.

[86] Cigré Working Group 36.01, "ADDENDUM to CIGRE Document N° 20 (1974) : INTERFERENCES PRODUCED BY CORONA EFFECT OF ELECTRIC SYSTEMS," 1974.

[87] A. Carsimamovic, A. Mujezinovic, S. Carsimamovic, Z. Bajramovic, M. Kosarac, and K. Stankovic, "Calculation of the corona onset voltage gradient under variable atmospheric correction factors," in *IEEE EUROCON 2015 - International Conference on Computer as a Tool (EUROCON)*, 2015, pp. 1–5.

[88] A. Fridman, A. Fridman, and L. A. Kennedy, *Plasma Physics and Engineering*, Second Edi. CRC Press, 2011.

[89] F. W. Peek, "The Law of Corona and the Dielectric Strength of Air-II," *Proc. Am. Inst. Electr. Eng.*, vol. XXXI, no. 7, pp. 1051–1092, Jul. 1911.

[90] A. L. Souza and I. J. S. Lopes, "Experimental investigation of corona onset in contaminated polymer surfaces," *IEEE Trans. Dielectr. Electr. Insul.*, vol. 22, no. 2, pp. 1321–1331, Apr. 2015.

[91] NEMA, "NEMA 107-2016. Methods of Measurement of Radio Influence Voltage (RIV) of High Voltage Apparatus - NEMA." pp. 1–19, 2016.

[92] International Electrotechnical Commission, *IEC 60270:2000 High-voltage test techniques - Partial discharge measurements*, 3.0. International Electrotechnical Commission, 2000.

[93] IEEE, "1829-2017 - IEEE Guide for Conducting Corona Tests on Hardware for Overhead Transmission Lines and Substations," 2017.

[94] IEEE, "IEEE Std 4-2013 (Revision of IEEE Std 4-1995) IEEE Standard for High-Voltage Testing Techniques," *IEEE Std 4-2013 (Revision of IEEE Std 4-1995)*. pp. 1–213, 2013.

[95] IEEE, "IEEE Std 1829-2017 - IEEE Guide for Conducting Corona Tests on Hardware for Overhead Transmission Lines and Substations," 2017.

[96] G. H. Vaillancourt, R. Malewski, and D. Train, "Comparison of Three Techniques of Partial Discharge Measurements in Power Transformers," *IEEE Trans. Power Appar. Syst.*, vol. PAS-104, no. 4, pp. 900–909, Jul. 1985.

[97] G. H. Vaillancourt, A. Dechamplain, and R. A. Malewski, "Simultaneous measurement of partial discharge and radio-interference voltage," *IEEE Trans. Instrum. Meas.*, vol. IM-31, no. 1, pp. 49–52, Mar. 1982.

[98] N. L. Allen, M. Abdel-Salam, and I. Cotton, “Effects of temperature and pressure change on positive corona and sparkover under direct voltage in short airgaps,” *IET Sci. Meas. Technol.*, vol. 1, no. 4, pp. 210–215, Jul. 2007.

[99] IEC, “IEC 60437:1997. Radio interference test on high-voltage insulators.” International Electrotechnical Commission, Geneva, Switzerland, pp. 1–29, 1997.

[100] Q. Yang, Y. Chen, W. Sima, and H. Zhao, “Measurement and analysis of transient overvoltage distribution in transformer windings based on reduced-scale model,” *Electr. Power Syst. Res.*, vol. 140, pp. 70–77, 2016.

[101] H. Li, N. Shu, X. Wu, H. Peng, and Z. Li, “Scale Modeling on the Overheat Failure of Bus Contacts in Gas-Insulated Switchgears,” *IEEE Trans. Magn.*, vol. 50, no. 2, pp. 305–308, Feb. 2014.

[102] R. G. Urban, H. C. Reader, and J. P. Holtzhausen, “Small Corona Cage for Wideband HVac Radio Noise Studies: Rationale and Critical Design,” *IEEE Trans. Power Deliv.*, vol. 23, no. 2, pp. 1150–1157, Apr. 2008.

[103] Joseph Chambers, *Modeling Flight : The role of dynamically scale*. NASA, 2015.

[104] J. Hernandez-Guiteras, J. R. Riba, P. Casals-Torrens, and R. Bosch, “Feasibility analysis of reduced-scale air breakdown tests in high voltage laboratories combined with the use of scaled test cages,” *IEEE Trans. Dielectr. Electr. Insul.*, vol. 20, pp. 1590–1597, 2013.

[105] X. Bian *et al.*, “Corona-generated space charge effects on electric field distribution for an indoor corona cage and a monopolar test line,” *IEEE Trans. Dielectr. Electr. Insul.*, vol. 18, no. 5, pp. 1767–1778, Oct. 2011.

[106] Y. Nakano and Y. Sunaga, “Availability of corona cage for predicting audible noise generated from HVDC transmission line,” *IEEE Trans. Power Deliv.*, vol. 4, no. 2, pp. 1422–1431, Apr. 1989.

[107] J. Hernandez-Guiteras, J.-R. Riba, P. Casals-Torrens, and R. Bosch, “Feasibility analysis of reduced-scale air breakdown tests in high voltage laboratories combined with the use of scaled test cages,” *IEEE Trans. Dielectr. Electr. Insul.*, vol. 20, no. 5, pp. 1590–1597, Oct. 2013.

[108] L. Xie, L. Zhao, J. Lu, X. Cui, and Y. Ju, “Altitude Correction of Radio Interference of HVDC Transmission Lines Part I: Converting Method of Measured Data,” *IEEE Trans. Electromagn. Compat.*, vol. 59, no. 1, pp. 275–283, Feb. 2017.

[109] L. Zhao, X. Cui, L. Xie, J. Lu, K. He, and Y. Ju, “Altitude Correction of Radio Interference of HVdc Transmission Lines Part II: Measured Data Analysis and Altitude Correction,” *IEEE Trans. Electromagn. Compat.*, vol. 59, no. 1, pp. 284–292, Feb. 2017.

[110] F. Yin, M. Farzaneh, and X. Jiang, “Corona investigation of an energized conductor under various weather conditions,” *IEEE Trans. Dielectr. Electr. Insul.*, vol. 24, no. 1, pp. 462–470, Feb. 2017.

[111] S. Rabe and B. Schartel, “The rapid mass calorimeter: Understanding reduced-scale fire test results,” *Polym. Test.*, vol. 57, pp. 165–174, 2017.

[112] D. S. Prasad and B. S. Reddy, “Digital image processing techniques for estimating power released from the corona discharges,” *IEEE Trans. Dielectr. Electr. Insul.*, vol. 24, no. 1, pp. 75–82, Feb. 2017.

[113] D. S. Prasad and B. S. Reddy, "Study of corona degradation of polymeric insulating samples using high dynamic range imaging technique," *IEEE Trans. Dielectr. Electr. Insul.*, vol. 24, no. 2, pp. 1169–1177, Apr. 2017.

[114] Q. Hu, L. Shu, X. Jiang, C. Sun, S. Zhang, and Y. Shang, "Effects of air pressure and humidity on the corona onset voltage of bundle conductors," *IET Gener. Transm. Distrib.*, vol. 5, no. 6, p. 621, Jun. 2011.

[115] M. Braunovic, V. V. Izmailov, and M. V. Novoselova, "A model for life time evaluation of closed electrical contacts," in *Proceedings of the Fifty-First IEEE Holm Conference on Electrical Contacts, 2005.*, 2005, pp. 217–223.

[116] M. Sun, M. G. Pecht, M. A. E. Natishan, and R. I. Martens, "Lifetime resistance model of bare metal electrical contacts," *IEEE Trans. Adv. Packag.*, vol. 22, no. 1, pp. 60–67, 1999.

[117] J.-R. Riba Ruiz, A.-G. Mancini, C. Abomailek, and F. Capelli, "A 3D-FEM-based model to predict the electrical constriction resistance of compressed contacts," *Measurement*, vol. 114, pp. 44–50, 2018.

[118] *Electrical Contacts: Principles and Applications, Second Edition*. CRC Press, 2013.

[119] R. D. Malucci, "Stability and contact resistance failure criteria," *IEEE Trans. Components Packag. Technol.*, vol. 29, no. 2, pp. 326–332, Jun. 2006.

[120] N. . Myshkin, M. . Petrokovets, and S. . Chizhik, "Basic problems in contact characterization at nanolevel," *Tribol. Int.*, vol. 32, no. 7, pp. 379–385, Jul. 1999.

[121] C. Hildmann, S. Grossmann, and T. Dockhorn, "ICEC 2014; The 27th International Conference on Electrical Contacts; Proceedings of," *ICEC 2014; The 27th International Conference on Electrical Contacts; Proceedings of*. pp. 1–6, 2014.

[122] R. D. Malucci and F. R. Ruffino, "A Method for Power Rating Contacts using Voltage Drop," in *2008 Proceedings of the 54th IEEE Holm Conference on Electrical Contacts*, 2008, pp. 225–231.

[123] J. Lienig and Jens, "Electromigration and its impact on physical design in future technologies," in *Proceedings of the 2013 ACM international symposium on International symposium on physical design - ISPD '13*, 2013, p. 33.

[124] J. Aronstein, "AC and DC electromigration in aluminum," in *Electrical Contacts - 1996. Proceedings of the Forty-Second IEEE Holm Conference on Electrical Contacts. Joint with the 18th International Conference on Electrical Contacts*, 1996, pp. 311–320.

[125] R. Timsit, "On the Evalutation of Contact Temperature from Potential-Drop Measurements," *IEEE Trans. Components, Hybrids, Manuf. Technol.*, vol. 6, no. 1, pp. 115–121, Mar. 1983.

[126] M. Gatzsche, N. Lucke, S. Grobmann, T. Kufner, B. Hagen, and G. Freudiger, "Electric-thermal performance of contact elements in high power plug-in connections," in *2014 IEEE 60th Holm Conference on Electrical Contacts (Holm)*, 2014, pp. 1–8.

[127] R. F. Frank and C. P. Morton, "Comparative Corrosion and Current Burst Testing of Copper and Aluminum Electrical Power Connectors," *IEEE Trans. Ind. Appl.*, vol. 43, no. 2, pp. 462–468, 2007.

[128] R. Bergmann, H. Lobl, H. Bohme, and S. Grossmann, "Model to assess the reliability of electrical joints," in *Electrical Contacts - 1996. Proceedings of the Forty-Second IEEE Holm Conference on Electrical Contacts. Joint with the 18th International Conference on Electrical Contacts*, 1996, pp. 180–188.

[129] W. Nelson, *Accelerated testing : statistical models, test plans and data analyses*. Wiley-Interscience, 2004.

[130] W. Q. Meeker, L. A. Escobar, and C. J. Lu, "Accelerated Degradation Tests: Modeling and Analysis," *Technometrics*, vol. 40, no. 2, p. 89, May 1998.

[131] W. Nelson, *Accelerated testing : statistical models, test plans and data analyses*. Wiley, 1990.

[132] F. De Carlo, O. Borgia, and M. Tucci, "Accelerated degradation tests for reliability estimation of a new product: A case study for washing machines," *Proc. Inst. Mech. Eng. Part O J. Risk Reliab.*, vol. 228, no. 2, pp. 127–138, Apr. 2014.

[133] Hongyu Tang, D. G. Yang, G. Q. Zhang, Fengze Hou, Miao Cai, and Zaifu Cui, "Multi-physics simulation and reliability analysis for LED luminaires under step stress accelerated degradation test," in *2012 13th International Thermal, Mechanical and Multi-Physics Simulation and Experiments in Microelectronics and Microsystems*, 2012, p. 1/5-5/5.

[134] Sun Fuqiang, Li Xiaoyang, and Jiang Tongmin, "Reliability Evaluation for Microwave Electronical Assembly Based on Step-stress ADT with Multiple Degradation Measures," *Int. J. Adv. Comput. Technol.*, vol. 5, no. 6, pp. 578–586, Mar. 2013.

[135] S. Mohajeryami, M. Nagisetty, M. Doostan, and Z. Salami, "Investigation of naturally aged timing relays' service life by employing thermally accelerated aging," in *2016 IEEE/PES Transmission and Distribution Conference and Exposition (T&D)*, 2016, pp. 1–5.

[136] A. L. Petrou, M. Roulia, and K. Tampouris, "The use of the Arrhenius equationin the study of deterioration and of cooking foods - some scientific and pedagogic aspects," *Chem. Educ. Res. Pr.*, vol. 3, no. 1, pp. 87–97, 2002.

[137] W. Chen, J. Liu, L. Gao, J. Pan, and X. Lu, "Step-stress accelerated degradation test modeling and statistical analysis methods," *Chinese J. Mech. Eng.*, vol. 26, no. 6, pp. 1154–1159, Nov. 2013.

[138] L. Qingya, G. Jinchun, X. Gang, J. Qiuyan, and J. Rui, "Lifetime prediction of electrical connectors under multiple environment stresses of temperature and particulate contamination," *J. China Univ. Posts Telecommun.*, vol. 23, no. 5, pp. 61–81, Oct. 2016.

[139] H. Salimi, "Stochastic Fractal Search: A powerful metaheuristic algorithm," *Knowledge-Based Syst.*, vol. 75, pp. 1–18, Feb. 2015.

[140] C. Blum and A. Roli, "Metaheuristics in combinatorial optimization: Overview and conceptual comparison," vol. 35, no. 3, pp. 268–308, 2003.

[141] M. (Computer scientist) Mitchell, *An introduction to genetic algorithms*. MIT Press, 1996.

[142] J. Kennedy and R. Eberhart, "Particle swarm optimization," in *Proceedings of ICNN'95 - International Conference on Neural Networks*, vol. 4, pp. 1942–1948.

[143] D. Karaboga, “An Idea Based on Honey Bee Swarm For Numerical Optimization,” 2005.

[144] A. Saltelli *et al.*, *Global Sensitivity Analysis: The Primer*. John Wiley & Sons, 2008.

[145] D. Pannell, “Sensitivity analysis of normative economic models: theoretical framework and practical strategies,” *Agric. Econ.*, vol. 16, no. 2, pp. 139–152, May 1997.

8 APPENDICES

APPENDIX 1: PHYSICAL PROPERTIES OF THE HTLS CONDUCTORS AND CONNECTORS

Variable	Value	Value
Conductor type	GTACSR-464	GTACSR-131
Aluminum conductor mass	559.8 kg/km	320.8 kg/km
Steel conductor mass	367 kg/km	210,32 kg/km
Diameter of the conductor	27.60 mm	15.79 mm
Diameter of steel core	9.00 mm	5.55 mm
Aluminum thermal heat capacity, Cp_{Al}	534.6 J/(m·K)	534.6 J/(m·K)
Steel thermal heat capacity, Cp_{steel}	174.7 J/(m·K)	174.7 J/(m·K)
Conductor electrical resistivity, $\rho_{e,20^oC}$	$4.46 \cdot 10^{-8}$ Ω·m	$4.46 \cdot 10^{-8}$ Ω·m
Temperature coefficient, α_{cd}	0.0041 1/K	0.0041 1/K
Aluminum thermal conductivity, kp_{Al}	229 W/(m·K)	229 W/(m·K)
Steel thermal conductivity, kp_{steel}	43 W/(m·K)	43 W/(m·K)

Variable	Value
Aluminum alloy	A356.0
Aluminum mass density	2700 kg/m^3
Aluminum thermal heat capacity, Cp_{Al}	534.6 J/(m·K)
Aluminum thermal conductivity, kp_{Al}	229 W/(m·K)
Connector thermal emissivity, ε	0.45
Connector electrical resistivity, ρ_e	$4.5 \cdot 10^{-8}$ Ω·m
Temperature coefficient, α_{cd}	0.004 1/K
Contact resistance factor*	2

*Based on measurements, it is known that the contact resistance is 2 times higher than the theoretical connector resistance

APPENDIX 2: CONNECTOR DRAWS

REF Nº: S285TLS_esc	REV	DATE	DESCRIPTION	BY	CHK
	0	26/04/2016	DRAWING RELEASED	IES	FCA

Un = kV
In = A
Icc = kA/s

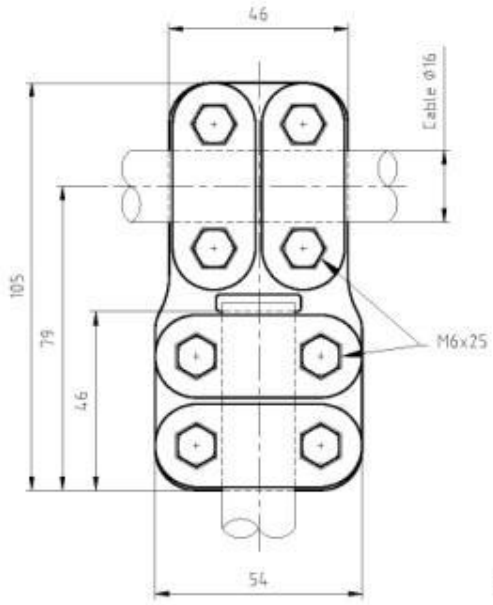

NOTES:

1. MATERIAL: EN 1706 AC-42100 (Al. ALLOY 356 ASTM B26)
2. HARDWARE MATERIAL: A2 STAINLESS STEEL.
3. SURFACE FINISH: AS CAST.
4. FOR USING HARDWARE WITH A4 STAINLESS STEEL: ADD "4" TO END OF REF. Nº.: (...4)
5. CATALOGUE NUMBER RAISED MARKING H:4+5mm.
6. DRAWING UNITS: LENGTH: (mm); FORCE: (N); TORQUE: (Nm); TIME: (s); TEMPERATURE: (ºC)
7. CLEAN CONDUCTOR & CONTACT SURFACES. THEN SCRATCH-BRUSH CONDUCTOR & CONTACT SURFACES UNDER "CONTACT GREASE".

HARDWARE TYPE	RECOMMENDED TORQUE MOMENT [Nm]				
	M8	M10	M12	M14	M16
STAINLESS STEEL	15	35	60	90	140

CUST. PROJ. Nº:			REV:
DATE:	ITEM Nº:	POS. Nº:	A =
COMMENTS:			B =
			C =
			D =

FIRST ANGLE PROJECTION	AL T-CONNECTOR			
	REF Nº: S285TLS_esc			
	SCALE: NTS	SIZE: A4	KG: –	
	DRAWN BY: IES		26/04/2016	
-TOLERANCES-	CHECKER: FCA		26/04/2016	
DIMENSION TYPE ISO 8062	PROD FAM: ST		DOC. TYPE: Sales	
ANGLES ±2º	DRAWING Nº: BSA535185		REV: 0	

SBI Connectors
SAAE-GX PRODUCTS
www.sbiconnect.es
substation@sbiconnect.es

REF Nº: S285A4P23LS_esc	REV	DATE	DESCRIPTION	BY	CHK
	0	26/04/2016	DRAWING RELEASED	IES	FCA

Un = kV
In = A
Icc = kA/s

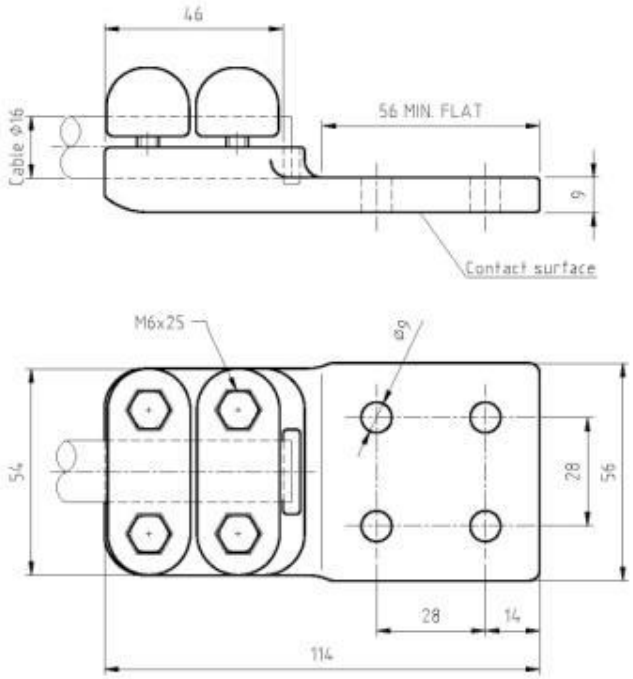

NOTES:

1. MATERIAL: EN 1706 AC-42100 (Al. ALLOY 356 ASTM B26)
2. HARDWARE MATERIAL: A2 STAINLESS STEEL.
3. SURFACE FINISH: AS CAST.
4. TO ORDER CUPAL SHEET ADD "C" TO END OF REF. Nº: (...C)
5. FOR USING HARDWARE WITH A4 STAINLESS STEEL: ADD "4" TO END OF REF. Nº.: (...4)
6. CATALOGUE NUMBER RAISED MARKING H:4+5mm.
7. DRAWING UNITS: LENGTH: (mm); FORCE: (N); TORQUE: (Nm); TIME: (s); TEMPERATURE: (°C)
8. CLEAN CONDUCTOR & CONTACT SURFACES. THEN SCRATCH-BRUSH CONDUCTOR & CONTACT SURFACES UNDER "CONTACT GREASE".

HARDWARE TYPE	RECOMMENDED TORQUE MOMENT [Nm]				
	M8	M10	M12	M14	M16
STAINLESS STEEL	15	35	60	90	140

CUST. PROJ. Nº:		REV:
DATE:	ITEM Nº: POS. Nº:	A =
COMMENTS:		B =
		C =
		D =

FIRST ANGLE PROJECTION	AL TERMINAL	
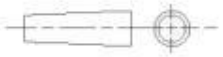	REF Nº: S285A4P23LS_esc	SBI Connectors SAAE-DX PRODUCTS www.sbiconnect.es substation@sbiconnect.es
-TOLERANCES-	SCALE: NTS SIZE: A4 KG: –	
DIMENSION TYPE: ISO 8062	DRAWN BY: IES 26/04/2016	
ANGLES ±2º	CHECKER: FCA 26/04/2016	
	PROD FAM: SA DOC. TYPE: Sales	
	DRAWING Nº: BSA535186 REV: 0	